Summer 2018

Optimization of Top Contact for Cu(In,Ga)Se2 Solar Cells

Grace Cherukara Rajan
Old Dominion University

OPTIMIZATION OF TOP CONTACT FOR $Cu(In,Ga)Se_2$ SOLAR CELLS

by

Grace Cherukara Rajan
B.Tech. May 2009, Kerala University, India

A Dissertation Submitted to the Faculty of
Old Dominion University in Partial Fulfillment of the
Requirements for the Degree of

DOCTOR OF PHILOSOPHY

ELECTRICAL AND COMPUTER ENGINEERING

OLD DOMINION UNIVERSITY
August 2018

Approved by:

_____
Sylvain Marsillac (Director)

_____
Gon Namkoong (Member)

_____
Christopher Bailey (Member)

_____
Xiaoyu Zhang (Member)

ABSTRACT

OPTIMIZATION OF TOP CONTACT FOR Cu(In,Ga)Se_2 SOLAR CELLS

Grace Cherukara Rajan
Old Dominion University, 2018
Director: Dr. Sylvain Marsillac

As world energy demands continue to increase, the need to generate electricity from a broader variety of sources, including renewables, is more critical than ever. With costs still 30% higher than those of natural gas, solar energy is a viable contender, but more progress is needed to level the playing field with other forms of energy generation. The overall energy security can be enhanced by diversifying the energy supply. Among them, Cu(In,Ga)Se_2 (CIGS) has gained significant momentum as a possible high efficiency and low cost thin film solar cell material. The capacity to scale up any photovoltaic technology is one of the criteria that will determine its long term viability. In the case of CIGS, many manufacturers are showing the way for GW-scale production capacity. However, as CIGS technology continues to increase its share of the market, the scarcity and high price of indium will potentially affect its ability to compete with other technologies. One way to avoid this bottleneck is to reduce the importance of indium in the fabrication of the cell simply by reducing its thickness without significant efficiency loss. Reducing the thickness of CIGS thin film will not only save the material but will also lower the production time and the power needed to produce the cell. As the properties of the absorber and buffer layers are modified with each enhancement, it is also important to continue developing a better and effective light trapping mechanism. The overall reflection losses can be minimized to a great extent by applying an efficient anti-reflective (AR) coating, thus

increasing the power conversion efficiency of the device. We describe a method using in-situ real time spectroscopic ellipsometry and optical modeling allowing for the optimization of the thickness of the anti-reflective (AR) coating for $Cu(In_{1-x}Ga_x)Se_2$ (CIGS) solar cells. The model is based on a transfer matrix theory as well as accurate measurement of the dielectric function and thickness of each layer in the stack by spectroscopic ellipsometry. The AR coating thickness is then optimized in real time to optically enhance the performance of the device for various device configurations by varying the thickness and properties of different layers.

In ultra-thin CIGS solar cells, multi-layered anti-reflective coatings are essential since a single layer AR coating is not capable of suppressing the reflectance as it increases. Thus it is very important to obtain an enhanced light trap in the red and near infra-red region. Multi-layer AR coatings are used to obtain at least five passes in the internal reflection from the bottom surface of the cell.

This dissertation is dedicated to my family, T. J. Rajan, Money Rajan and John C. Rajan.

ACKNOWLEDGMENTS

I would like to express my sincere gratitude Dr. Sylvain Marsillac, my advisor, for his never ending support and invaluable guidance throughout my academic career. His guidance and support has always inspired me to have a positive outlook towards life and always strive to excellence. Without his resolute belief in my abilities and dedicated involvement, my life at Old Dominion University would not have been so successful.

I would also like to thank to Dr. Christopher Bailey for his invaluable advice and guidance in my research. I am grateful to my committee members Dr. Gon Namkoong and Dr. Xiaoyu Zhang for their time, invaluable suggestions, and comments.

I am fortunate to be a part of the Virginia Institute of Photovoltaics (VIPV) at Old Dominion University, whose members have all helped me in making this dissertation a success. In particular, I would like to acknowledge the support and encouragement I received from Shankar Karki, Dr. Krishna Aryal, Dr.Yunus Erkaya, Dr.Tasnuva Ashrafee, Hareen Illa, Nitin Hedge, Dr. Patrick Boland, Dr. Vikash Ranjan and Dr. Thomas Begou, who helped me stay motivated during my Ph.D.

I would like to thank the staff at Old Dominion University, Romina Samson, Linda Marshall, Deborah Kinney, and Lori Barrett.

I am also grateful to the invaluable love, kindness, and support I received from my friends during this time, which was a great source of strength for me throughout my PhD studies. For all the food, fun, love and laughter, I owe it all to you. Thank you for always believing in me. The Basnet family, Swetha, Ujwal, Shreya, Griffin, Naveen, Arun and Sachin, thank you for always being there! New Life Church - all my prayer warriors, thank

you for always supporting me through all these years and helping me to re-focus on the true values of life.

Finally, I would like to acknowledge, with gratitude, my family for their unconditional love, unceasing prayers, unwavering enthusiasm, and steadfast encouragement during this time, without which this dissertation would not have been possible. Thank you for always encouraging me to attain greater heights – for always reminding me “with God by my side, it is all possible”.

TABLE OF CONTENTS

LIST OF TABLES

LIST OF FIGURES

CHAPTER 1

INTRODUCTION

1.1. Motivation and Background

The global energy demand is anticipated to increase exponentially every year due to the growth in world population and economic and technological advancement. The majority of the world's current energy sources account to non-renewable fossil fuels such as coal, oil, and natural gas. According to recent publications of World Energy Assessment [1],[2], the power demand is expected to increase to around 30 TW, by the year 2050. The existing fossil fuel reserves are very well sufficient to meet this energy requirement, however the excessive usage of fossil fuels leads to the emission of greenhouse gases and contributes to severe climatic changes. The annual global CO_2 emission from fuel combustion have dramatically increased from near zero to over 32 $GtCO_2$ in 2014 since the industrial revolution [3]. By 2050, these rocketing values of CO_2 emissions will make the earth a less habitable place to live on. Strategies must be developed to reduce the CO_2 emissions to slow down and eventually reverse global warming. A feasible approach to this problem is to switch the heavy dependence on fossil fuels towards renewable, emission free sources of energy such as nuclear fission, hydropower, biomass, wind, geothermal, and solar energy. It took the oil crisis in the 1970's to gain the world's attention to the importance of using alternate energy sources [4]. Photovoltaics (PV) is the direct conversion of sunlight into electricity and it is one of the most promising and cleanest energy source having the potential to meet the global energy demand. 173,000 TW of solar energy strikes the earth continuously which is 10,000 times the annual energy demand, making it the most abundant energy resource on the earth [5].

1.2. Solar Cell Technologies

The solar cell technologies have been categorized into different generations based on their history of development. Bulk crystalline or multi-crystalline silicon has the longest history and they are referred to as the first generation PV technology. This generation occupies almost about 90% of the solar module market share and exhibits about 26.7% of the submodule efficiency and 24.4% module efficiency[6]. However, the production of monocrystalline solar cells is expensive due to the cost of solar grade silicon feedstock. It is challenging to economically fabricate crystalline silicon cells without the aid of government subsidies to match up with the prices offered by the conventional sources of energy. The second generation PV technology was developed in an attempt to reduce the module cost. This generation focused on fabricating thin film modules by significantly reducing the amount of active material and involved the usage of cheaper substrates and fabrication methods. The major cells developed during this generation are hydrogenated amorphous silicon (a-Si:H), hydrogenated nanocrystalline silicon (nc-Si:H), cadmium telluride (CdTe), and copper indium-gallium diselenide (CIGS). The majority of these PV materials have direct band gaps or indirect band gap behavior suppressed by amorphous or nanocrystalline structures and exhibit high absorption coefficients. Thus it was made possible to achieve optimized efficiencies at lower thicknesses. However, the second generation PV technology suffers from many drawbacks such as long term instabilities, toxicity, and limited availability of the materials. The third generation PV technology was developed to further reduce the cost of fabrication of solar cells. New devices were developed such as multi-junction/tandem cells, quantum dot cells, intermediate band cells, hot carrier cells, organic cells, polymer solar cells, and dye-sensitized solar cells. Hybrid

active materials were developed as a combination of low-cost and conducting organic polymer films.

1.3. Cu(In,Ga)Se_2 Solar Cells

This dissertation will be primarily focused on one of the most promising thin film solar cell technologies, employing copper indium-gallium di-selenide (CIGS) as the absorber material. CIGS is an I-III-VI_2 semiconductor compound that crystallizes in a tetragonal chalcopyrite structure. In spite of the polycrystalline nature, various research groups have attained high conversion efficiencies above 22% in the recent years [7]. The standard CIGS solar cells is deposited on soda-lime glass (SLG) and consists of a Mo back contact, p-type CIGS absorber layer, n-type CdS buffer layer, and a transparent conductive oxide window layer. A typical device structure is shown in Figure 1.1. The Mo back contact is usually deposited by DC sputtering and this layer forms a non-blocking contact with CIGS layer. The CIGS absorber layer is deposited by co-evaporation process, in which all the elements are simultaneously deposited on a heated substrate. CdS buffer layer and window layers are deposited on the CIGS absorber layer by chemical bath deposition process and RF sputtering respectively. The window layer consists of a bi-layer configuration – a high resistance intrinsic ZnO layer of 80 nm thickness and a conductive layer of Al- doped ZnO layer of 200 nm thickness.

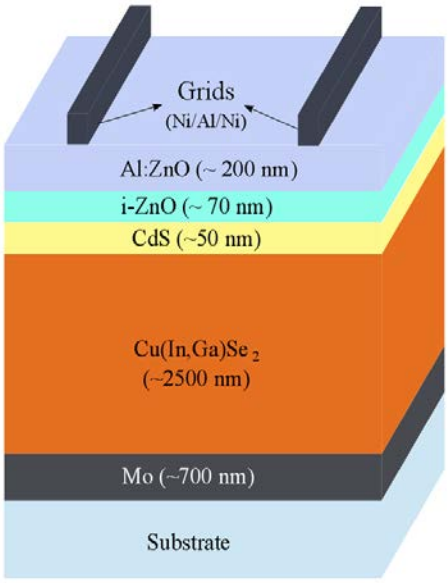

Figure 1.1: Illustration of the CIGS device structure

1.4. Fundamental of Solar Cells

A solar cell is a semiconductor device, which converts sunlight into electric power by generating current and voltage**.** Semiconductors are materials with a smaller energy gap in the distribution of allowed energy states. At a temperature of absolute zero, the electrons occupy the lowest energy states, such that all the states in the valence band will be occupied and the all the states in the conduction band are unoccupied. A pn junction or a diode is formed when a p-type and n-type semiconductor are electrically connected. The fermi level E_F of the semiconductors are at a different position with respect to the band edges and the valence band E_V and conduction band E_C bend around the interface to reach electrostatic equilibrium. The bending of the energy bands creates a large carrier concentration gradient leading to carrier diffusion. The majority carriers from the n-type semiconductors (electrons) diffuse to the p-side, leaving some of the positive donor ions (N_D^+) near the

junction uncompensated. Similarly, the majority carriers (holes) from the p-type semiconductor diffuse to the n-side leaving negative acceptor ions (N_A^-) uncompensated. Consequently, a negative space charge forms near the p-side region and a positive space charge forms near the n-side. The movement of the carriers gives rise to a diffusion current. This separation of the charge carriers creates an electric field directed from the positive charge to the negative charge, creating a drift current which opposes the diffusion current. In the absence of an external bias voltage, the drift current and diffusion current balances each other.

The ideal Shockley diode equation derived on the behavior of an ideal diode under applied voltage. The total current is the sum of the hole and electron currents at the boundaries. The current density J is defined as the current flowing per unit area,

$$J = J_0.\left(exp\left(\frac{qV}{k_BT}\right) - 1\right) \tag{1.1}$$

where J_0 is the saturation current density, q the elementary charge, k_B the Boltzmann constant and T the temperature of the device. The saturation current density is the superposition of a generation current from the n-type and p-type semiconductor and is given by

$$J_0 = -\left(J_{gen}^n + J_{gen}^p\right) = q\left(\frac{D_n n_i^2}{L_n N_A} + \frac{D_p n_i^2}{L_p N_D}\right) \tag{1.2}$$

where n_i is the intrinsic carrier density, $D_{n,p}$ are the diffusion coefficients, and $L_{n,p}$ are the diffusion lengths of electrons and holes.

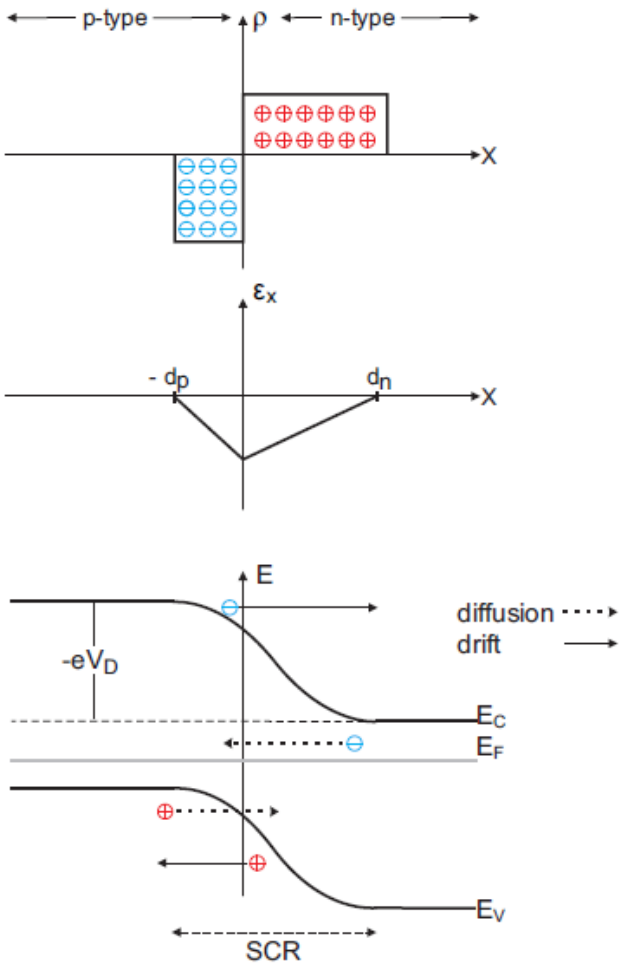

Figure1.2: Schematic of a p-n junction illustrating the space charge distribution, electric field distribution and energy band diagram [8]

Under illumination, the charge carriers are excited by the photons and the resulting electric field drives the minority carriers across the junction. The direction of photocurrent density J_{ph} is opposite to the diode current density and the modified current density is [8]

$$J = J - J_{ph} = J_0.\left(exp\left(\frac{qV}{k_BT}\right) - 1\right) - J_{ph} \quad (1.3)$$

The photocurrent density is voltage dependent because of finite lifetime of photo-generated charge carriers leading to incomplete collection of the carriers outside the SCR.

Thus the basic operation of a solar cell can be summarized as follows:

a) generation of electron-hole pairs (e-h) in semiconductor materials by absorbing the incident photon with energy (E_{ph}) greater than or equal to the band gap (E_g) of the absorbing materials,

(b) Separation of these light generated e-h pairs

(c) Collection of these carriers by appropriate electrodes.

The Single Diode Model

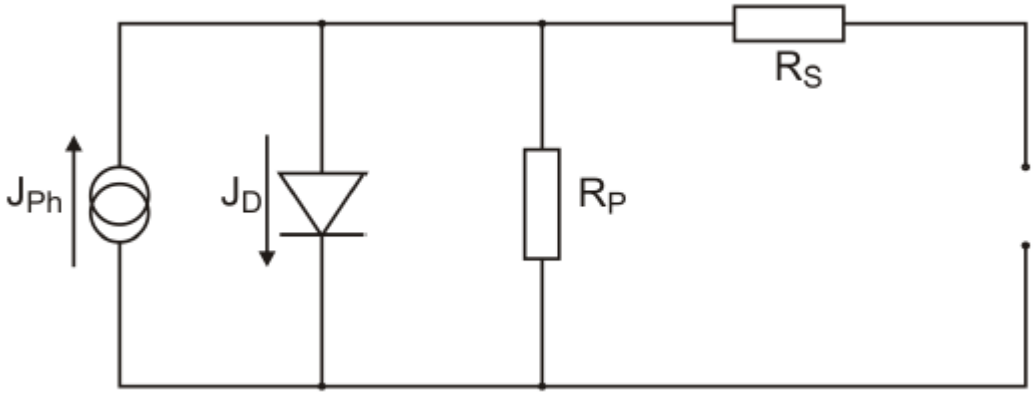

Figure 1.3: Single diode model

The current-voltage characteristics of solar cells is described using the single diode model. Figure 1.3 illustrates a single diode model, which is a good approximation to real solar cells. The series resistance R_s accounts for limitation in the current conduction due to contact resistances whereas the shunt resistance R_{sh} accounts for the leakage current through defects. The single diode model can be mathematically represented as [8]

$$J = J_0 \left(exp \left(\frac{q(V - JR_S)}{Ak_BT} \right) - 1 \right) + \frac{V - JR_S}{R_{sh}} - J_{ph} \quad (1.4)$$

where A corresponds to the diode quality factor.

Current-Voltage Characteristics

The electron transport in a solar cell can be characterized by the current density-voltage (J-V) measurements. Under standard test conditions, the illumination source has a AM1.5G solar spectrum with an intensity of 1000 W/m^2. The J-V characteristics of the solar cells measured in dark condition resemble the exponential response of a diode with higher current in the forward bias and small current in reverse bias. Under illumination, there is also a photocurrent in the cell which is in the opposite direction of the dark current and the J-V characteristics are ideally the superposition of the dark characteristics and the photocurrent. Figure 2.3 shows the J-V characteristics of solar cells under illumination and the three characteristic points obtained from the curve are open circuit voltage (V_{oc}), the short circuit current density (J_{sc}) and the maximum power point with voltage and current density of V_{MP} and J_{MP} respectively. The equations relating the above parameters to power conversion efficiency (PCE) are also given.

The short-circuit current density, J_{SC} is the current through the solar cells when V = 0, which is the similar condition as the two electrodes of the cell being short-circuited together. Because V= 0, power is the product of current and voltage, no power is generated at this point but J_{sc} marks the onset of power generation. J_{sc} of a solar cell depends on the intensity of the incident light and thus a standardized solar spectrum such as AM1.5 is used for the light measurements. The optical structure of the solar cell along with the optical properties of each layer of the structure directly influences the J_{sc} value. The value also

gives an indication of the collection probability of the photogenerated charge carriers as a function of the location of its creation.

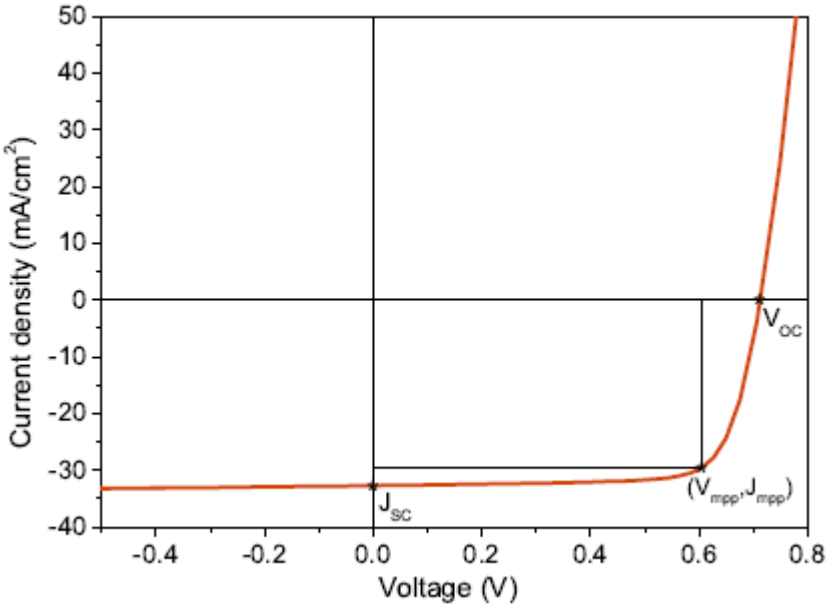

Figure 1. 4: J-V characteristics of solar cells under illumination showing the open circuit (Voc), the short circuit current density (Jsc) and the maximum power point with voltage and current density of VMP and JMP respectively [4]

The open-circuit voltage, V_{OC}, is the voltage at which no current flows across the solar cell, which is the same as the device being open-circuited. This value represents the optimum voltage that a cell can deliver. Since J= 0 there is no power produced at this point but it marks the boundary for voltages at which power can be produced. The Voc corresponds to the amount of forward bias voltage at which the dark current compensates the photo-current in the solar

cell. The V_{OC} can be calculated from an equation given below by assuming that the net current is zero.

$$V_{OC} = \frac{AkT}{q} ln\left(\frac{J_{ph}}{J_o} + 1\right) \quad (1.5)$$

Where kT/q is the thermal voltage, J_{ph} is the photocurrent density and Jo is the dark saturation current. The above equation shows that V_{OC} depends on the saturation current and light generated current in the solar cell. Since J_{ph} has a small variation, the key effect on V_{oc} is the saturation current, which may vary by orders of magnitude. The saturation current density, J_o, depends on the recombination in the solar cell so V_{oc} is a measure of the amount of recombination in the cell.

The fill factor is defined as the ratio of the maximum power ($P_{max} = J_{mp} \times V_{mp}$) generated by a solar cell to the product of V_{OC} and $J_{SC.}$

$$FF = \frac{J_{mp}V_{mp}}{J_{SC}V_{OC}} \quad (1.6)$$

FF determines the squareness of J-V curve and a higher value is desired as it indicates a higher maximum power.

The power conversion efficiency is defined as the ratio of energy output from the solar cells to input energy from the sun. The efficiency of a solar cell is determined in terms of the four different photovoltaic parameters:

$$\eta = \frac{P_{max}}{P_{in}} = \frac{J_{mp}V_{mp}}{P_{in}} = \frac{V_{OC}J_{SC}FF}{P_{in}} \quad (1.7)$$

The equation compares the impact of J_{sc}, V_{oc}, and FF on the device efficiency. Since the area used to calculate J will affect the efficiency of the cell, the inactive areas such as grids,

and interconnects should be included while calculating the efficiency for large area devices or modules.

Quantum Efficiency

In an ideal solar cell, each photon incident on the solar cell structure with an energy larger than the bandgap of the light absorbing material, will generate an electron-hole pair which is collected at the terminals of the structure. The external quantum efficiency (EQE) measures the ratio of the number of collected photo-generated carriers to the number of incident photons arriving on the solar cell at each wavelength. An absolute measurement of the EQE for an illumination spectrum, provides the J_{sc} of the solar cell. Thus, the ratio acts as a measure of the losses that accounts to a reduction of the J_{sc} from the maximum achievable photocurrent density. The major losses in Jsc can be due to the following three reasons – optical losses, recombination losses, and parasitic losses. Quantum efficiency curve for CIGS solar cells is illustrated in Figure 1.5 and the involved loss mechanisms are highlighted. The losses in detail are as follows:

1. Less than 5% losses are accounted to the shading loss from collection grids.
2. Front surface reflection losses due to the reflection at material interfaces.
3. Absorption in the window layers. Free carrier absorption in the ZnO layer can lower the quantum efficiency in the higher wavelength region ($\lambda > 900$nm).
4. Absorption in the buffer layer. The loss in quantum efficiency below $\lambda > 520$nm accounts to the thickness of the CdS buffer layer due to insufficient collection of the generated electron-hole pairs.
5. Incomplete absorption in the CIGS absorber layer near the CIGS bandgap. Photons below the bandgap are not absorbed.

6. Incomplete collection of photogenerated carriers in CIGS. This can be considered as a cumulative effect of all the above mentioned losses.

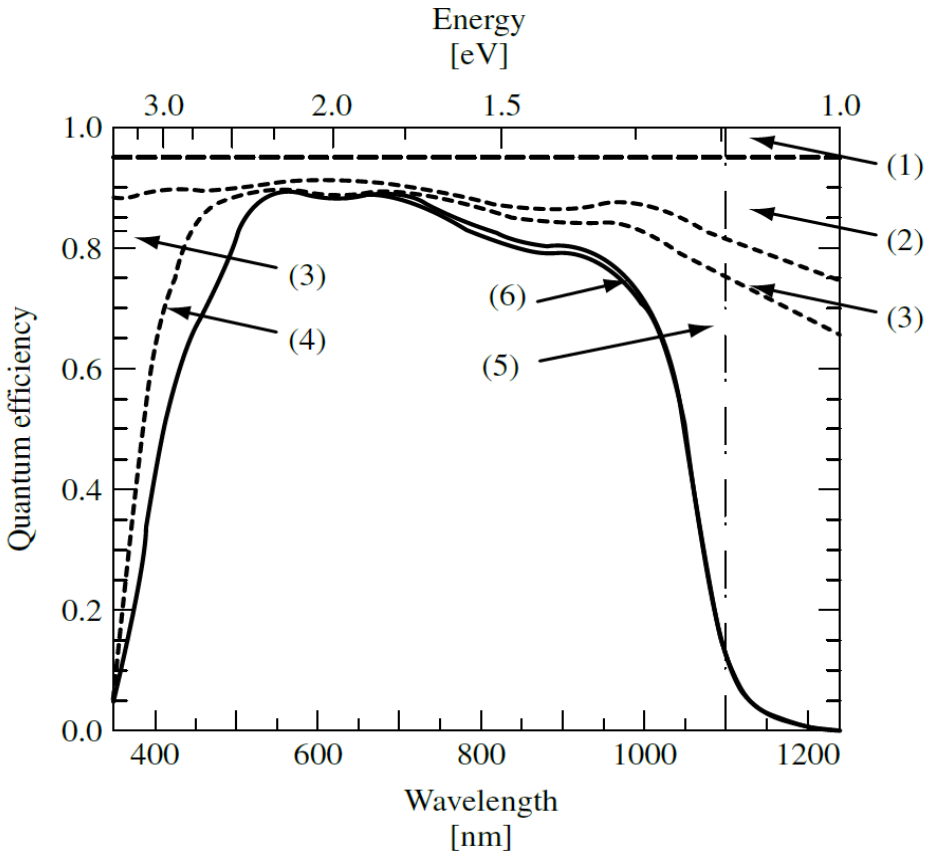

Figure 1.5: Quantum Efficiency and optical losses for CIGS solar cells [9]

1.5. Proposal Objectives and Organization

Many technology options exist nowadays to harvest the power of the sun, a sustainable energy source, and generate electricity directly from this source via the photovoltaic effect. Among them, $Cu(In,Ga)Se_2$ has gained significant momentum as a possible high efficiency and low cost thin film solar cell material. With 22.6 % efficiency, $Cu(In,Ga)Se_2$ (CIGS) solar cells are the most efficient polycrystalline thin films solar cells today. The capacity to scale up any photovoltaic technology is one of the criteria that will determine its long

term viability. However, as CIGS technology continues to increase its share of the market, the scarcity and high price of indium will potentially affect its ability to compete with other technologies. One way to avoid this bottleneck is to reduce the importance of indium in the fabrication of the cell simply by reducing its thickness without significant efficiency loss. Reducing the thickness of $Cu(In,Ga)Se_2$ thin film will not only save the material but will also lower the production time and costs. The impact of back surface recombination can increase. Thus it is important to include an effective light trapping technique to reduce the reflection losses. The results have been published in the following publications [10-16] .

In Chapter 2, describes in detail the modeling methods and characterization techniques used to analyze the CIGS device and the AR structure.

In Chapter 3, the optimization of single layer AR coating for a CIGS device based on its structure as deduced by spectroscopic ellipsometry.

In Chapter 4, the effect of absorber thickness on ultra-thin CIGS films and devices are presented and the design of multi-layer AR coating with a graded index profile for ultra-thin CIGS devices.

In Chapter 5, design of multi-layer AR coating with a high/low index profile for ultra-thin CIGS devices.

In the final chapter, a summary and conclusion of the work presented here will be given. This chapter also discusses future works and goals for further improvement of the PV device quality.

CHAPTER 2
OPTICAL MODELING OF THIN-FILM STRUCTURE

1.1. Fundamentals of Optics

When a light wave is incident on the interface between two mediums, a part of the wave will be reflected from the surface and the other part will be transmitted into the medium. A fraction of the transmitted light will be absorbed in the material depending on its optical characteristics. The optical properties of a material are characterized by its complex refractive indices and is given by

$$\tilde{n} = n - ik = \sqrt{\varepsilon_1 + i\varepsilon_2} \tag{2.1}$$

where the real part of refractive index n is the ratio of the speed of light in the medium to the speed of light in vacuum, the imaginary part k is the extinction coefficient and it relates to the absorption and ε is the complex dielectric constant or the relative permittivity. The intensity of the light transmitted through the medium gets reduced exponentially as it gets absorbed in the medium. The intensity change of the light is described by the Lambert – Beer law,

$$I(x) = I_0 e^{-\alpha x} \tag{2.2}$$

where I_0 represents the initial intensity of the incident radiation and $I(x)$ is the light intensity of the light passing through a distance x, while α is the absorption coefficient. The absorption coefficient α describes to the fraction of the light absorbed in the medium and is related to the extinction coefficient by

$$\alpha = \frac{4\pi k}{\lambda} \tag{2.3}$$

The number of electron-hole (e-h) pairs generated within the solar cell can be calculated based on Eqn 2.2 based on the assumption that the loss in intensity is directly proportional to the generation of an e-h pair. Thus, the generation rate G is obtained by deriving the change in light intensity across the cell and is given by

$$G(x) = \alpha N_0 e^{-\alpha x} \tag{2.4}$$

where N_0 is the photon flux at the solar cell surface in units of photons/unit area/s and α is the absorption coefficient and *x* is the distance into the solar cell.

Thin Film Interference

When two coherent waves travelling in the same direction superimpose with each other, they exhibit interference effects. If the two waves are in phase and have equal frequency, the magnitude of displacement is the sum of the amplitude of the waves and this phenomenon is called constructive interference. Light waves that are exactly out of phase undergo destructive interference and their amplitudes cancel with each other. Figure 2.1 represents constructive and destructive interference of two waves. The solid black line represents the first wave and the dashed line is the second wave. The solid red line represents the resultant wave.

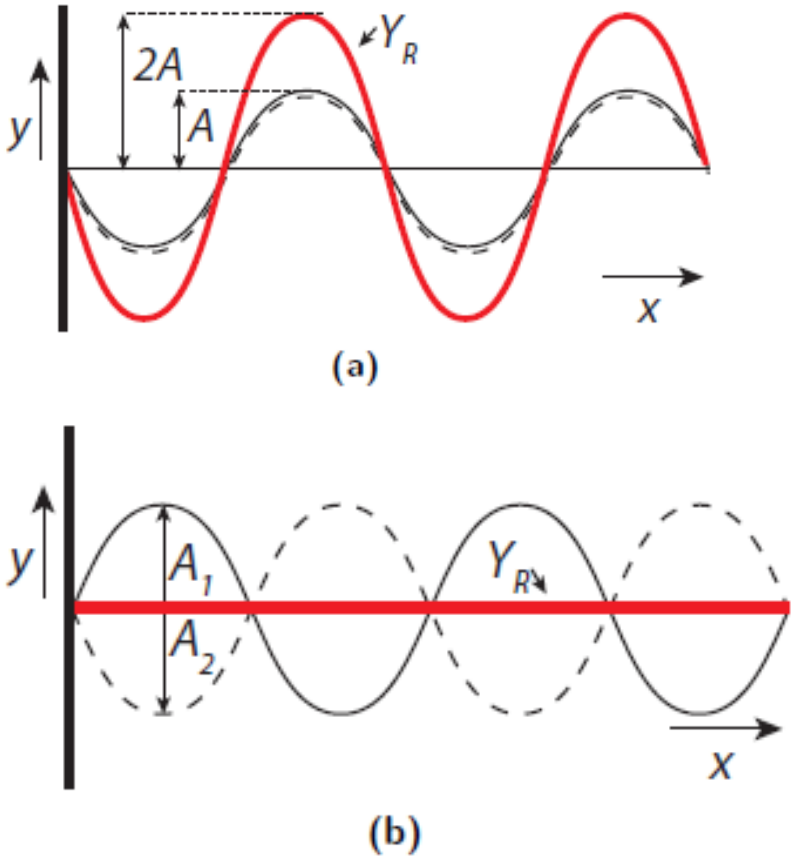

Figure 2.1: a) Constructive interference of two sinusoidal waves, b) Destructive interference [17]

1.2. Optical Modeling

Optical simulation provides guidance for optical design of solar cells through improved understanding of optical losses and gains in a multilayer solar cell structure. In order to understand the absorption within each layer, as well as the transmission and reflection from a solar cell, an optical model is needed.

2.1.1 . Spectroscopic Ellipsometry

Spectroscopic Ellipsometry has emerged as a non-destructive, non-invasive optical technique that provides a natural fit to understand and monitor the performance of thin films[18]. Ellipsometry measures the change in polarization of light as it interacts with the sample. The technique derives its name by measuring the resulting elliptically polarized light from the sample, when a beam of light with known polarization is incident on it. Ellipsometers are very sensitive to the changes in the sub-monolayers in the materials during a real time dynamic process over a wide spectral range. Regardless of the material used, this characterization technique is ideal for the measurement of the film thickness and optical constants as well as other parameters that define the quality of the film.

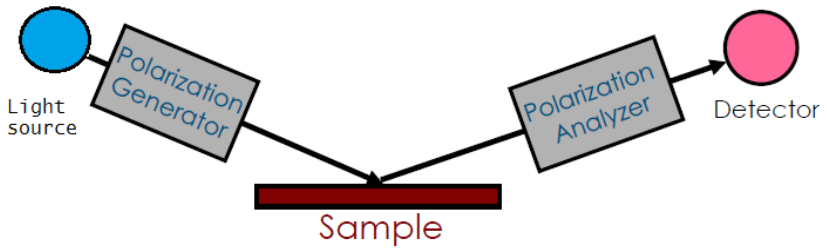

Figure 2. 2: The instrumentation for Ellipsometry[18]

The main tools used for collecting ellipsometry data includes a light source, a polarization generator, a sample, a polarization analyzer, and a detector. Figure 2.2 displays the block diagram for instrumentation. The monochromatic light source is obtained using a laser, or by using an arc lamp or by using a polychromatic source and filtering. The polarization

generator and analyzer are optical components used to manipulate the polarization. A polarization generator is used to convert the unpolarized light to linearly polarized light whereas a polarization analyzer converts the elliptically polarized light to linearly polarized light. The detector is used to measure the light intensity. The different ellipsometer configurations include rotating analyzer (RAE), rotating polarizer (RPE), rotating compensator (RCE), and phase modulation (PME). The Rotating analyzer ellipsometer configuration uses a polarizer to define the incoming polarization and then a rotating analyzer is used to analyze the outgoing light from the sample. The polarizer allows the passage of light of a preferred electric field orientation. The axis of the polarizer is oriented between the parallel and perpendicular plane such that the light falls directly on the sample. The linearly polarized light gets reflected from the sample surface as elliptically polarized light and it is passed through a rotating analyzer. In some configurations, a rotating compensator is used to shift the relative phase of orthogonal vector components resolved along the fast and slow axes of the compensator. The phase shift between the p and s componenets of the electric field vector depends on the angle of the fast axis of the compensator with respect to the field of incidence. The beam of light reflects from the sample surface thus inducing a change in the nature of the polarization state modulation. Upon specular reflection, the beams pass through a polarization analyzer and are collected by the spectograph [18].The beam splitter within the spectograph directs the low energy photons to an InGaAs photodiode array and the high energy photons to a CCD detector [19]. The detector converts the light to voltage, to determine the reflected polarization. The data thus obtained is compared to the input polarization to determine the change in polarization as reflected from the sample. This accounts to the Psi and delta measurement.

Ellipsometry Measurements

When a light wave is incident on a plane, some of the light is reflected and some gets transmitted. The plane polarized waves in the plane of incidence are known as parallel waves (‘p’ waves) and the plane polarized waves perpendicular to the plane of incidence are known as perpendicular waves (‘s’ waves, ‘s’ is taken from the German word “senkrecht” which means perpendicular). Ellipsometry deals with the change of ‘p’ and ‘s’ components on reflection or transmission in relation to each other [20].

Fresnels equations describes the amount of light reflected and transmitted at an interface between the materials. The Fresnel reflection coefficient r is the ratio of the amplitude of the reflected wave to the amplitude of the incident wave for the single interface and the coefficients are given by [18]

$$r_s = \left(\frac{E_{0r}}{E_{0i}}\right)_s = \frac{n_i \cos(\phi_i) - n_t \cos(\phi_t)}{n_i \cos(\phi_i) + n_t \cos(\phi_t)} \tag{2.5}$$

$$r_p = \left(\frac{E_{0r}}{E_{0i}}\right)_p = \frac{n_t \cos(\phi_i) - n_i \cos(\phi_t)}{n_i \cos(\phi_t) + n_t \cos(\phi_i)} \tag{2.6}$$

Reflectance is defined as the ratio of the reflected intensity to the incident intensity. For a single interface, the reflectance for parallel and perpendicular incident waves are given by [19],

$$R^P = |r^P|^2 \tag{2.7}$$

$$R^S = |r^S|^2 \tag{2.8}$$

A known polarization is reflected or transmitted from the sample and the output polarization is measured. The ellipsometer measures the change in polarization expressed as a complex ratio [20],

$$\rho = \tan(\psi)\, e^{i\Delta} \tag{2.9}$$

where Ψ is the amplitude ratio and Δ represents the change in phase difference between the p- and s- polarizations respectively. Fig. 15 explains the principle of measurement of ellipsometry. The phase difference between the parallel component and the perpendicular component of the incident wave is δ_1. The phase difference between the parallel component and the perpedicular component of the reflected wave is δ_2. Thus the change in phase difference is expressed as $\Delta = \delta_1 - \delta_2$ and its value can change from 0° to 360° [19].

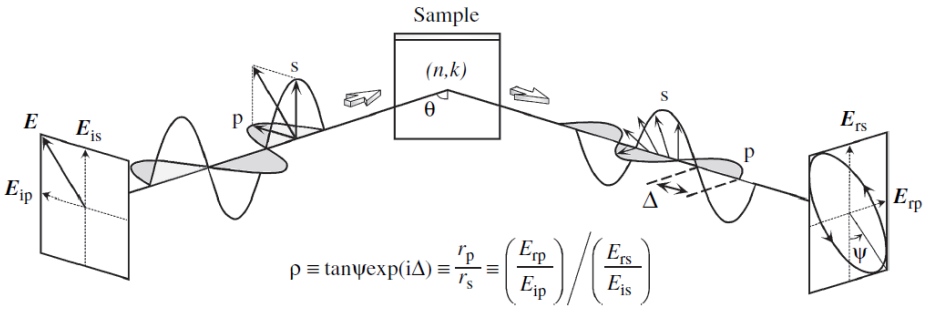

Figure 2. 3: Measurement principle of Ellipsometry [12]

Regarding the amplitude, the perpendicular and parallel components may change upon reflection. The ratio of the amplitude of the reflected wave to the amplitude of the incident wave for the parallel and perpendicular components are given by $|R^P|$ and $|R^S|$. Thus the amplitude is defined as $\tan\Psi = \frac{|R^P|}{|R^S|}$. The value of Ψ can vary from 0° to 90° [19].

Ellipsometry measures the change in light polarization and determines the sample's material properties such as film thickness and optical constants. Pseudo optical constants can be derived from the ellipsometry measurement for the bulk materials [18]. Figure 2.4 shows the data analysis procedure in spectroscopic ellipsometry.

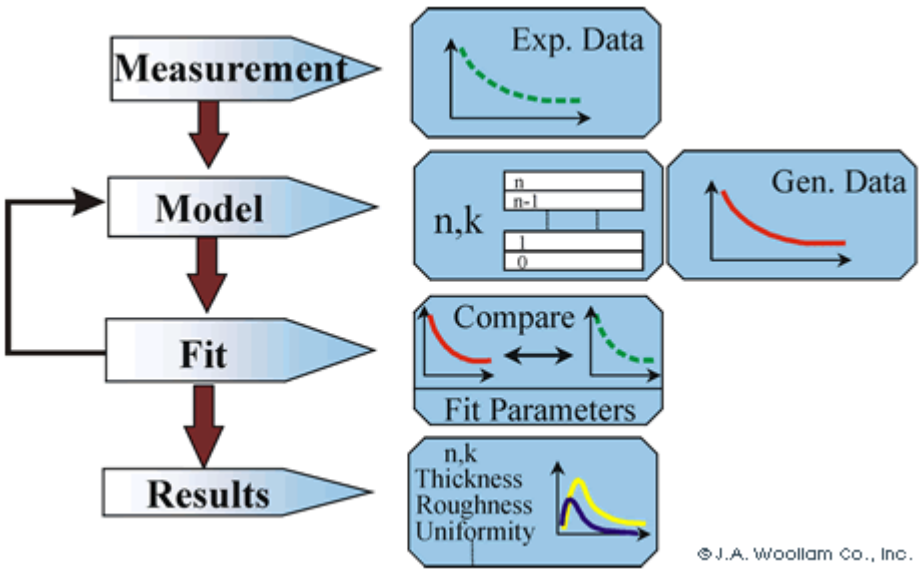

Figure 2.4: Flowchart for Ellipsometry analysis[18]

After measurement of the data, an optical model is constructed corresponding to the sample. For a sample structure with known component materials and dielectric functions, an optical model is constructed by placing the layers in the right sequence including the thickness and optical properties of each layer. If the dielectric functions of the material are not available, different dielectric function models are used to mathematically analyze the layers. For dielectric function modeling in a transparent region, Sellmeier or Cauchy models are used. A Drude model is used to analyze free carrier absorption. Various models

such as Lorentz model, Tauc-Lorentz model, harmonic oscillator approximation (HOA), and model dielectric function (MDF) are used to express the electric polarization in the visible/UV region. Intermix layers and void fractions can be analyzed to improve the correlation with the theoretical and experimental techqniques. The predicted response is calculated from the Fresnel's equations using the optical model and the response describes the material's thickness and optical constants. The calculated values are compared with the experimental data. Regression is used to find the best match between the model and the experimental data. A least square regression algorithm is used to minimize the differences between the generated spectra and the experimental data by adjusting the variable parameters in the model. Mean Squared Error (MSE) is taken as an estimator to represent the quality of the match between the generated data and experimental data. MSE is written as

$$MSE = \sqrt{\frac{1}{2N-M}\sum_{i=1}^{N}\left[\left(\frac{\psi_i^{\mathrm{mod}}-\psi_i^{\mathrm{exp}}}{\sigma_{\psi,i}^{\mathrm{exp}}}\right)^2+\left(\frac{\Delta_i^{\mathrm{mod}}-\Delta_i^{\mathrm{exp}}}{\sigma_{\Delta,i}^{\mathrm{exp}}}\right)^2\right]} \qquad (2.10)$$

where N is the number of (ψ, Δ) pairs, M is the variable parameters in the model and σ is the standard deviation of the experimental data. The unknown parameters are varied till a minimum MSE is obtained.

The thickness of the film and the optical constants are the main data that are extracted using the Ellipsometry process. The complex dielectric constant ε and the absorption constant α can also be obtained from the optical constants. Also, the reflectance (R) and the transmittance (T) at different angles of indicidence can be calculated from the thickness [21]. The film thickness is determined by the interference between the light

travelling through the film and the light reflected from the surface. The optical constants n and k should also be determined along with the thickness to obtain accurate results. The thickness of the film will indicate the length of the path travelled by the light through the film. The index determines the velocity of the light wave through the sample and the refracted angle. But the optical constants will vary for different wavelengths. Thus it is important to obtain the constants at all wavelengths. A dispersion relationship is used to explain the optical constants versus wavelength [22].The parameters of the relationship allow the overall constants to match the experimental results. The model can be optimized to the measured data by varying the wavelength independent parameters such as angle of incidence, adjusting the layer thickness, adding Lorentz parameters, EMA fractions and amorphous semiconductor parameters [22].

2.2.2 Transfer Matrix Theory Modeling

In this optical model, the illumination light source generates a plane wave that is normally incident on the multilayer structure. All interfaces are assumed to be parallel. The coherence length is assumed to be long compared to any thin film thicknesses, but short compared to the thickness of the glass superstrate in the case of superstrate solar cells. Thus, in multi-beam interference calculations, the light waves are assumed to be coherent and thus add coherently in all layers except the thick superstrate. With respect to their optical properties, material media in each layer may be lossy but are otherwise assumed to be linear, non-magnetic, isotropic, and homogeneous within each layer. The optical interference and absorption in the CIGS solar cell multi-layer stack was calculated using a Transfer Matrix Theory model developed on a Matlab platform. In a coherent multilayer structure, the light waves are assumed to be planar and transversal such that the magnitudes

of the electric field components in each layer can be sufficiently used to calculate the irradiance and absorption [23]. Consider a light wave normally incident on a multilayer structure composed of *n* layers as illustrated in Figure 2.5. At each interface, the waves will be propagating in both forward and reverse directions owing to multiple reflections and transmissions. Maxwell's equation with appropriate boundary conditions can be applied to find the coefficients of reflection and transmission at each interface [24]. The reflections at the interface affect the distribution of the optical electric field and this directly influences the generation of the charge carriers. The electromagnetic wave of the specular light in the multi-layer stack can be described by the amplitudes of the electric field E. At any point in the layer *m*, the electric field is represented by four components (Figure 2.5). The light wave electric field magnitude propagating in the m^{th} layer can be expressed as

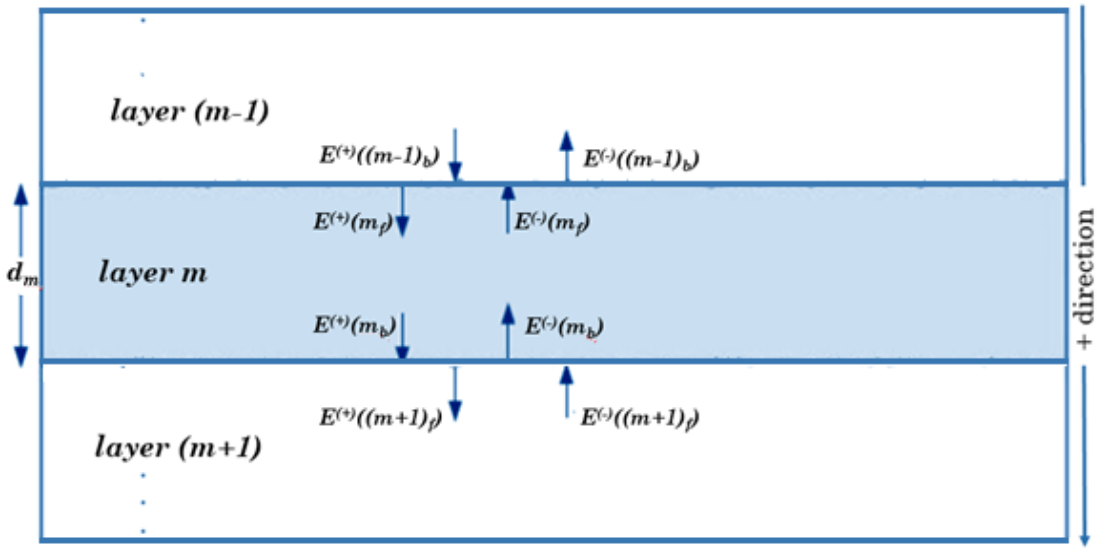

Figure 2. 5:A general multi-layer structure having n layers of thickness d_m

$$E^{(+)}(m_f) = E^{(+)}((m-1)_b).t_{m-1,m} + E^{(-)}(m_f).r_{m,m-1} \quad (2.11)$$

$$E^{(-)}(m_f) = E^{(-)}(m_f).\tau_m \quad (2.12)$$

$$E^{(+)}(m_b) = E^{(+)}(m_f).\tau_m \quad (2.13)$$

$$E^{(-)}(m_b) = E^{(-)}((m+1)_f).t_{m+1,m} + E^{(+)}(m_b).r_{m,m+1} \quad (2.14)$$

where m corresponds to each layer (ranging from 1,2...n); subscripts f corresponds to the front (top in the Figure) and b to the bottom of the layer; + and - corresponds to the positive and negative direction; τ_m is the phase thickness of each layer; r_m and t_m correspond to the Fresnel's coefficients. The complex index of refraction of the m^{th} layer N_m, can be related to the real refractive index n_m and the extinction coefficient k_m as $N_m = n_m - ik_m$. The Fresnel's coefficients relate the amplitude of the reflected and transmitted electric field magnitudes to the amplitude of the incident electric field [25].

Under illumination, four electric field amplitudes are associated with each interface for the multi-layer structure. Let $E^{(+)}(m_f)$ denotes the electric field magnitude of light wave that is incident on top of the m^{th} interface travelling in a forward direction, $E^{(-)}(m_b)$ the electric field magnitude of light wave that is incident on the m^{th} interface travelling in the backward direction, $E^{(+)}(m_b)$ the electric field magnitude of light wave that leaves the m^{th} interface travelling in a backward direction and $E^{(-)}(m_f)$ the electric field magnitude of light wave that leaves the m^{th} interface travelling in the forward direction. The matrix representation of electric field magnitude of light wave propagating in the m^{th} layer can then be expressed by:

$$\begin{bmatrix} E^{(+)}(m_b) \\ E^{(-)}(m_b) \end{bmatrix} = L_{m+1} \begin{bmatrix} E^{(+)}((m+1)_b) \\ E^{(-)}((m+1)_b) \end{bmatrix} \quad (2.15)$$

where L_{m+1} denotes the layer matrix that calculates the amplitudes in the consecutive layers. Layer matrix can be explained as the matrix multiplication of the interface matrix (I_{m+1}) and propagation matrix (P_{m+1}). The propagation matrix (P_{m+1}) calculates the electric field amplitudes across the (m+1) layer and the interface matrix (I_{m+1}) calculates the electric field amplitudes across the $m/(m+1)$ layer and can be expressed as follows:

$$P_{m+1} = \begin{pmatrix} e^{-\frac{2\pi N_{m+1} d_{m+1}}{\lambda_0}} & 0 \\ 0 & e^{\frac{2\pi N_{m+1} d_{m+1}}{\lambda_0}} \end{pmatrix} \tag{2.16}$$

$$I_{m+1} = \frac{1}{t_{m,m+1}} \begin{pmatrix} 1 & -r_{m+1,m} \\ r_{m,m+1} & (t_{m,m+1}.t_{m+1,m} - r_{m,m+1}.r_{m+1,m}) \end{pmatrix} \tag{2.17}$$

$$L_{m+1} = P_{m+1}.I_{m+1} \tag{2.18}$$

The relationship between the incident, reflected, and transmitted amplitudes can be expressed by [26]

$$\begin{bmatrix} I \\ R \end{bmatrix} = \begin{bmatrix} E^{(+)}(1_f) \\ E^{(+)}(1_b) \end{bmatrix} = I_1 \begin{bmatrix} E^{(-)}(1_f) \\ E^{(-)}(1_b) \end{bmatrix} = I_1 P_1 \begin{bmatrix} E^{(+)}(2_f) \\ E^{(+)}(2_b) \end{bmatrix} = I_1 P_1 I_2 \begin{bmatrix} E^{(-)}(2_f) \\ E^{(-)}(2_b) \end{bmatrix} \tag{2.19}$$

$$\begin{bmatrix} I \\ R \end{bmatrix} = I_1 P_1 I_2 \ldots . I_n P_n I_n \begin{bmatrix} E^{(-)}(n_f) \\ E^{(-)}(n_b) \end{bmatrix} = \begin{bmatrix} S_{11} & S_{12} \\ S_{21} & S_{22} \end{bmatrix} \begin{bmatrix} T \\ 0 \end{bmatrix} \tag{2.20}$$

The structure matrix for the coherent propagation of light for n-coherent layers, S_n, calculates the electric field amplitudes across the entire multilayer structure [26]. The zero in the column vector is due to the fact that there is no wave incident on the n^{th} interface travelling in the backwards direction [27],[28]. The energy density of the electric field is then calculated using the Poynting's vector, S, given by:

$$S(m_f) = \left(\frac{1}{2} Y_0 n_m \left|E^{(+)}(m_f)\right|^2\right) - \left(\frac{1}{2} Y_0 n_m \left|E^{(-)}(m_f)\right|^2\right)\left(Y_0 \kappa_m . I_m \left(E^{(-)}(m_f).\left(E^{(+)}(m_f)\right)^*\right)\right)$$

(2.21)

$$S(m_B) = \left(\frac{1}{2} Y_0 n_m \left|E^{(+)}(m_b)\right|^2\right) - \left(\frac{1}{2} Y_0 n_m \left|E^{(-)}(m_b)\right|^2\right)\left(Y_0 \kappa_i . I_m \left(E^{(-)}(m_b).\left(E^{(+)}(m_b)\right)^*\right)\right)$$

(2.22)

where Y_0 is the optical admittance of the free space. The 1st term of the Poynting's vector represents the intensity of the waves propagating in the positive direction, the 2nd term is the intensity in the negative direction and the 3rd term represents the interference component between the two. Thereafter, absorption in each layer is calculated from the Poynting's vectors by:

$$A_m = \frac{2}{n_{air} . Y_0}\left[S(m_f) - S(m_b)\right] \quad (2.13)$$

The Quantum efficiency (QE) spectrum for the CIGS device can be predicted from the optically deduced light absorption in the active components and thus the short-circuit current density, J_{SC}, can also be deduced from this model. This optical model requires precise parameters – optical absorption coefficient, refractive index and thickness of all the layers within the multi-layer structure – which are extracted using SE.

2.2.3 Optical Modeling – Reflectance Model

As light propagates from one medium into another medium with different optical properties, part of the light is reflected and some is transmitted. The preliminary mathematical model of reflection and transmission can be formulated using Fresnel equations. In a multi-layer film structure, the coherent waves reflected between the interfaces interfere as described as follows:

$$A = A1sin(wt) + A2\,sin(wt + \Delta) \tag{2.24}$$

The optical path difference Δ is the equal to the product of the geometrical path difference of the light and the refractive index of the film. Destructive interference occurs at a phase difference, $\Delta = m\pi$, *m* be any integer, reducing the amplitude of the light to a minimum. The thickness of the AR coating should be chosen such that destructive interference occurs between the light reflected from the module interface and the AR coating surface and in this way reflections at the specific design wavelength are eliminated. This leads to the condition that the AR layer thickness should equal one quarter of the wavelength within the coating, or $d = \lambda/4 = \lambda_0/4n$, where λ_0 is the wavelength of the wave in vacuum. This type of coating is referred to as the 'V' coating since the reflection is reduced at a chosen wavelength and rises rapidly at the either ends. The AR coatings are made more efficient by choosing multi-layer AR coatings as the anti-reflection effect is extended across a wavelength range due to the presence of the coupled medium boundaries. The performance of the AR coating is improved by selecting materials with a wide difference of refractive index and also by adjusting the thickness of each layer.

An optimization model was developed based on the reduction of average reflectance, thus maximizing the optical absorption in the active layer on Matlab platform. The optical properties and of each layer of the CIGS solar cell structure was obtained by analyzing the data measured using ex-situ variable angle of incidence SE. The reflectance of the solar cell structure was calculated based on a recursive approach of the optical admittance Y,

$$Y_i = \frac{jN_i \sin(\delta_i) + Y_{i-1}\cos(\delta_i)}{\cos(\delta_i) + j\frac{Y_{i-1}\sin(\delta_i)}{N_i}} \tag{2.25}$$

The phase thickness of the layer, $\delta_i = \frac{2\pi N_i d cos\theta_i}{\lambda}$, where N_i and d is respectively the complex index of refraction and thickness of each layer. We assume normal incidence, so $cos\theta_i$=1.

The reflectance of the total structure is defined by

$$R = \left|\frac{1-Y}{1+Y}\right|^2 \tag{2.26}$$

The average reflectance of the solar cell structure for a given spectral range is calculated by[4]

$$AvR = \frac{1}{\lambda_{max}-\lambda_{min}} \int_{\lambda_{min}}^{\lambda_{max}} R(\lambda) d\lambda \tag{2.27}$$

2.3 Other Characterization Techniques

2.3.1 Transmission and Reflectance Measurements

The most common method of determining the band gap of a semiconductor is by transmission and reflection measurement. The transmission and reflection coefficients of the semiconductors are normally measured in the wavelength range from 200-2500 nm. Then the absorption coefficient can be calculated from transmission and reflection coefficients using the relation [20]

$$\alpha = \frac{2\ln(1-R) - \ln(T)}{d} \tag{2.28}$$

Where α is the absorption coefficient, d is thickness of the thin film, R is the reflection and T is the transmission. Once α is calculated, then the band gap of any direct band gap semiconductors can be extracted by plotting $(\alpha h\upsilon)^2$ vs. hυ and by extrapolating the linear portion of the curve to the hυ axis. The intersection of this linear extrapolation with the hυ axis gives the band gap.

2.3.2 X-ray Diffraction (XRD)

X-ray diffraction is a rapid analytical technique used to probe the crystalline phases present in materials and to measure the structural properties such as grain size, preferred orientation, and defect structure of the phases. When a collimated beam of X-rays is directed at the sample surface, the material of the sample causes the X-rays to be diffracted at various angles based on its crystal structure. The diffraction spectrum of the samples is then plotted as a function of 2θ. When Bragg's law ($2d \sin\theta = n\lambda$) is satisfied, diffraction peaks appear. The diffraction angle, the number of peaks, and their intensity depend on the crystal structure, symmetry and lattice constant. Comparing the peaks with XRD database gives the phase, crystal orientation, lattice constants, and other information. The inter-planar spacing, d_{hkl}, corresponding to each diffraction line, is calculated by the following equation:

$$d_{hlk} = \frac{\lambda}{2Sin\theta} \tag{2.29}$$

where θ is Bragg's angle of diffraction and λ is the wavelength of the X-rays radiation. XRD data can also be used to predict the crystallites size using Scherrer formula [29].

$$L = \frac{K_s \lambda}{\beta \cos\theta} \tag{2.30}$$

where L is the grain size, K_s is Scherrer constant (usually set at 0.9 for spherical particles), β is the full width at half maximum of the peak in radians, λ is the wavelength of the X-ray beam and 2θ is the peak position.

The X-rays penetration depth can be varied by varying the angle of incidence of the x-rays beam. With a bigger angle it is possible to see the material composition deeper into the sample. For $Cu(In,Ga)Se_2$ compounds, since the lattice parameters for different Ga/(In+Ga) are already known, XRD can also be used to find the Ga/(In+Ga) value in the film. Sometimes, it is not desired to probe deeply into the film or not possible to get a good signal if the film is too thin. To counteract this, grazing incident XRD (GIXRD) can be used. This is basically a low angle XRD, which changes the penetration depth of the X-ray by fixing the incident angle from 1 to 10 degrees while moving the detecting arm.

2.3.3 Atomic Force Microscopy (AFM)

AFM is one type of scanning probe microscopes, which is used to obtain surface structures images (on an nm or even sub-nm scale) and other information. In AFM, a probe is maintained in close contact with the sample surface by a feedback mechanism as it scans over the surface, and the movement of the probe to stay at the same probe-sample distance is taken to be the sample topography. Generally, a cantilever made of Si or SiN is used to probe the surface of the sample by adjusting the position via control implementations. The tip of the cantilever is kept in continuous or intermittent contact with the sample surface and the cantilever is translated over the sample using a piezocontroller. A laser is reflected on the back surface of the cantilever as a scan is in progress. Whenever the laser changes its positions due to force on the cantilever, a voltage is applied to the piezoelectric to make the laser go back to its origin. The voltage corresponds to the height of surface features,

since the force on the cantilever is caused by the features on the specimen. A precise calibration between the height and the voltage is accomplished by using a sample with known structure. AFM can be used in three main different modes of imaging depending on the interaction of the surface and the tip. In contact mode, the tip of the AFM probe is always kept in contact with the surface whereas the tip never touches the sample in non-contact mode measurement. During contact with the sample, the probe predominately experiences repulsive Van der Waals forces. As the tip moves further away from the surface (non-contact mode) attractive Van der Waals forces are dominant. Contact mode AFM is good for rough samples but it damages soft surfaces whereas the non-contact mode has bad resolution and usually needs ultra-high vacuum (UHV) to have best imaging. In tapping mode, the imaging is similar to contact mode however in this mode, the cantilever is oscillated at its resonant frequency via the piezoelectric crystal attached to the tip holder. During the oscillation, the probe tip keeps moving towards the surface till it lightly taps on the surface. As soon as there is contact between the tip and the surface, there is loss in the oscillation amplitude, which is used to find the topographic changes. This technique allows high resolution and is good for soft surface.

2.3.4 Scanning Electron Microscopy (SEM)

Scanning electron microscopy utilizes an electron beam to produce a highly magnified image of the sample. A SEM consists of an electron gun, a lens system, scanning coils, an electron collector, and a cathode ray display tube (CRT). In SEM, larger magnification is possible over optical microscopic since electron wavelengths are much smaller than photon wavelength and a large field of view is possible since the electron beam is small, which allows three-dimensional study of a specimen’s surface. The focused

electrons interact with the atoms in the specimen producing a number of different types of signals, which contains data about the specimen's surface morphology, composition, and other properties such as electrical resistivity. The induced signals by an SEM include secondary electrons, back-scattered electrons (BSE), characteristic X-rays, photons as well as specimen current, and transmitted electrons. All these signals can be detected and amplified to control the brightness of a CRT scanned in synchronism with the sample beam scan in the SEM. Electron with energies 0-30 eV are detected and used to form the image in secondary electron mode. These electrons are knocked out from within a few nanometers of the surface of the specimen. Backscattered electrons are electrons from the electron beam that are elastically scattered back from the sample and provides the information about the bulk properties of the materials since such scattering takes place in a volume extending down to 0.5 μm below the surface of the specimen.

CHAPTER 3
SINGLE LAYER ANTI-REFLECTIVE COATINGS

3.1 Introduction and Motivation

Over the past few years, thin film solar cells based on $Cu(In,Ga)Se_2$ (CIGS) have developed into a new realm of high efficiencies after major revisions and alterations of the CIGS deposition process. Several laboratories have been able to produce record devices over 22% efficiency [7, 30]. As the absorber and buffer layers properties are modified with each enhancement, it is also important to continue developing a better and effective light trapping mechanism. The overall reflection losses can be minimized to a great extent by applying an efficient anti-reflective (AR) coating, thus increasing the power conversion efficiency of the device. Magnesium fluoride (MgF_2) is the most widely used material for AR coatings in CIGS solar cells because it forms high quality films and has a low refractive index, *n* [31]. However, the material by itself is not sufficient, and a careful deposition process, leading to a precise thickness, is paramount to the success of the AR coating. The thickness of the AR coating should be chosen such that destructive interference occurs between the light reflected from the CIGS cell interface and the AR coating surface, allowing reflections at the specific wavelength to be eliminated. This leads to the condition that the AR layer thickness should equal one quarter of the wavelength within the coating, or $d = \lambda/4 = \lambda_0/4n$, where λ_0 is the wavelength of the wave in vacuum [32]. As more research is being implemented to push the limitations in energy conversion of the devices, improvements are made in the device structure or process parameters to optimize the device

efficiency (thinner CdS or AZO) or to reduce the cost of the process (thinner absorber layer), and the role and importance of the AR coating during these changes need to be assessed. In this paper, we described several ways to model accurately the effect of various layers on the thickness of the AR coating, and implement ways to deposit effectively the appropriate thickness using various means.

3.2 Experimental Details

The devices were grown on molybdenum coated soda lime glass substrates. CIGS absorber layers were deposited by a 3-stage process in a high vacuum, co-evaporation chamber. After the CIGS process, the samples were dipped into a chemical bath to form a thin layer of CdS buffer layer. High resistive ZnO layers along with Al:ZnO layers were deposited by RF sputtering to obtain a transparent window layer. Finally, Ni/Al/Ni grids were evaporated by e-beam evaporation for the electrical contacts. MgF_2 layers were deposited as the anti-reflective coating on the CIGS solar cells by e-beam evaporation and variations in relative reflectance were obtained for different wavelengths during the course of deposition by Real Time Spectroscopic Ellispometry (RTSE). The RTSE measurements were carried out *in-situ* during film growth while the spectroscopic ellipsometry measurements were carried out *ex-situ*. They both used a rotating compensator, multichannel instrument with an energy range of 0.75–6.5 eV at an angle of incidence of 65°. Quartz crystal monitors were used to accurately monitor the deposition rate of the MgF_2 film during the deposition.

3.3 Optical modelling of Single layer AR coating

There are many ways of depositing an AR coating with optimal thickness on a CIGS solar cell. The most typical one is to assume that all layers are optimal and of typical

thicknesses and therefore to deposit a MgF_2 layer of a fixed thickness. Even high efficiency solar cells have MgF_2 thickness varying extensively, ranging from 100 -105 nm[33-35]. Here three other methods are proposed, with an increasing level of precision: (i) the 1st method allows the prediction of the thickness to be deposited based on a transfer matrix theory (TMT) modeling combined with spectroscopic ellipsometry (SE) measurements; (ii) the 2nd one is based on real time optimization via *in-situ* RTSE; (iii) the 3rd one is a combination of prediction via TMT and real time optimization via *in-situ* RTSE measurements.

3.3.1 Application of the TMT & SE Method to a CIGS Solar Cell

The optical properties and structure of each individual layer in the CIGS solar cell structure were characterized using ex-situ spectroscopic ellipsometry (SE). Figure 3.2 shows the structural model used here for analysis of ellipsometric spectra and results of analysis for ex-situ measurements of a typical glass/Mo/CIGS/CdS/ZnO/ZnO:Al film stack. The bulk and the surface roughness thicknesses of the structure were determined by least squares regression analysis of a single pair of ellipsometric spectra [36]. For the analysis of the SE data, the simplest model with the least number of fitting parameters was considered. The complex dielectric function spectra of the layers were obtained by deposition of the materials on well-characterized native oxide coated silicon wafer substrates. The surface roughness or interface roughness layers were not considered in the basic starting model. The root-mean squared error (MSE) was estimated by [37]:

$$MSE = \sqrt{\frac{1}{3n-m}\sum_{i=1}^{n}\left[\left(N_i^{(exp)} - N_i^{(cal)}\right)^2 + \left(C_i^{(exp)} - C_i^{(cal)}\right)^2 + \left(S_i^{(exp)} - S_i^{(cal)}\right)^2\right]} \times 1000$$

(3.1)

where $N=cos2\psi$, $C=sin2\psi\ cos\Delta$, $S=sin2\psi\ sin\Delta$, n is the number of data points and m is the number of fit parameters. A step-by-step MSE reduction method was applied to improve the model. The surface roughness and interface layers were modeled using the Bruggeman effective medium approximation as a mixture of the overlying and underlying materials. Experimental ψ and Δ are shown in Figure 3.1 along with the best model fit and the final result analysis for a specific structure.

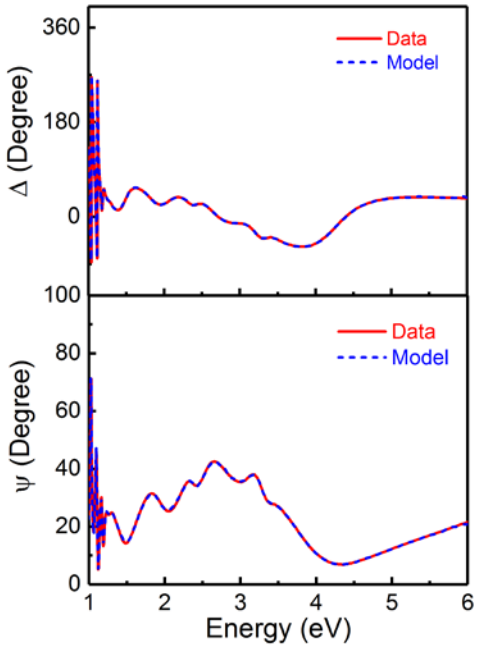

Surface roughness (f_v=30.6 %)	34.29 nm
ZnO:Al (f_v=2.9%)	111.97 nm
ZnO:Al/i-ZnO (f_{ZnO}=21.8 %, f_v=2.9 %)	140.08 nm
i-ZnO (f_v=0.0 %)	36.23 nm
i-ZnO/CdS (f_v=48.6%)	44.47 nm
CdS (f_v=0.0 %)	48.67 nm
CdS/CIGS (f_v=77.5 %)	59.12 nm
CIGS (Graded layer, (f_v=0.0 %)	2177.73 nm
CIGS/Mo (f_{Mo}=82.0 %)	19.89 nm
Mo (opaque)	

Figure 3. 1:(a). Experimental spectra in ψ and Δ along with the best fit for a specific CIGS device without AR layer along with the final result analysis (b).

The optical properties thus obtained were used to model the reflectance, transmittance, and absorbance losses in each layer. MgF_2 was chosen as the material for AR optical coating on top of the CIGS solar cells. The film was deposited by e-beam evaporation on well-

characterized silicon wafers. The index of refraction and extinction coefficient of the material, as deduced by SE, are shown in Figure 3.2.

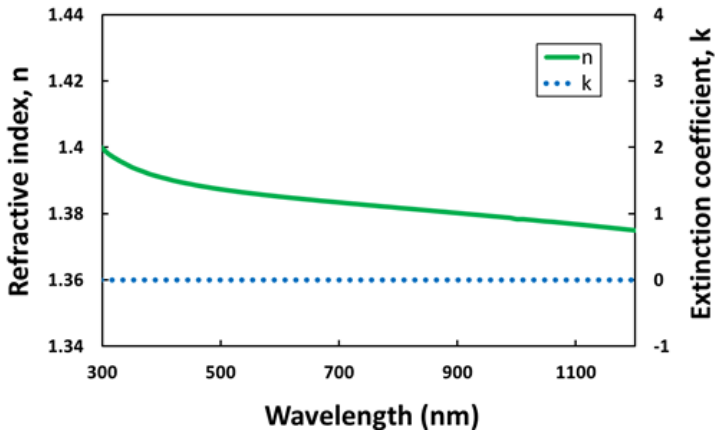

Figure 3. 2:Index of refraction n and extinction coefficient k for MgF_2, as deduced by ex-situ variable angle of incidence spectroscopic ellipsometry measurements

An optimization model was developed based on the reduction of average reflectance, thus maximizing the optical absorption in the active layer. The modelling was performed for a CIGS absorber layer of thickness 2.5 µm with one layer of MgF_2. The MgF_2 layer was deposited on the CIGS solar cell by e-beam evaporation and variations in reflectance were obtained for different wavelengths during the course of deposition. The RTSE measurements were carried out *in-situ* during film growth using a rotating compensator, multichannel instrument with an energy range of 0.75–6.5 eV at an angle of incidence of 65°.

Once the thickness and the optical properties of the component layers of the solar cell were extracted with SE, the maximum external quantum efficiency (QE) and short circuit current density (J_{sc}) were calculated by assuming perfectly specular reflection/transmission conditions[38]. Also, the reflectance spectra from the structure can be predicted using this

model, which helps in optimizing the AR coating. The simulation of QE spectra is based on the assumption that all the photo-generated carriers within the active layers are collected without any recombination. Thus, a comparison between the simulated QE and experimental QE obtained from the measurement of a completed solar cell device can also provide information on the electronic losses, as well as the spectral dependence of the losses. Furthermore, the optical model does not take into consideration the scattering of light at rough surfaces and interfaces, thus the modeled QE spectra can provide insight into the gain due to light trapping caused by scattering at rough surfaces and interfaces.

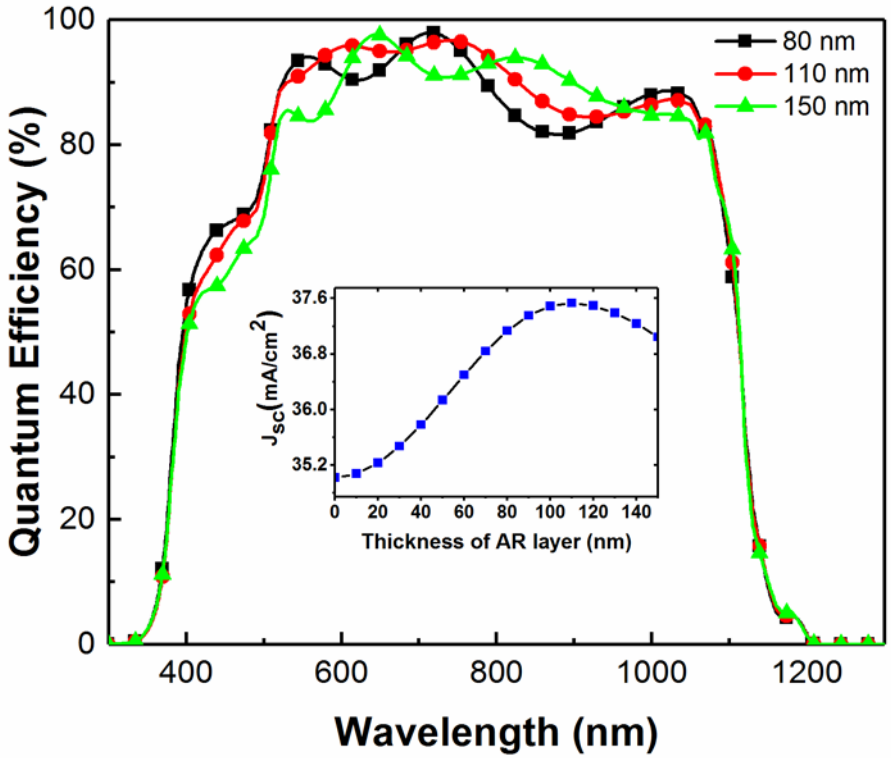

Figure 3. 3:Simulated QE and J_{SC} for various thickness of the AR layer for the CIGS solar cell characterized by SE

This optical model was applied to predict the maximum obtainable J_{sc} for the cell previously analyzed by SE. The variation of the QE curve and J_{sc} versus the thickness of the AR layer shows that a maximum J_{sc} is predicted for an MgF_2 layer of thickness around 114 nm for the mentioned CIGS device structure (Figure 3.3).

The model was then verified experimentally, by depositing a 114 nm MgF_2 layer on top of the CIGS solar cell stack. The calculated results and the experimentally measured results were then compared, showing excellent correlation between the two (Figure 3.4). The main difference appears from 500 nm to 1000 nm, where the simulated data shows interference fringes, contrarily to the measured data, due to the smooth surface used for simulation.

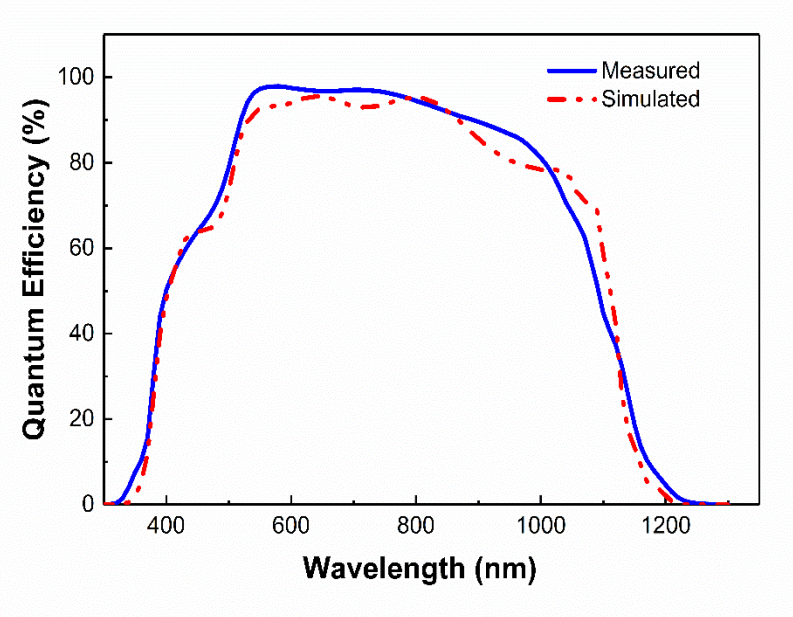

Figure 3.4:Comparison of the measured and optically simulated QE spectra

3.3.2 Thickness Optimization by Real Time Optimization via *in-situ* RTSE

A CIGS device without AR coating was loaded in the e-beam chamber. The reflectance of the device was then monitored *in-situ* and in real time during the deposition of the AR coating on the CIGS device (Figure 3.5). Figure 3.5 (a) shows real time measurements of the relative reflectance from the multi-layered CIGS solar cell during the deposition of MgF_2. The variations in reflectance can be observed for different wavelengths during the course of the deposition. One can see that a minimum is observed around 8 min for 300

nm, 9 min for 400 nm, and 10 min for 500 nm. In Figure 3.5 (b), another representation of the same data is shown, whereby the relative reflectance for wavelengths ranging from 300 nm to 1000 nm is reported for the same device for various thicknesses of the AR coating. One can see that as the thickness increases up to 110 nm, the average reflectance falls down. For larger thicknesses, the reflected irradiance increases at low wavelengths while decreasing at higher wavelengths. It is therefore difficult to optimize the thickness of the AR coating in real time and *in-situ* without a knowledge *a priori* of which wavelengths are the most crucial to increase the device current (as seen in Figure 3.3 for example). However, the main advantage of this technique is that it displays the real reflectance, taking into account surface roughness, which results in quite different behaviors. For example, in Figure 3.3, the 150 nm AR coating has sometimes higher values, sometimes lower values, of QE compared to the 110 nm for wavelengths between 500 nm and 1000 nm, while in Figure 3.5 (b) it is systematically lower for the 140 nm AR coating.

a)

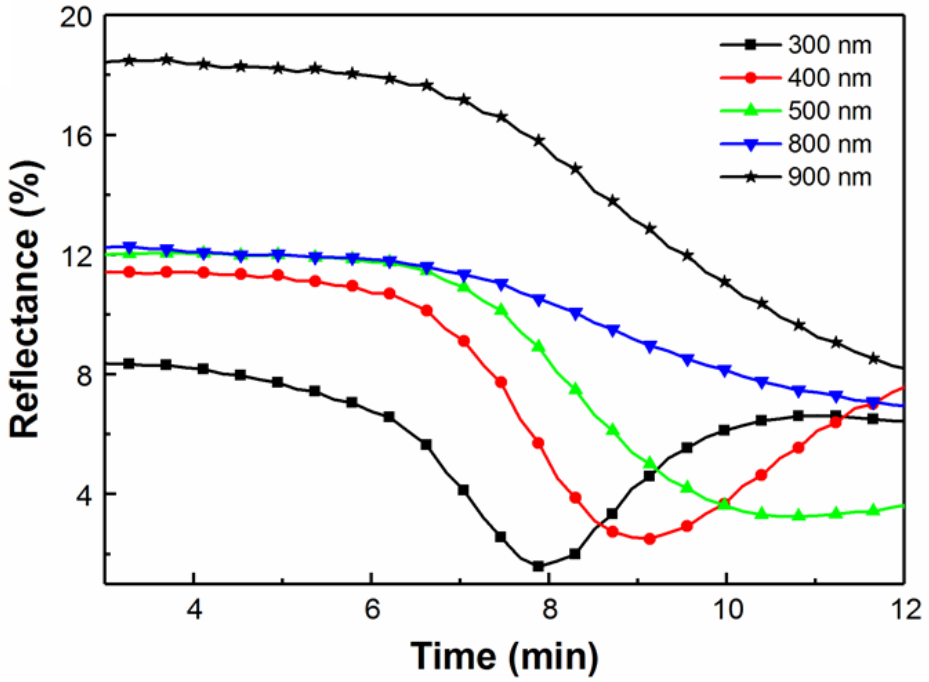

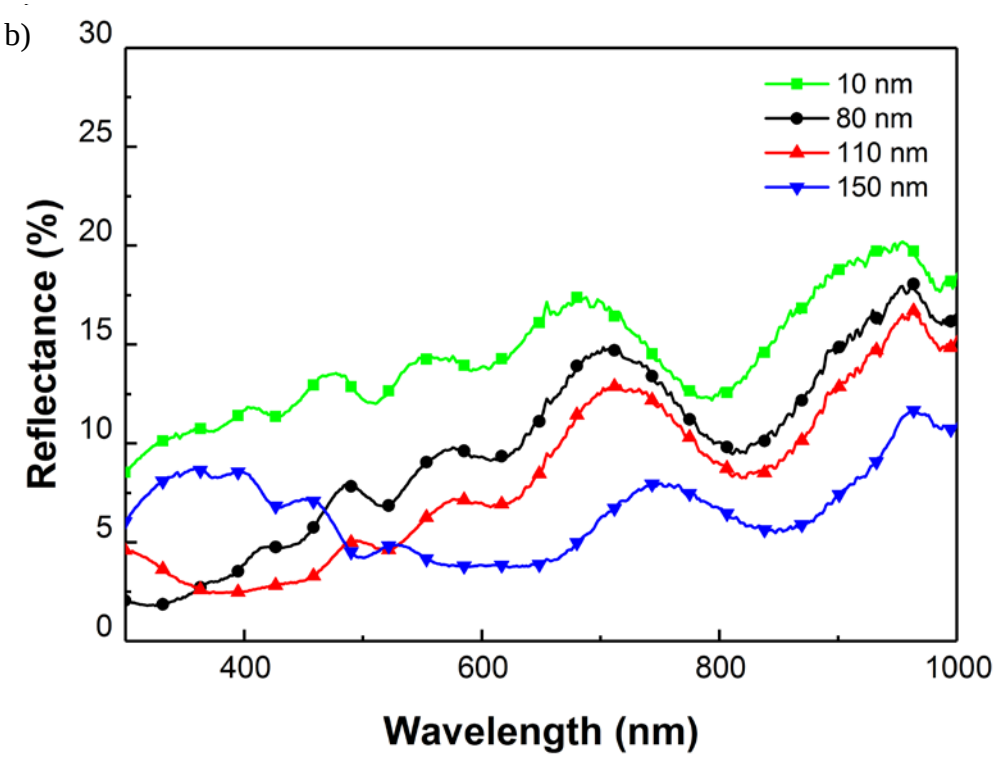

Figure 3. 5: (a) Real time variation of the relative reflectance during the course of deposition of the AR layer (t = 3 to 12 min); b) Real time variation of the relative reflectance of the CIGS structure with increased thickness of the AR layer.

Another optical model was developed incorporating the data obtained from RTSE and ex-situ ellipsometry to simulate the quantum efficiency of the CIGS device. The reflectance obtained during RTSE and the optical properties of each layer were incorporated to calculate the incomplete collection of photo-generated carriers in the CIGS device structure and is given by [39]

$$QE_{ext}(\lambda, V) = [1 - R(\lambda)][1 - A_{ZnO}(\lambda)] * [1 - A_{CdS}(\lambda)]QE_{int}(\lambda, V) \quad (3.2)$$

where R is the total reflection, A_{ZnO} is the absorption in the ZnO layer, A_{CdS} is the absorption in the CdS layer and QE_{int} is the internal quantum efficiency approximated by [39]

$$QE_{int}(\lambda, V) \approx 1 - \frac{\exp[-\alpha(\lambda)W(V)]}{\alpha L + 1} \tag{3.3}$$

where α is the absorption coefficient of CIGS, W is the space charge width in the CIGS layer, and L is the minority carrier diffusion length. This approximation assumes that all the carriers generated in the space charge region are collected without recombination loss. The optically simulated QE spectra is compared to the measured QE spectra for the CIGS solar cell device with AR coating in Figure 3.6, showing that the model provides a good fit.

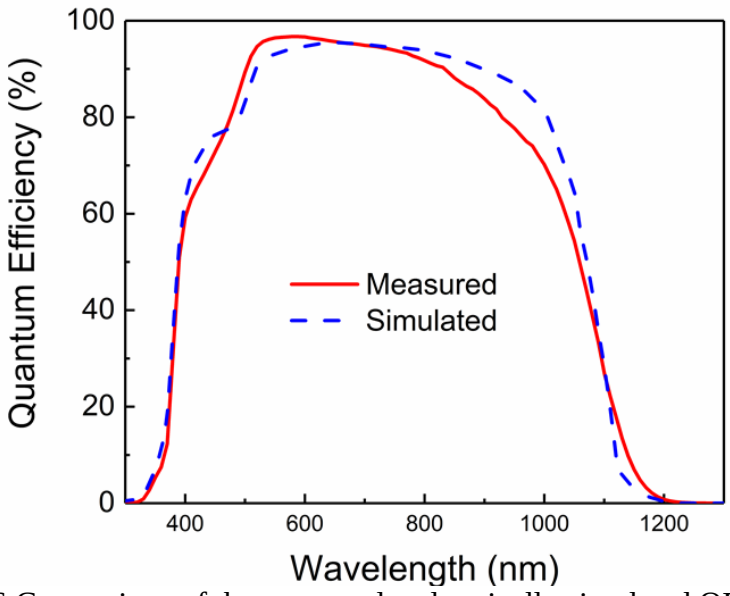

Figure 3. 6:Comparison of the measured and optically simulated QE spectra for CIGS solar cells

Optimized JV results

The thickness of the MgF_2 AR layer was decided upon using the in-situ reflectance measurement and simulation results. These results were incorporated into the fabrication of the AR coated CIGS device and a comparison of the effect of AR coating on the JV parameters of the recorded best cell is listed in Table I. The JV – QE results of the best cell with the new optimized coating is shown in Figure 3.7. The experimental results are in good correlation with the modeling results. Another sample was loaded in the chamber with the focus on minimizing relative reflectance at 500 nm. The results show enhanced current at all wavelengths as expected, without any noticeable change in open circuit voltage or fill factor.

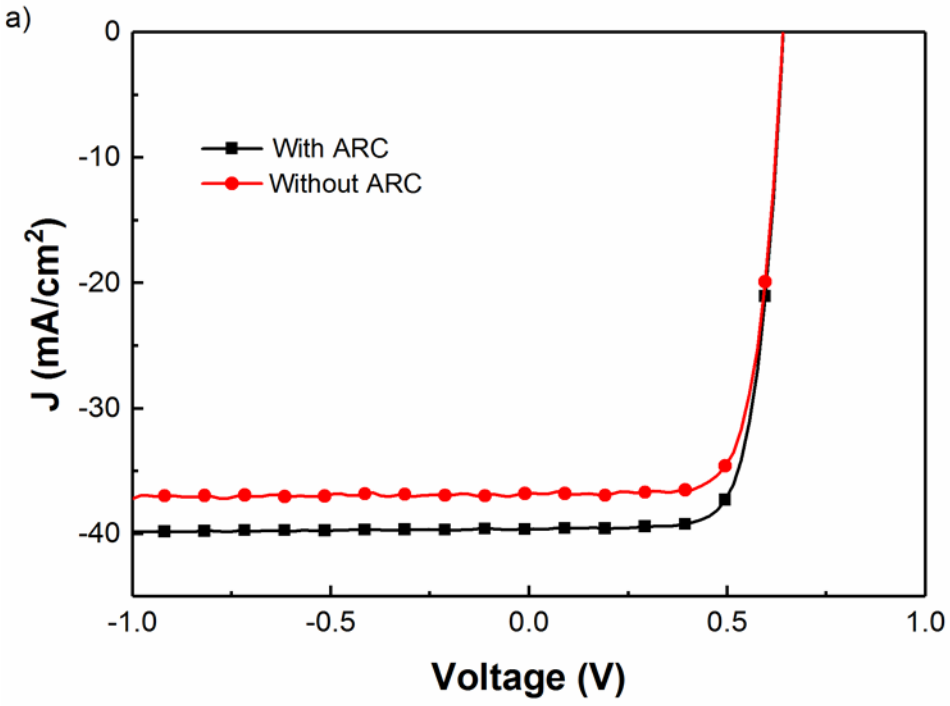

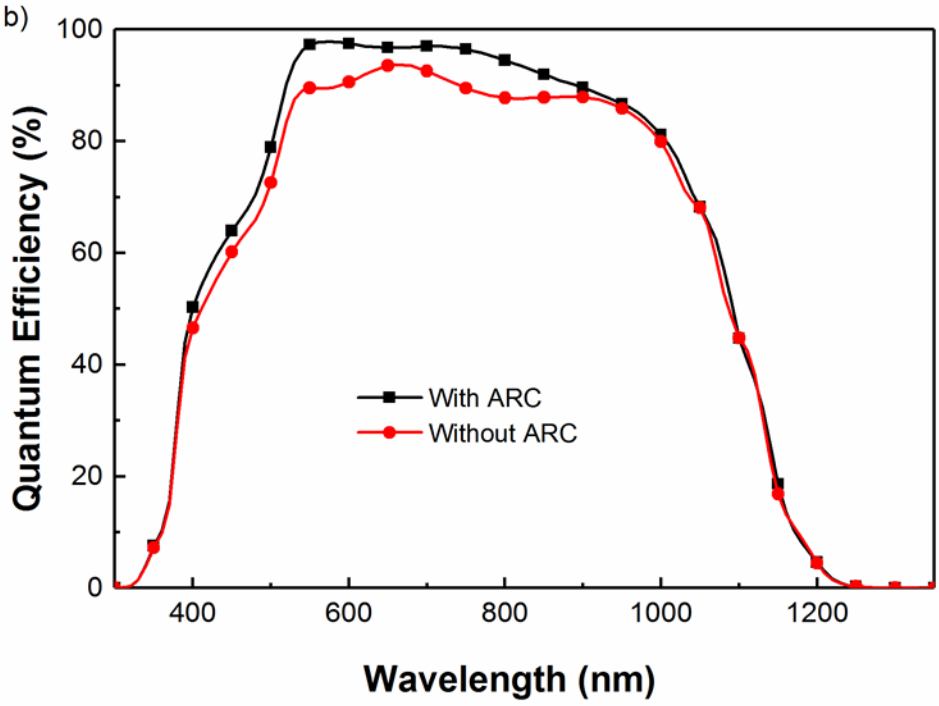

Figure 3. 7:Comparison of measured J-V curves and QE spectra obtained for CIGS solar cells with and without AR coating.

TABLE 3. 1 DEVICE PARAMETERS OF THE CIGS SOLAR CELL BEFORE AND AFTER DEPOSITING THE AR COATING

AR coating	**η (%)**	**Jsc (mA/cm^2)**	**Voc (V)**	**FF (%)**
Without AR	16.7	35.6	0.64	73.4
With MgF_2	17.6	37.5	0.64	73.1

3.3.3 Thickness Optimization by Transfer Matrix Theory Modeling and *in-situ* RTSE

In this method, both the TMT modeling using SE as well as the in-situ RTSE have been used to optimize the thickness of the AR coating. The TMT modeling associated with the

SE allows for accurate prediction of the thickness needed, while the *in-situ* RTSE allows for any experimental issue to be assessed and taken care of in real time. This thickness optimization tool is presented here for four examples: (a) variation in CIGS thickness, (b) variation in CdS thickness, (c) variation in AZO thickness, and (d) variation in MgF_2 deposition parameters.

a) Optimizing the AR layer as a function of the CIGS layer's thickness

It can be of interest to reduce the thickness of the CIGS layer for various reasons, notably (i) the scarcity of indium, which can have an economic impact on the CIGS solar module production; (ii) to increase the manufacturing throughput [40] .In this study, the thickness of the CIGS layer was varied (while all the other layers were kept constant) and the AR coating was optimized according to the change in the structure. The TMT modeling was used to predict the short circuit current density, J_{SC}, and quantum efficiency of the CIGS device with various thicknesses of the absorber layer (Figure 3.8).

As one can see, the optimum thickness of the MgF_2 layer is predicted to change from 111 nm for a 0.5 μm CIGS to 117 nm for a 2.5 μm CIGS. Note that the loss of current from 2 μm to 0.5 μm is mostly due to incomplete absorption in the CIGS layer, which a single layer AR coating cannot compensate for [38]. It is important to note that this modeling is purely optical and does not take into account potential problems due to back surface recombination or short-circuit, specifically for the ultra-thin devices.

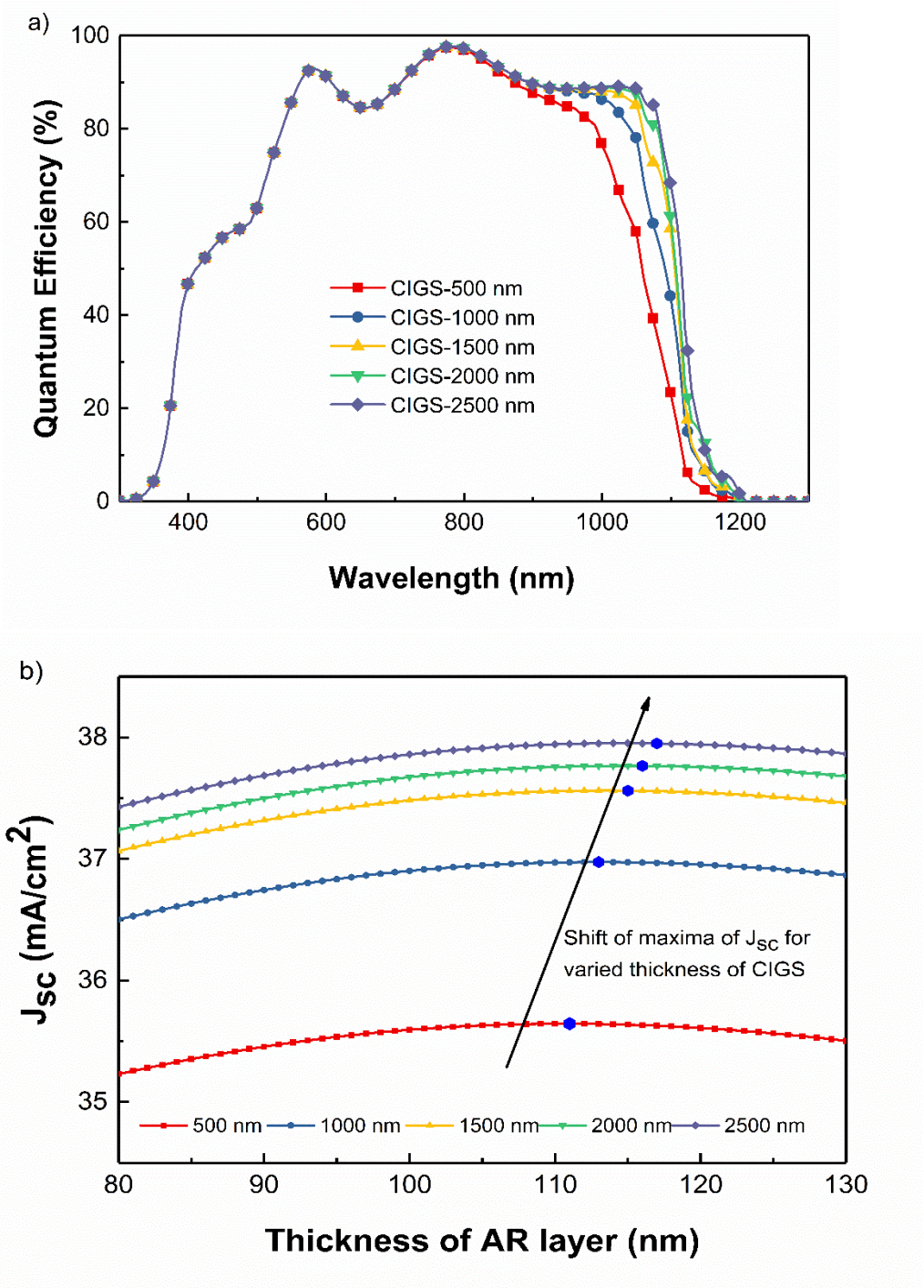

Figure 3. 8:a) Simulated variation of QE with varied thickness of CIGS layer and a fixed value of MgF2 (111 nm), b) Simulated JSC for a CIGS device as a function of MgF2 thickness, for varied thickness of CIGS layer.

Once the optical modeling was completed, we fabricated three cells with CIGS thickness of 500, 1500 and 2500 nm, respectively. The samples were then loaded in the e-beam chamber after full characterization. The relative reflectance of the device was monitored using RTSE during the deposition of the MgF_2 AR layer to observe the variation of the reflectance in real time (Figure 3.9).

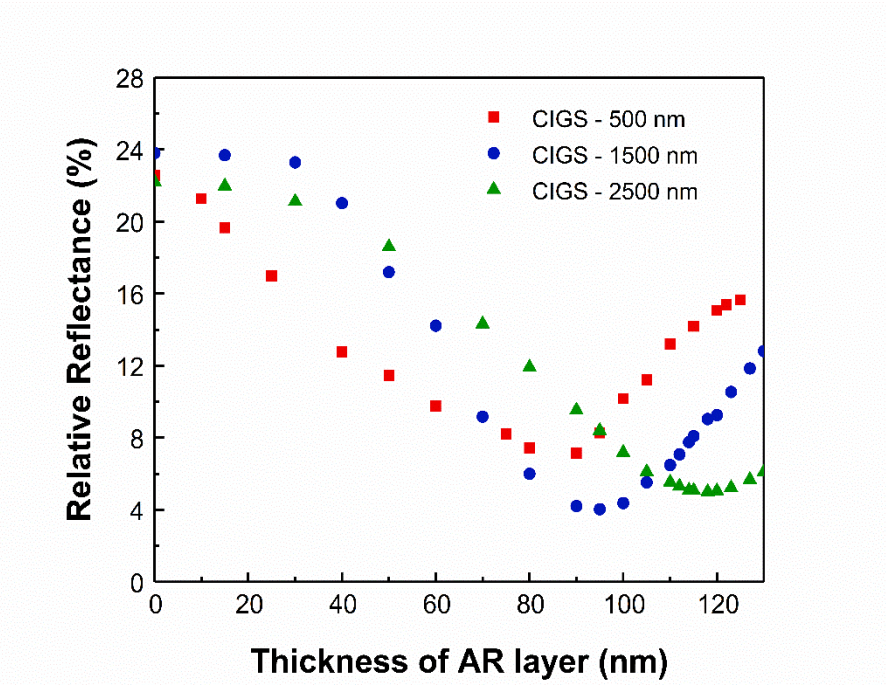

Figure 3. 9: Real time relative reflectance for CIGS devices with different layers of CIGS thickness.

The deposition of the MgF_2 AR layer was not stopped intentionally at the ideal thickness to show clearly where that thickness is. In other runs, this can obviously be modified to stop at the desired ideal thickness, based on the TMT modeling prediction and clear inflection point of the *in-situ* data. The effect of the CIGS thickness can be seen, whereby the reflectance minimum does not occur at the same MgF_2 thickness for all samples. In this case, the ideal thickness was 88 nm for the 500 nm CIGS, 95 nm for the 1500 nm CIGS,

while it was 117 nm for the 2500 nm CIGS. Note that this value is slightly different than the one obtained from simulation, probably due to the importance of the surface roughness, especially for the ultra-thin film. The capacity to optimize the thickness of AR layer was further tested on CIGS devices with absorber thickness of 1500 nm (Figure 3.10). Here, several samples from the same deposition were either not coated, coated with a standard AR thickness (105 nm), or had an optimized AR layer deposited (in this specific case, 97 nm). One can see from the J-V curves that there is almost 1mA/cm^2 increase in the devices with the optimized AR layer, when compared to having the conventional AR layer with little change for the other parameters.

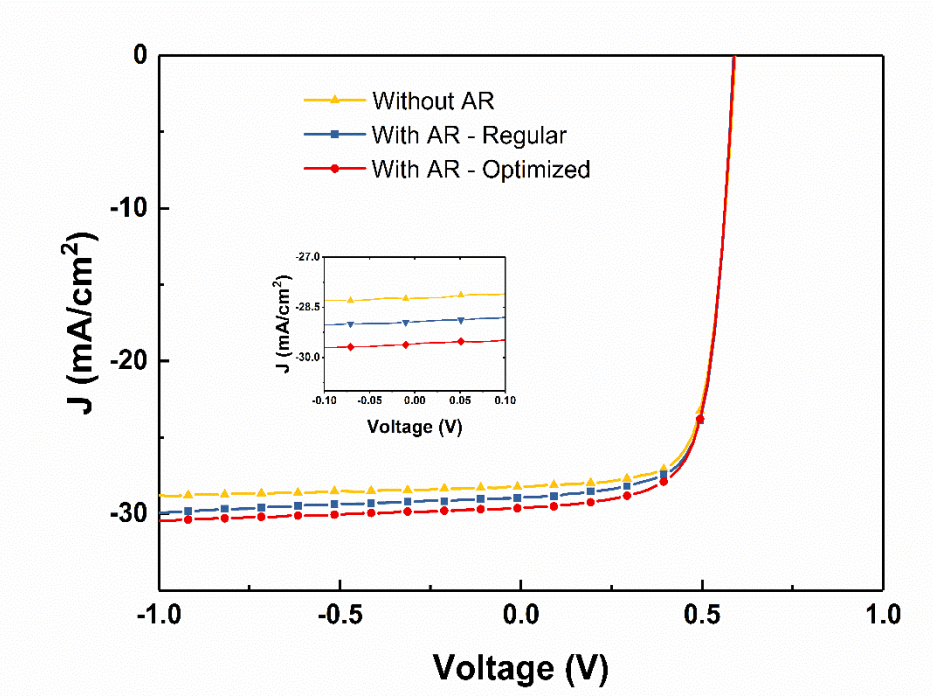

Figure 3. 10: J-V curves for CIGS solar cells with absorber of 1500 nm and various AR coating configurations

b) Optimizing the AR layer as a function of the CdS layer's thickness

Light absorption in the CdS buffer layer is known to take a significant share in the total photocurrent loss of the heterojunction structure. The charge carriers photogenerated in the

buffer layer are only partly collected and this reduces the spectral response of the solar cell, notably in the blue region of the solar spectrum. Figure 3.11 (a) shows the simulated QE of solar cells with varied thickness of CdS layer. The blue response of the quantum efficiencies decreases with growing CdS thickness, due to the increased absorption in the CdS layer. Even though the thinning down of the CdS layer seems to be beneficial, there is a limit where the interface between CIGS and CdS degrades, at which point electronic losses will become important. Thus, it has to be a balance between the optical gain and the electronic losses. Previous studies had shown that they compensate each other for CdS thickness of about 40 nm[41]. However, with recent key innovation involving alkali post deposition treatment of the CIGS layer, it is now possible to reduce the minimal thickness of the CdS buffer layer even further and reach higher efficiency.

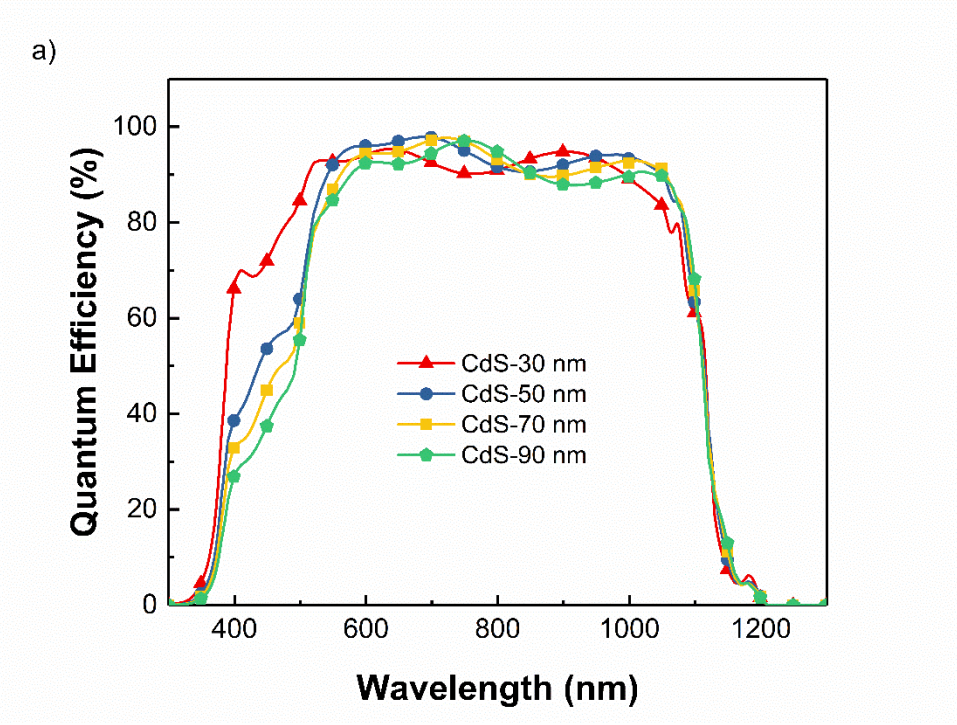

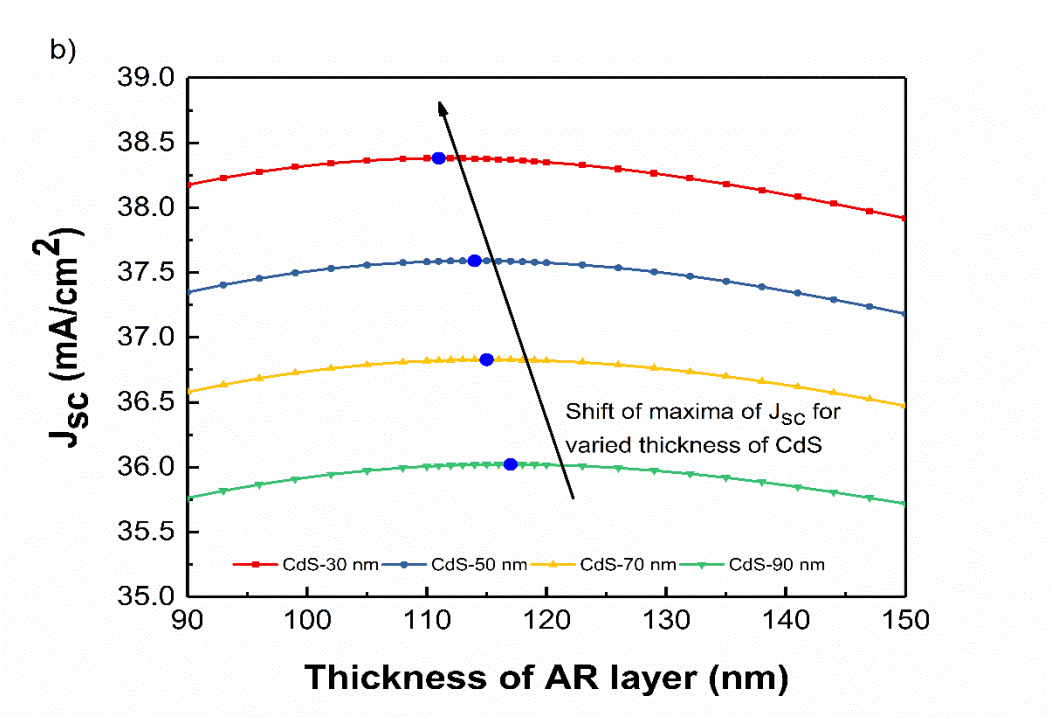

Figure 3. 11:a) Simulated variation of QE with varied thickness of CdS layer for a fixed value of MgF_2 (112 nm), and b) Simulated JSC as a function of MgF_2 thickness for various thickness of CdS layer.

With the variation in the thickness of CdS layer, it is equally important to optimize the AR layer to ensure full benefit of these process modifications. Using TMT modeling and SE measurements, we therefore simulated the variation of the J_{SC} maximum for various thicknesses of both CdS and MgF_2 (Figure 3.11(b)). As one can see, the ideal MgF_2 thickness range from 117 nm for CdS of 100 nm, down to 111 nm for CdS of 20 nm for this specific device. Following the optical model, two samples were fabricated simultaneously and the thickness of the CdS layer was reduced from 50 nm for a regular device to 30 nm. The samples were then loaded in the e-beam chamber after full characterization. The relative reflectance of the device was closely monitored using RTSE

during the deposition of the MgF_2 AR layer. Here too, for this specific example, we did not interrupt the deposition of the MgF_2 AR layer at the ideal thickness, to demonstrate the capacity to observe its effect in real time. As one can see Figure 3.12, the reflectance reached a minimum for sample with regular CdS thickness for an AR layer of 118 nm, whereas for the device with reduced CdS thickness, the reflectance reached the minimum for 110 nm, as our model predicted. The average reflectance for the device varied therefore with the CdS thickness, but with the deposition of an optimized thickness of AR layer, it is possible to reduce the reflectance to obtain the highest efficiency devices in all cases. For a CIGS device having a thin CdS layer (30 nm), the simulations account to depositing an AR layer for 110 nm. The effect of having deposited the optimized AR layer on the device with thin CdS layer is demonstrated in Figure 3.12. There is a clear enhancement in the Jsc for the new optimized layer when compared to depositing the AR layer of standard thickness of 118 nm.

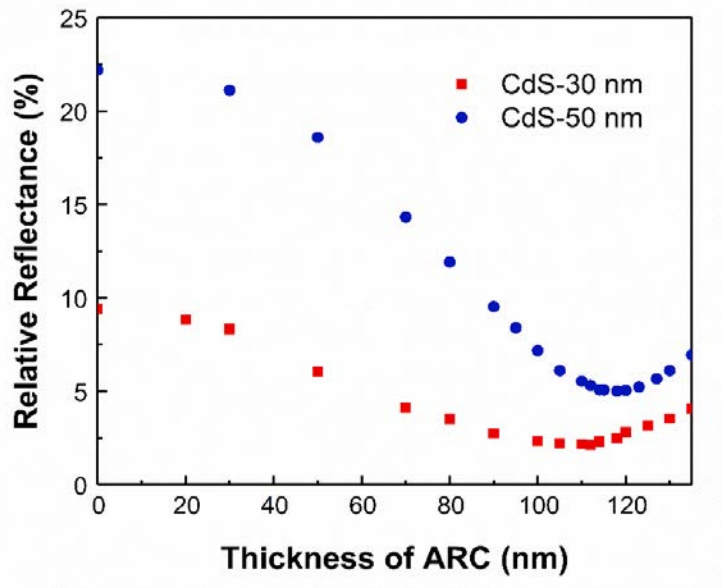

Figure 3. 12:Real time relative reflectance for CIGS devices with different layers of CdS thickness

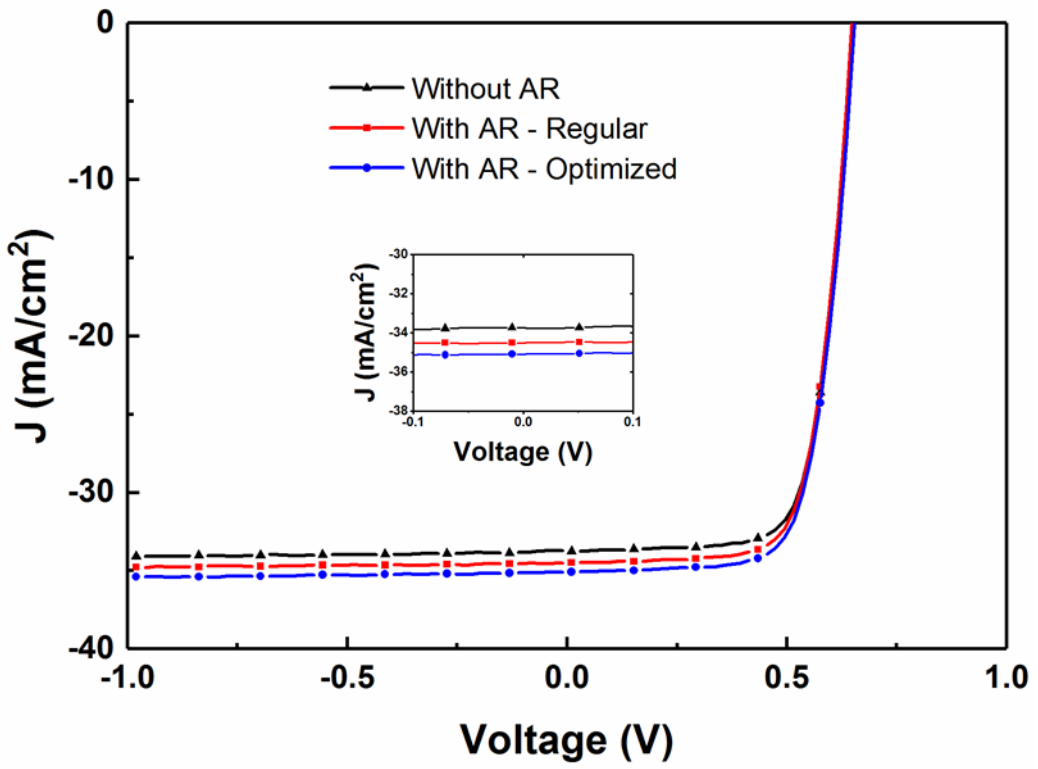

Figure 3. 13: J-V curves for CIGS solar cells with CdS layer of 30 nm and various AR coating configurations

c) Optimizing the AR layer as a function of the AZO layer's thickness

Similarly, to the CIGS and CdS thicknesses, the AZO layer thickness is quite often different from one group to another (without mentioning the use of alternate material such as ITO). In this section, the thickness of the AZO layer is therefore varied and the AR coating optimized according to the change in the structure. The optical model was used to predict the QE and short circuit current density of the CIGS device with the reduced thickness of the window layer (Figure 3.14 (a)). It is clearly evident from Figure 3.14(b) that the short-circuit current density, J_{SC}, is influenced by the reduction of the thickness of the TCO layer. There is an improved collection efficiency at longer wavelength region of the QE spectra for thinner layer, which can be attributed to the increase in optical transmission allowing more light to be absorbed by the CIGS layer [42]. However,

similarly to CdS, one has to take into account the potential electronic losses, coming here from reduced current collection. As one can see, the ideal MgF_2 thickness range from 110 nm for AZO of 300 nm, up to 115 nm for AZO of 150 nm for this specific device.

Following this modeling, two samples were fabricated simultaneously and the thickness of the TCO layer was reduced from 300 nm for a regular device to 150 nm. The samples were then loaded in the e-beam chamber after full characterization. The relative reflectance of the device was closely monitored using RTSE during the deposition of the MgF_2 AR layer. As one can see in Figure 3.15, the reflectance reached a minimum for the sample with regular TCO thickness for an AR layer of 110 nm, whereas for the device with reduced AZO thickness, the reflectance reached the minima for 120 nm, as our model predicted. The average reflectance for the device varied therefore with the AZO thickness, but with the deposition of an optimized thickness of AR layer, it is possible to reduce the reflectance to obtain the highest efficiency devices in all cases.

Figure 3.16 compares the effect of optimizing the thickness of the AR layer for a CIGS device with a thinner AZO layer of thickness 150 nm. The increase in the Jsc clearly substantiates the need of depositing a thicker AR layer of 120 nm when compared to the standard thickness of 105 nm as optimized for a regular CIGS device, with an increase of current of 2-3%.

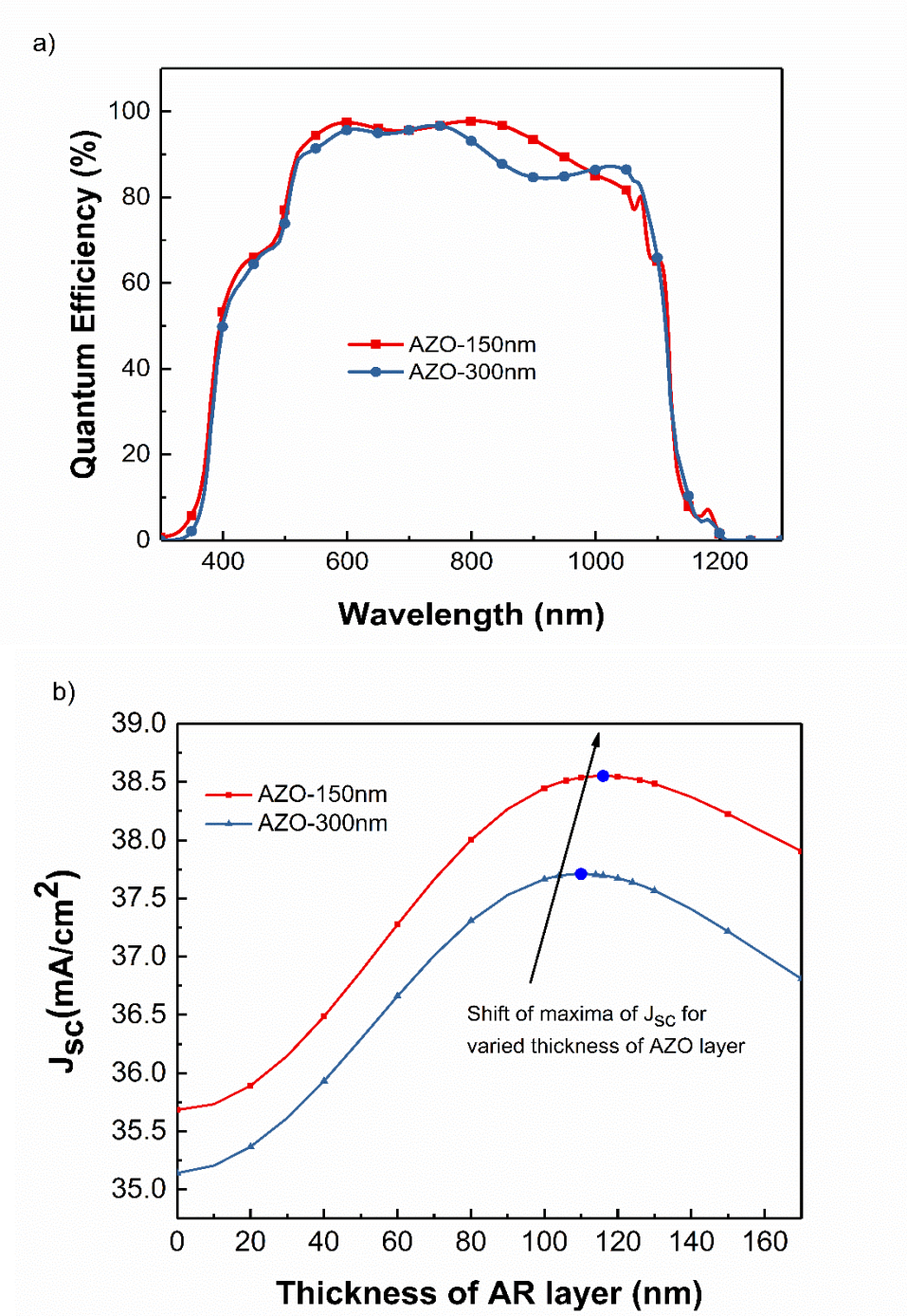

Figure 3. 14:a) Simulated variation of QE with varied thickness of AZO layer for a fixed value of MgF_2 (110 nm), and b) Simulated J_{SC} as a function of MgF_2 thickness for various thickness of AZO layer.

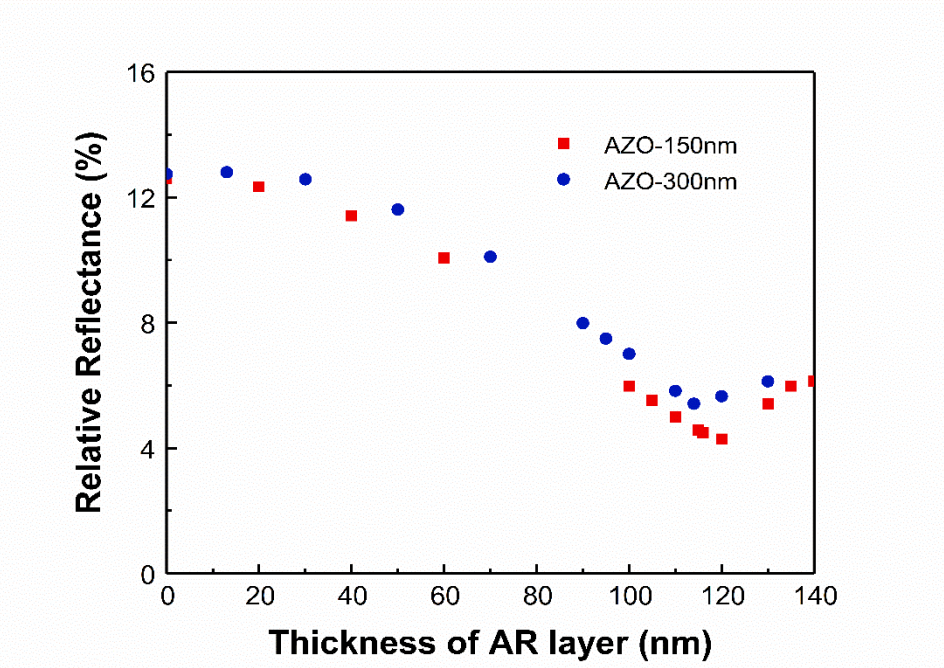

Figure 3. 15: Real time relative reflectance for CIGS devices with different layers of TCO thickness.

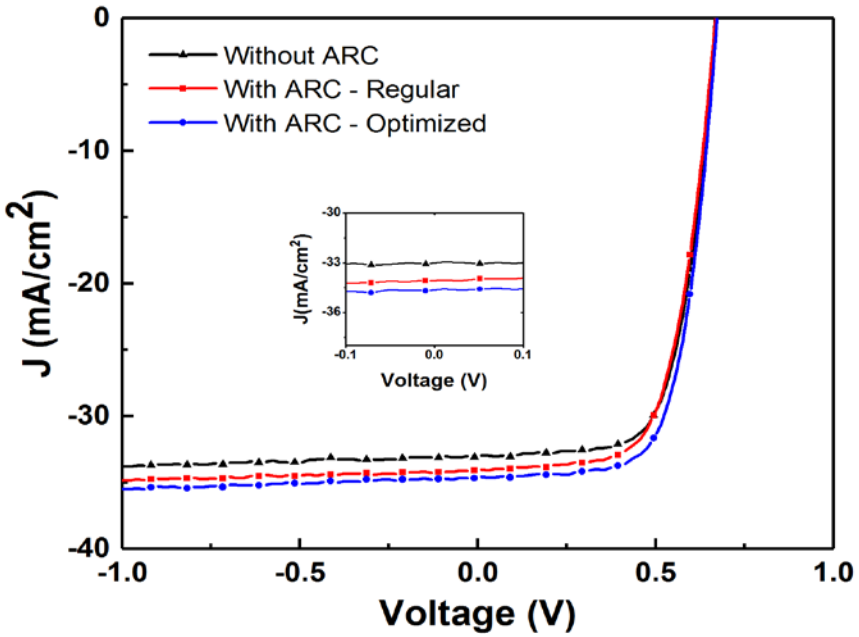

Figure 3. 16: Comparison of effect of optimized ARC on measured J-V curves CIGS solar cells having a thin AZO layer of 150 nm.

d) Optimizing the AR layer Deposited at Different Substrate Temperatures

It is equally important to understand the optical and structural quality of the AR layer in order to obtain maximum efficiency. The process variables for the deposition of MgF_2 layer was varied and the growth conditions were studied using RTSE to clarify and derive the optimum process conditions. The substrate temperature (T_{SS}) was changed from room temperature (RT) to 100°C to monitor the effect on the thin film. The refractive index of the film was extracted from the data obtained during RTSE. One can observe (Figure 3.17) that the refractive index decreases from RT to 50°C, then increases for all wavelengths from 50°C to 100°C. This is explained by the fact that the films at RT are densely packed and amorphous, while the film at 50°C are nanocrystalline but less dense, which yield a lower refractive index for the latter[43]. After that, the increase in temperature leads to nanocrystalline films with larger grains and higher packing density, thanks to the faster molecular motions occurring at a higher temperature [44, 45], and therefore has higher refractive index.

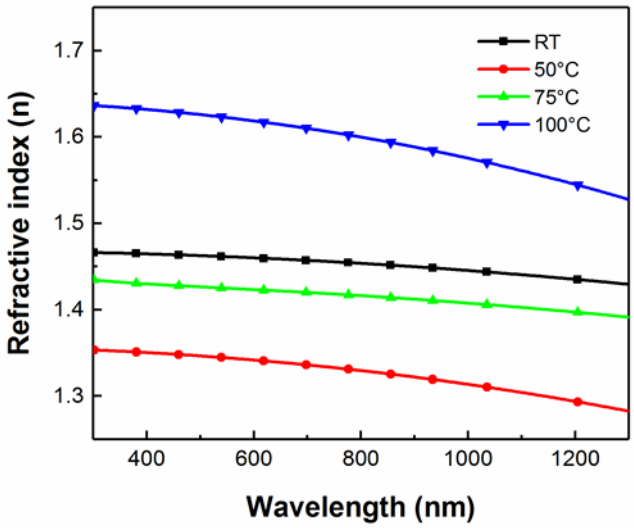

Figure 3. 17:Measured refractive index as a function of wavelength for MgF_2 films deposited for different T_{SS}, as extracted using RTSE

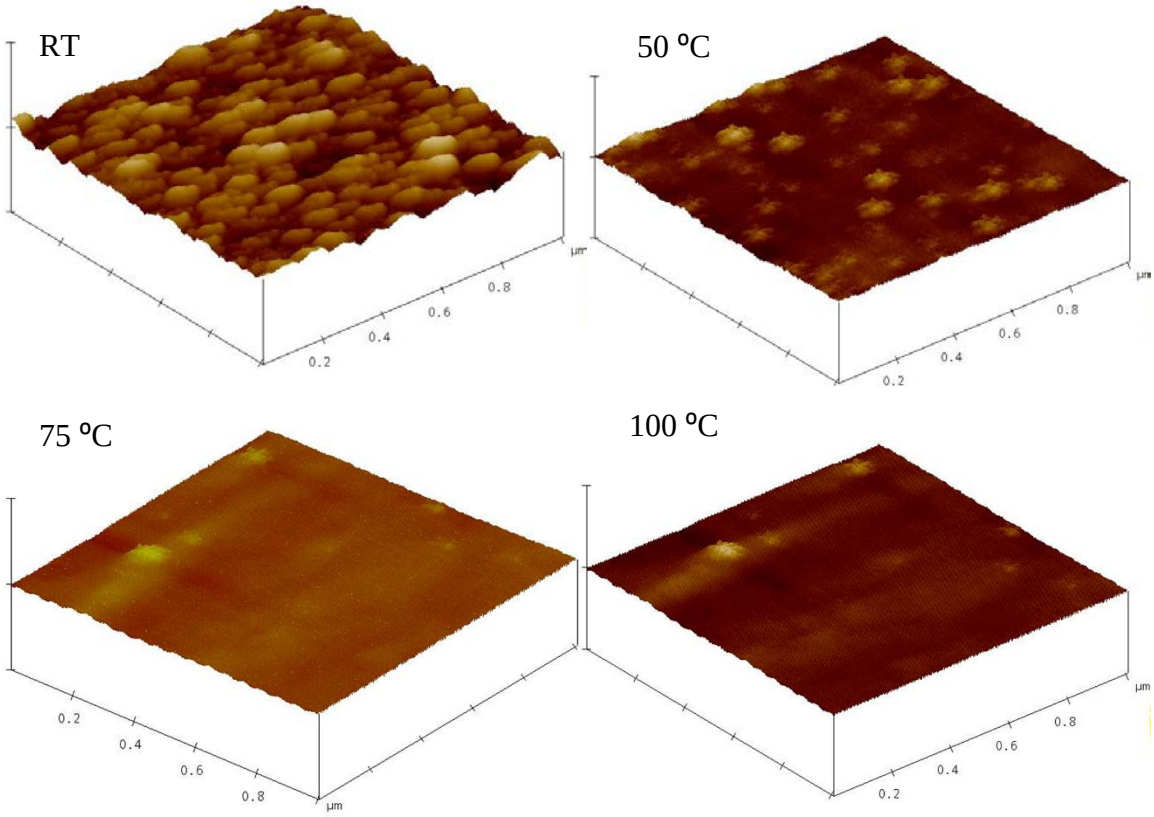

Figure 3. 18:AFM images of surface topography of MgF_2 layer deposited at different room temperatures.

Figure 3.18 compares the surface topography of the films deposited at different substrate temperatures as obtained from AFM images. The surface roughness of the films decreases considerably from 13 nm (RT) to 3nm (100 ^{0}C). The transmission and reflection intensity of the films differ with the change in temperature. Effect of high temperature on the MgF_2 layer on the reflection and transmission intensity of the layer is shown in Figure 3.19.

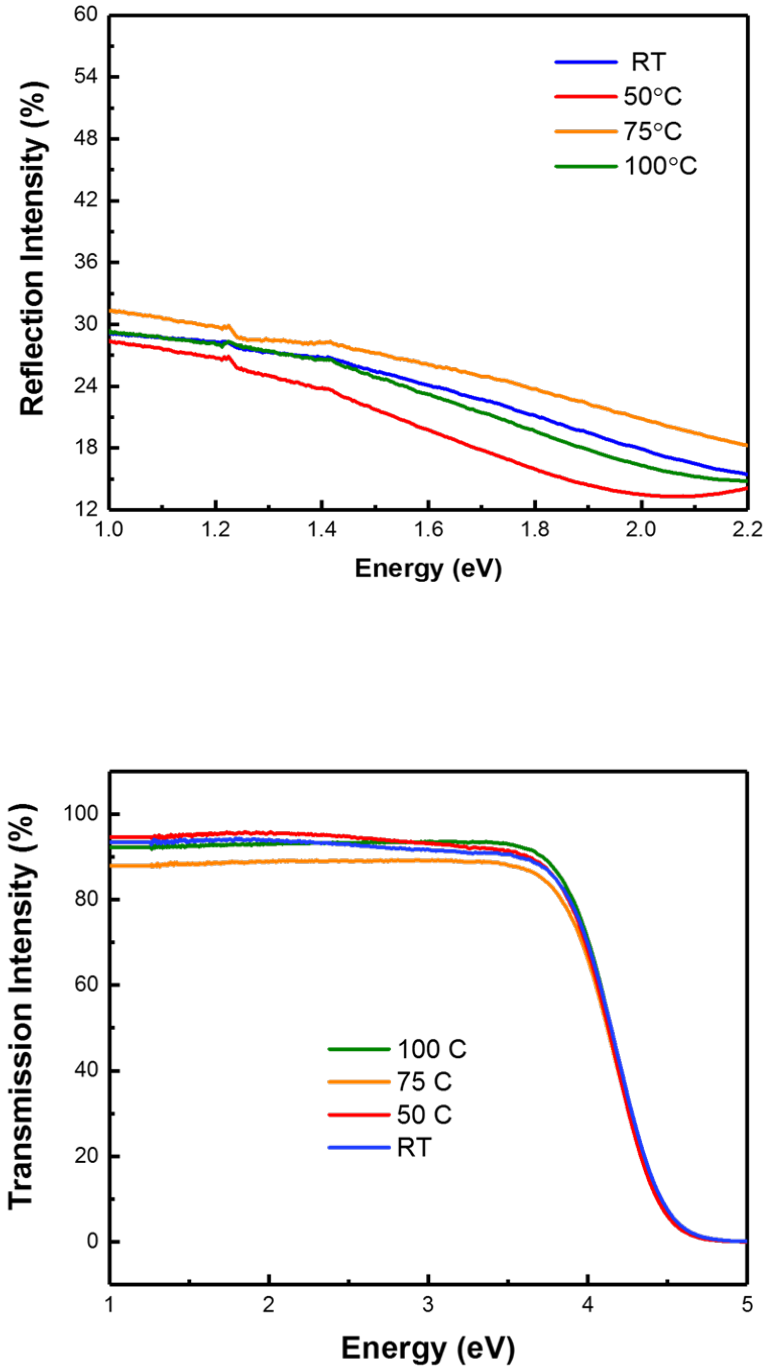

Figure 3. 19: Transmission and Reflection Intensity of MgF_2 layers deposited at different substrate temperatures

The TMT optical modeling was applied to predict the QE spectra and maximum obtainable J_{SC} for CIGS solar cells with AR layer deposited at different T_{SS} (Figure 3.20). The maximum value of J_{SC} can be observed for the cells with an AR layer deposited at 50°C with a thickness of 118 nm, for that specific structure.

.

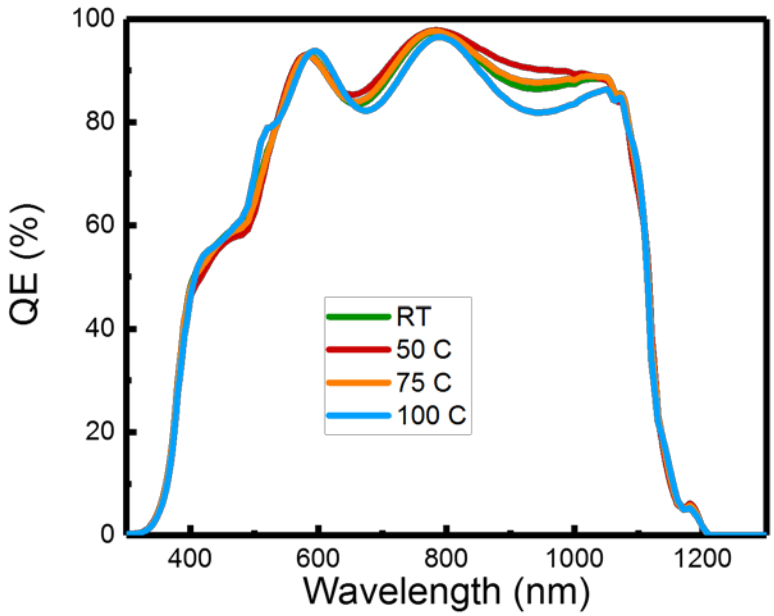

Figure 3.20:Simulated QE spectra CIGS devices with varied AR layer deposited at different T_{SS}.

Simulation results were used to guide the fabrication of AR coated CIGS devices with various MgF_2 T_{SS}. However, one has to keep in mind the effect of T_{SS} on the rest of the structure. Samples were loaded in the e-beam chamber after full characterization and a MgF_2 layer was deposited at different T_{SS}. The relative reflectance was measured in real time, but the deposition was stopped at the ideal thickness for these runs. After the run, grids of Ni/Al/Ni were deposited on the structure and the solar cells performance was measured.

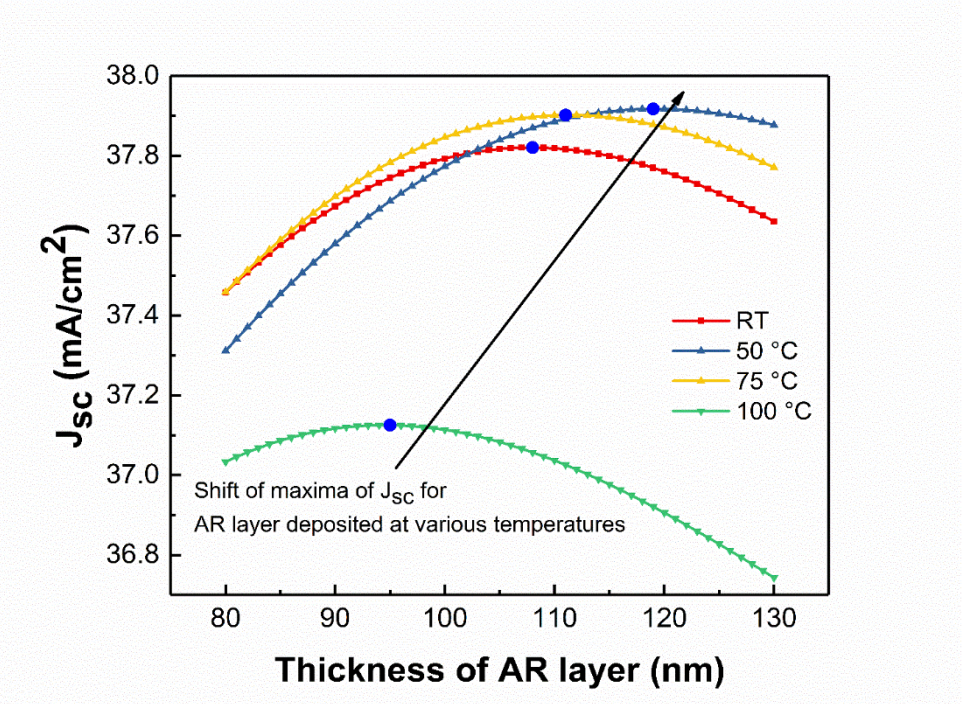

Figure 3.21: Simulation of the variation of J_{SC} for CIGS devices with varied thickness of MgF_2 layer deposited at different T_{SS}.

The average relative change (in percentage) in J-V parameters of the solar cell for AR coating deposited at different T_{SS} are reported in Table II. This average was done for > 100 cells. The experimental results are in good correlation with the modeling results. The results substantiate an enhanced performance of the devices with AR coating applied at 50°C. There is an increase in the J_{SC} by 10%, while AR coating deposited at RT only enhanced it by 5%. Even though higher J_{SC} values are reported for AR coating deposited at 75 °C and 100° C, the negative impact on V_{oc} and FF reduces the overall efficiency of the cell. The higher T_{SS} probably deteriorates the junction quality. It is interesting that the TMT modeling for the 100° C deposition predicted a lower current than for the other temperature, while it is quite similar experimentally and it could be explained due to the change in the optical properties of the film. Here again, the combination of predictive

modeling with *in-situ* real time measurement proves to be very useful in obtaining the best results.

TABLE 3. 2 AVERAGE RELATIVE CHANGE (IN %) IN J-V PARAMETERS OF SOLAR CELL FOR AR COATING DEPOSITED AT DIFFERENT SUBSTRATE TEMPERATURE

T_{SS} for AR coating	**η (%)**	**Jsc (mA/cm^2)**	**Voc (V)**	**FF (%)**
RT	+4	+4	0	0
50°C	+10	+9	0	+1
75°C	- 5	+15	- 2	- 15
100°C	- 11	+10	- 4	- 15

CHAPTER 4
MULTI-LAYER ANTI-REFLECTIVE COATINGS ON ULTRATHIN $Cu(In,Ga)Se_2$ SOLAR CELLS

4.1 Introduction and Motivation

The recent developments in $Cu(In,Ga)Se_2$ (CIGS) technology makes it a promising technology with an immense potential for development. However, the scarcity and high price of indium and gallium can potentially hinder it from competing with other solar cell technologies. The thickness of the absorber layer can be reduced to reduce the production cost [46] , but would lead to a decrease in short circuit current thereby reducing the overall efficiency. Figure 4.1 illustrates the simulated loss of J_{sc} with the reduction in thickness of absorber layers. However, the thickness of the absorber layer should be large enough to absorb as much as 99% of the incident light. The attenuation length was calculated for the CIGS absorber layer from the experimentally obtained optical constants. Figure 4.2 shows that the reduction of absorber layer thickness to 1μm leads to less than 1/e attenuation for the wavelengths above 1040nm. The minority carrier diffusion length should be several times the material thickness to ensure complete collection of the photo-carriers to have greater efficiency. As the thickness of the CIGS is reduced, a greater fraction of carriers is excited near the back contact and are lost. The light trapping capacity of the cell needs to be increased significantly along with an improvement in the back contact is significant to collect all the photo-generated carriers to impact the current and to increase the overall efficiency. The multilayer structure needs to be redesigned so that the optical field is enhanced at the top and suppressed at the back contact.

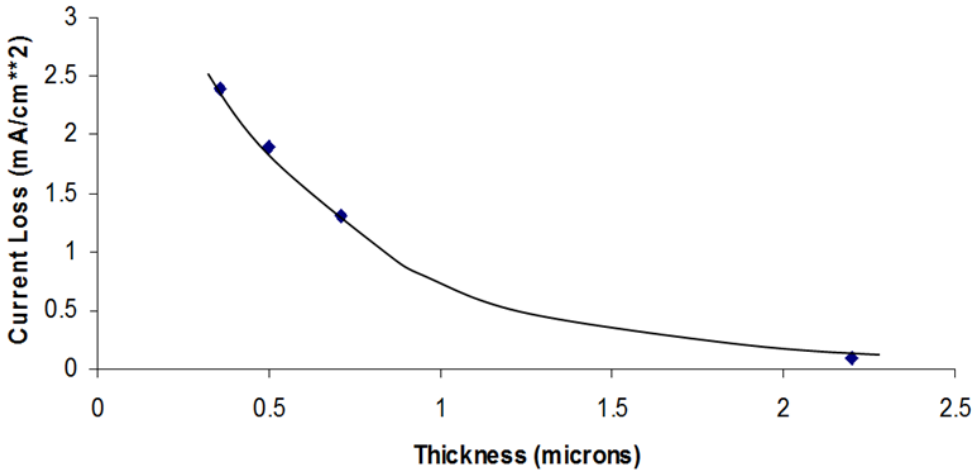

Figure 4.1:Loss of Jsc with the reduction in thickness of absorber layers

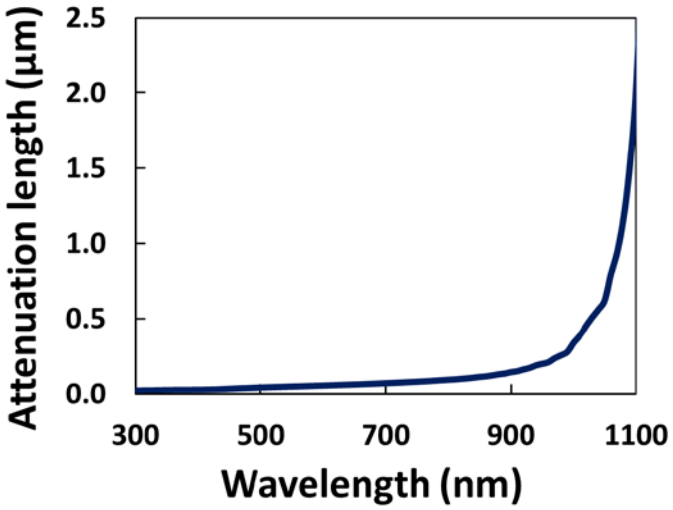

Figure 4. 2: Measured 1/e attenuation length as a function of CIGS absorber layer.

Anti-reflective (AR) coatings on the solar cells are very beneficial to minimize the reflection losses and thus increase the power conversion efficiency. The thickness and refractive index of the materials are chosen such that, when the light is incident on the cell, it undergoes destructive inference with the reflected light. However, the reflection losses are minimal near the wavelength and angle of incidence at optimization, and vary

drastically for other wavelengths and angle of incidences. When the thickness of the CIGS layer is reduced, the quantum efficiency (QE) curve drops for higher wavelength as the absorption reduces. Figure 4.3 shows the simulated QE curve for the variation in thickness of the absorber layer.

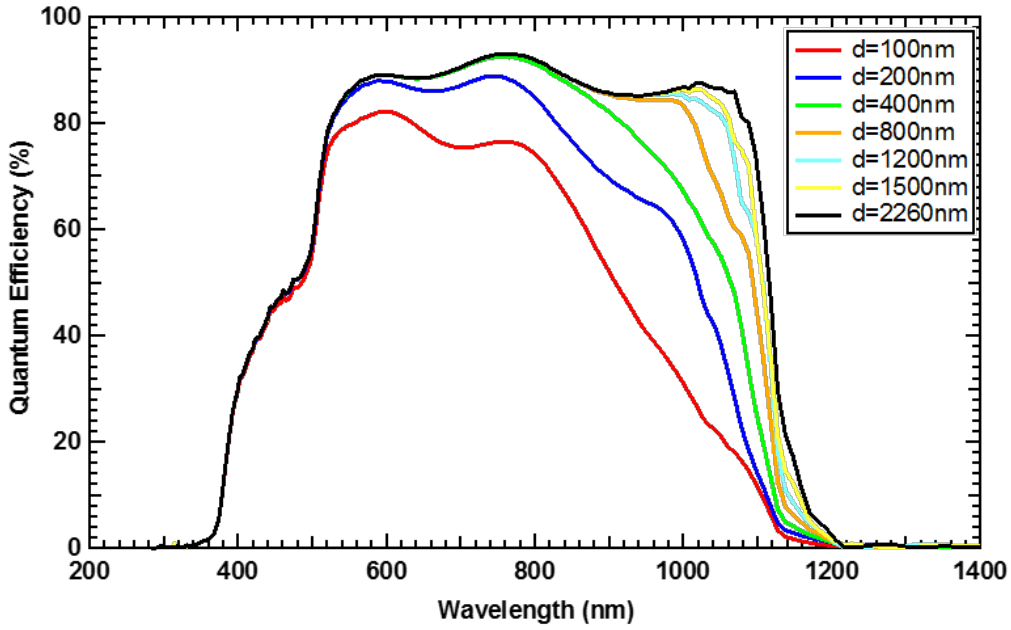

Figure 4. 3: Predicted QE for solar cells with CIGS absorber layers of different thicknesses.

A single layer AR coating is only designed to reduce reflection at a single wavelength and is not very effective over the entire spectral range for a thin CIGS device. Thus it is very important to obtain an enhanced light trap in the red and near infrared region. Multi-layer AR coatings can indeed be used to obtain at least five passes in the internal reflection from the bottom surface of the cell.

a)

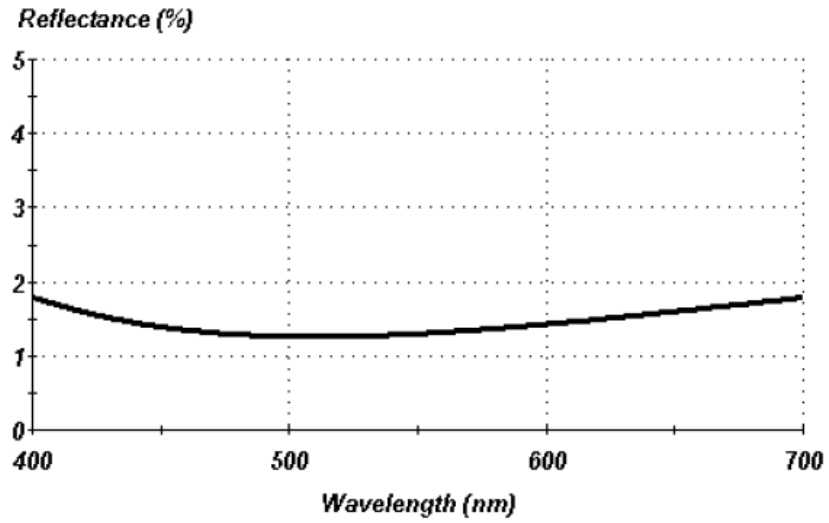

b)

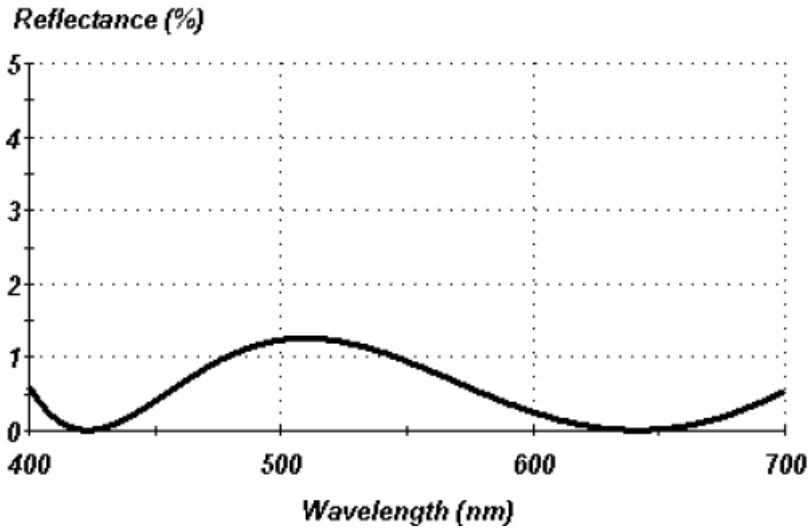

Figure 4. 4: (a) The reflectance of single layer AR coating (V coat), (b) The reflectance of double layer AR coating (W coat)[47]

Figure 4.4 compares the reflectance of a single layer AR coating with the reflectance of a substrate having double layer AR coating. The reflectance curve for a single AR coating curve is often called a V coat and the one with a double AR coating is called a W- coat owing to the shape of its characteristic curve. It's clearly visible that the W coat curve has minimum reflection points at different wavelengths and the average reflectance is comparatively reduced [48, 49].

4.2 Materials and Data Analysis

A wide variety of materials available for anti-reflection coatings, including MgF_2 and TiO_2, HfO_2, and ZrO_2 were deposited in a Kurt J. Lesker PVD 75 electron-beam evaporator. A base pressure lower than 10^{-6} Torr was obtained by a turbo-molecular pump prior to film depositions and the substrate holder was rotated at 15 rpm to ensure uniform deposition. Well-characterized Si wafer substrates were used, and the film/substrate was measured using ex-situ variable angle of incidence SE. Analysis of the SE data yields the optical properties and film microstructure parameters. The deduced optical properties are shown in Figure 4.5, and these were used in the optical modeling of the previous paragraph. The optical properties of Al_2O_3 used in the modeling were obtained from the literature. Unfortunately, the choices available for the low index materials of AR coatings are limited, as most fluoride materials show degradation over time when exposed to air.

The ellipsometry data was analyzed using an optical model incorporating a bulk layer and surface roughness layer thickness. The dielectric functions of each layer were extracted by point by point fitting correlated with the thickness of the layer. A model including the Cauchy dispersion equation and Urbach-like absorption onset was used to extract the refractive index and the extinction coefficient. The index of refraction for transparent films in the visible spectral range is often described by a Cauchy expression. A Cauchy expression can be used to define the index of refraction of non-absorbing films, or weakly absorbing dielectric and semiconductor films below the fundamental bandgap. The Cauchy model as described in the CompleteEASE software consists of a three-term expression that describes the index of refraction, as follows:

$$n(\lambda) = A + \frac{B}{\lambda^2} + \frac{C}{\lambda^4}$$

The parameter *A* describes the wavelength-independent amplitude of the index of refraction, and the parameters *B* and *C* describe the dispersion of the index versus wavelength. Thus, the parameters *A*, *B*, and *C* are variable fitting parameters that describe the wavelength dependence of the index of refraction. In addition to the Cauchy parameters *A*, *B*, and *C*, three additional parameters are used to describe an Urbach-like absorption tail as follows:

$$k = k_0 e^{D(\lambda - F)}$$

Here, *k*0 and *D* are parameters used for fitting the extinction coefficient whereas *F* is a fixed parameter set to the shortest wavelength of the measured ellipsometry spectra. It should be noted that for a true Urbach tail, the absorption coefficient increases exponentially with photon energy, as compared to the behavior of Eq. 2.19 in which the extinction coefficient decreases exponentially from the shortest wavelength of the measured spectra. The thin films of MgF2, HfO2, ZrO2, TiO2, SiO2, and Al2O3 deposited in this study were analyzed using ex-situ spectroscopic ellipsometry. The optical model incorporates the bulk layer thickness and surface roughness layer thickness as wavelength-independent free parameters. The surface roughness layer is assumed to consist of 50 vol.% bulk layer material and 50 vol.% voids. The deduced film thicknesses are summarized in Table 4.1 and the parameterized index of refraction and extinction coefficient spectra are shown in Figure. The Cauchy and Urbach-like parameters that define these spectra are summarized in Table 4.2.

TABLE 4. 1 BULK AND SURFACE ROUGHNESS LAYER THICKNESSES AS DETERMINED BY SPECTROSCOPIC ELLIPSOMETRY

Layer	Bulk thickness (nm)	Surface roughness (nm)
MgF_2	122.64 ± 0.25	0.90 ± 0.17
HfO_2	146.65 ± 0.29	2.44 ± 0.23
ZrO_2	155.74 ± 0.27	2.77 ± 0.28
TiO_2	152.34 ± 0.19	1.20 ± 0.15

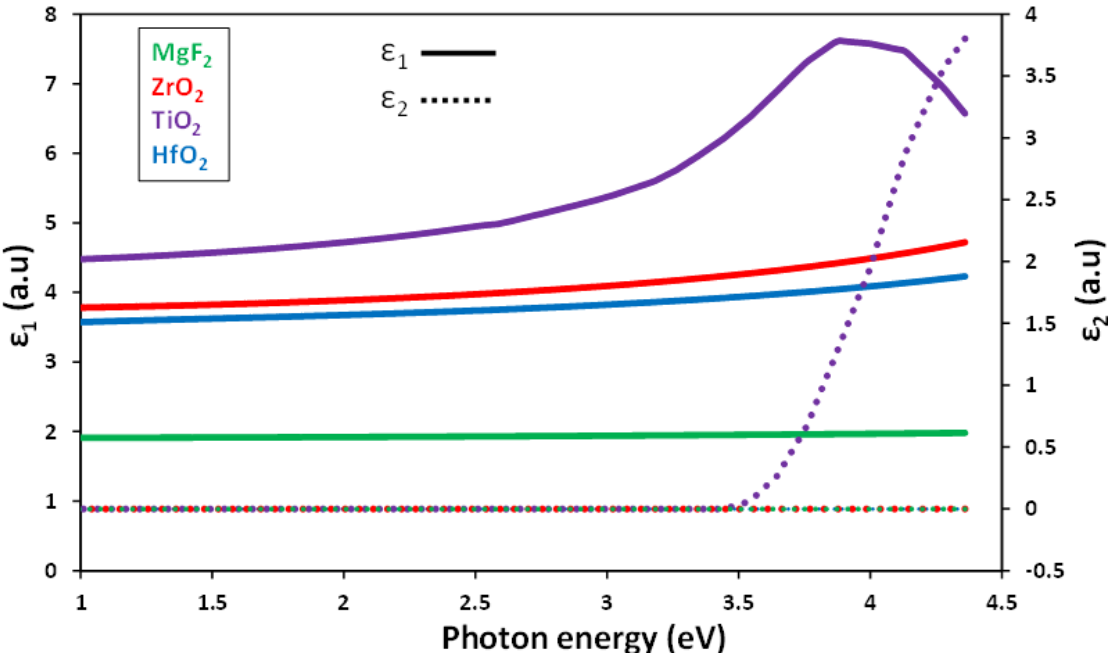

Figure 4. 5: Real and imaginary parts of the dielectric functions (ε_1, ε_2) of MgF_2, HfO_2, ZrO_2 and TiO_2 as deduced by ex-situ spectroscopic ellipsometry.

TABLE 4. 2 VALUES OF THE CAUCHY PARAMETERS OBTAINED FROM FITS OF THE INDEX OF REFRACTION AND EXTINCTION COEFFICIENT SPECTRA

Layer	**A**	**B**	**C**	k_0
MgF_2	1.38 ± 0.02	0.0023 ± 0.0117	1.38 ± 0.02	0.0000 ± 0.0452
HfO_2	1.89 ± 0.01	0.0089 ± 0.0102	0.0004 ± 0.0024	0.0058 ± 0.0460
ZrO_2	2.22 ± 0.02	0.0060 ± 0.0115	0.0008 ± 0.0021	0.0154 ± 0.0512
TiO_2	2.38 ± 0.02	0.0465 ± 0.0119	0.0028 ± 0.0026	0.6242 ± 0.0498

4.3 Single layer AR Coating on Ultra-thin CIGS device

For a thick CIGS layer (2 μm), a single layer of MgF_2 coating is sufficient to reduce the top reflection. When the thickness of the absorber layer is reduced however, a single MgF_2 layer is no longer capable to reduce the reflection to a reasonable level. Figure 3 depicts the simulated reflectance from a thick CIGS device and an ultra-thin CIGS device with and without the MgF_2 AR layer with different thickness. The quantum efficiency, transmittance and reflectance of an ultra-thin CIGS device with MgF_2 AR layer was simulated using transfer matrix theory and is shown in Figure 4.7. This gives an overview of the optical losses in an ultra-thin CIGS device. The losses cannot be compensated by a single MgF_2 AR layer.

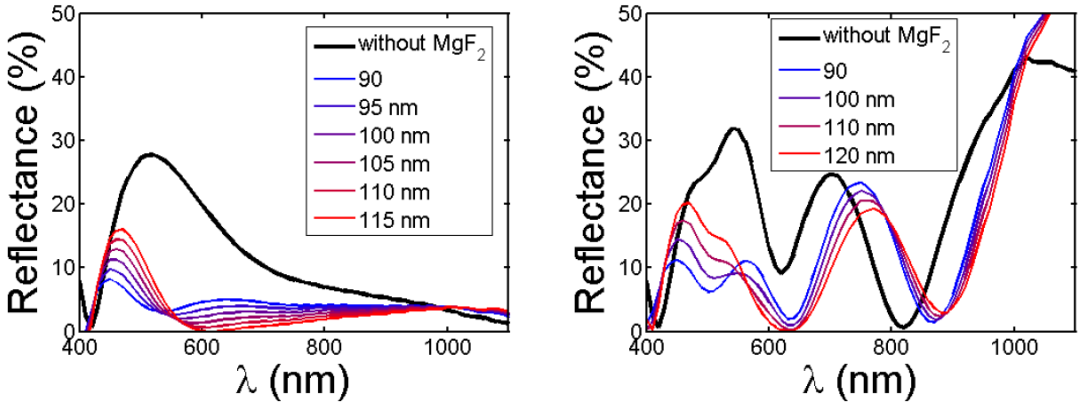

Figure 4. 6:Simulated reflectance from a regular CIGS device (left) and ultra-thin CIGS device with MgF_2 AR layer of varied thickness

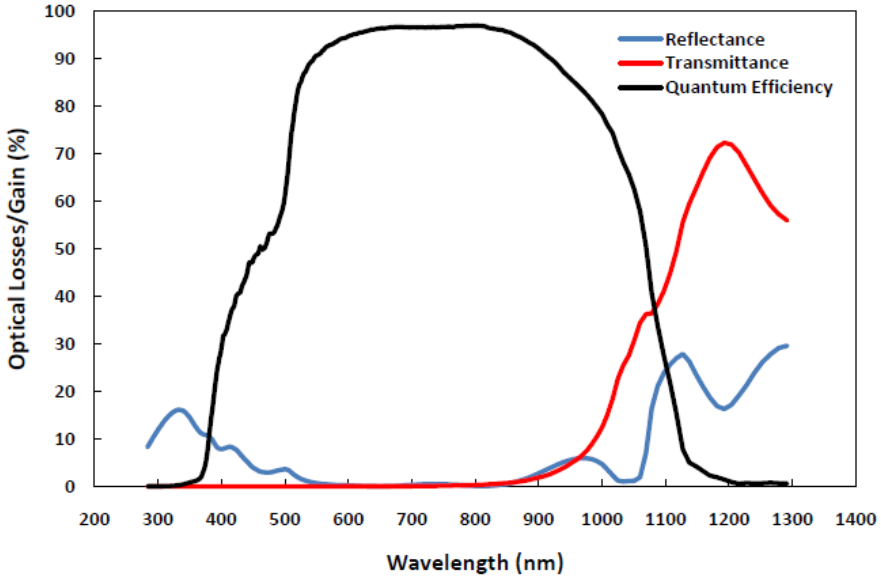

Figure 4. 7: Simulated QE, Transmittance and Reflectance of an ultra-thin CIGS device with MgF_2 AR layer

4.4 Three Layer Graded Anti-Reflective Coating

A single layer AR coating is not an effective solution to reduce reflectance for majority of the multi-layer structures. An alternative way of reducing reflectance is to gradually reduce the refractive index of the film from the refractive index of the substrate to the refractive index of air. A step-down index profile imparts a smooth transition of refractive index from a higher value of the substrate to the lower value of air. The multiple layers are modeled based on a periodic structure made of graded index profiles. These AR structures are called as graded refractive index (GRIN) structures. The smooth index transition between the two optical layers over a length scale can fairly suppress the reflection over a wide spectral and angular range. The multi-layer step gradient index stack affects the overall reflectance due to the discontinuity of refractive index at each interface of the structure and the total thickness of the stack affects the free spectral range [50]. The thicknesses of these layers are optimized to reduce the reflection for a specific spectral range leading to a reduced average reflectance. Figure 4.8 represents the schematic diagram of ultra-thin CIGS solar cell with a three layer graded anti-reflective coating. The thickness of each layer in the AR structure was varied to obtain the highest J_{sc} from the device. Many structures were investigated for the *3-layer AR* coatings, the QE, of these structures were simulated using the transfer matrix theory and is shown in Figure 4.9 and Figure 4.10 and the highest short circuit current density was found to be for the structure MgF_2(104 nm)/HfO_2(63 nm)/ZrO_2(140 nm) with $J_{sc\ max.}$ = 35.7 mA/cm^2.

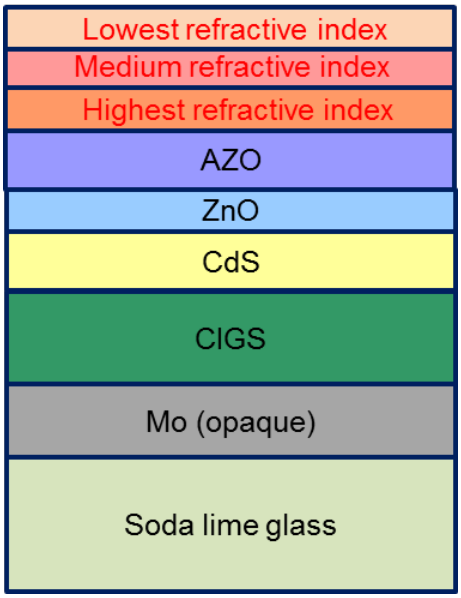

Figure 4. 8: Schematic diagram of ultra-thin CIGS solar cell with 3-layer graded ARC.

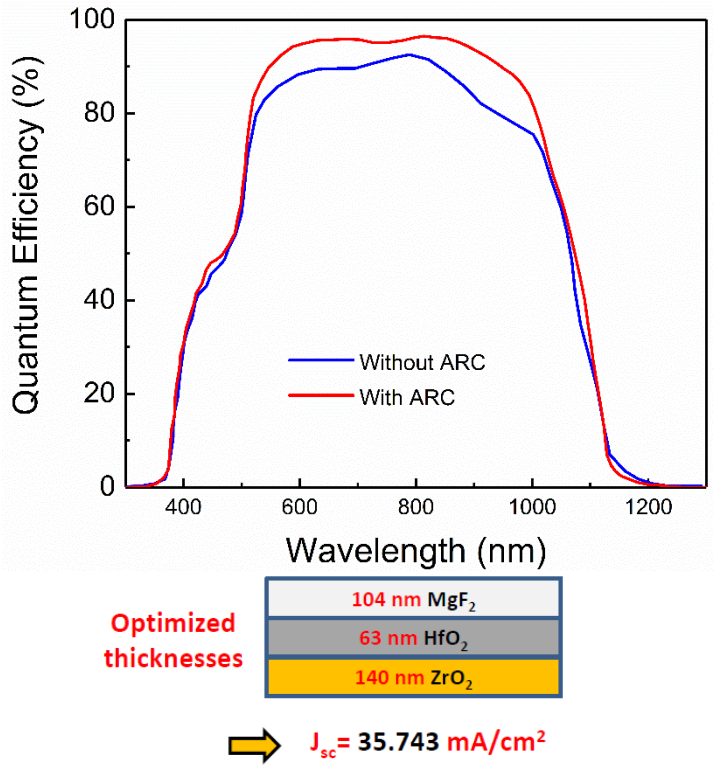

Figure 4. 9: Optimized thickness of 3-layer graded AR coatings to obtain highest Jsc.and simulated QE predicted for structures $MgF_2/HfO_2/ZrO_2$ structure

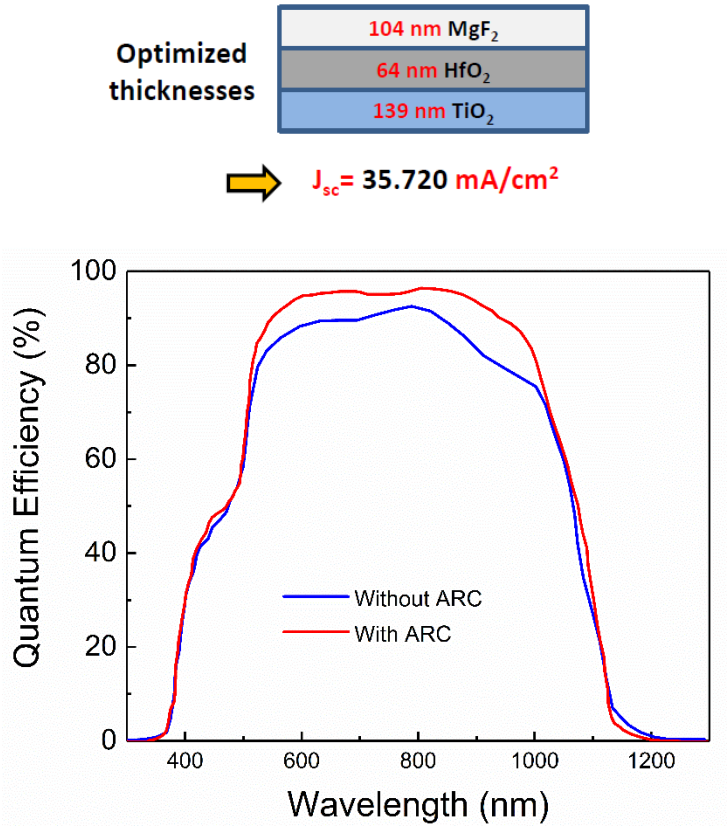

Figure 4.10: Optimized thickness of 3-layer graded ARC to obtain the highest Jsc and simulated QE predicted for structures with $MgF_2/HfO_2/TiO_2$ structure.

Figure 4.11 compares the reflectance and transmittance before and after the deposition of $MgF_2/HfO_2/ZrO_2$ AR coating on top of the standard TCO layers used for CIGS solar cells. The TCO layer was directly deposited on soda lime glass (SLG). The dependence of the optical properties of the AR coatings on the SLG substrate with TCO layers were evaluated as ZnO:Al is the top-most layer of the CIGS solar cell. Figure 4.12 shows the results obtained by investigating different materials including HfO_2, TiO_2, and ZrO_2 with the top layer being MgF_2. The reflectance was as low for $MgF_2/HfO_2/ZrO_2$ when compared to $MgF_2/TiO_2/MgF_2$ structure. The reflectance was as low as 13.0% for $MgF_2/HfO_2/ZrO_2$ when compared to $MgF_2/TiO_2/MgF_2$ having a reflectance of 15.5%.

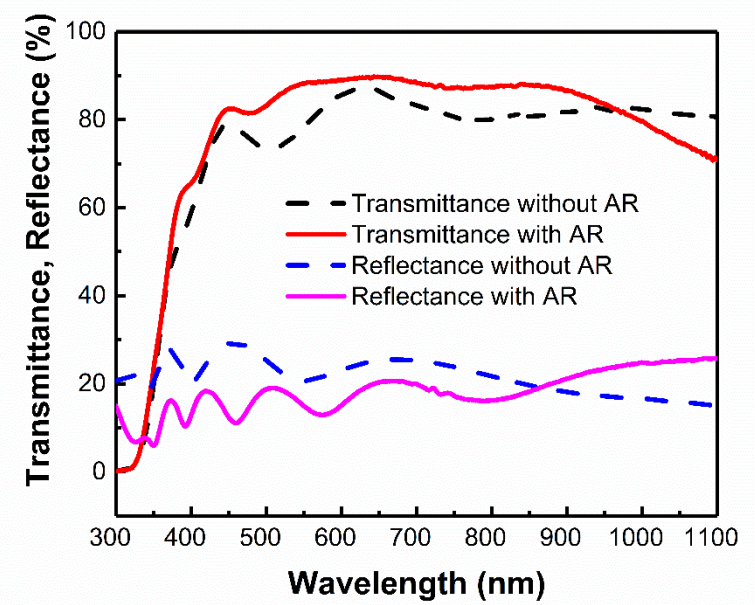

Figure 4. 11:Measured reflectance and transmittance spectra of a standard TCO structure on SLG before and after deposition of a 3-layer $MgF_2/HfO_2/ZrO_2$ AR coating.

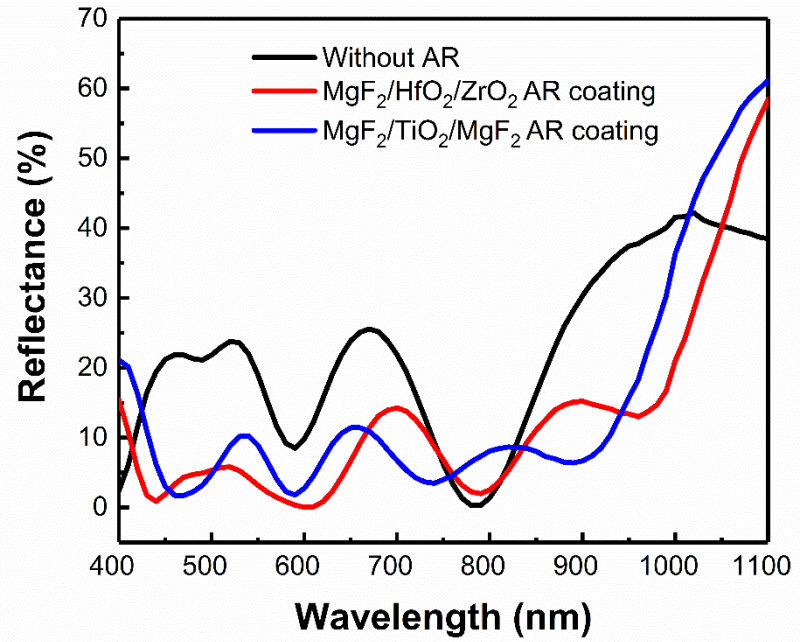

Figure 4. 12:Simulated QE, Transmittance and Reflectance predicted for structures with $MgF_2/HfO_2/ZrO_2$ structure.

The multiple layers are modeled based on a periodic structure made of graded index profiles. The thicknesses of these layers are optimized to reduce the reflection for a specific spectral range leading to a reduced average reflectance. Real time in-situ measurements were carried out to obtain relative reflectance of standard TCO structure on SLG with the multi-layer AR ($MgF_2/HfO_2/ZrO_2$) coatings. Figure 4.13 shows the relative real time reflectance measurement during the deposition of the three layers. The variations in reflectance were obtained for different wavelengths during the course of deposition of the three layers.

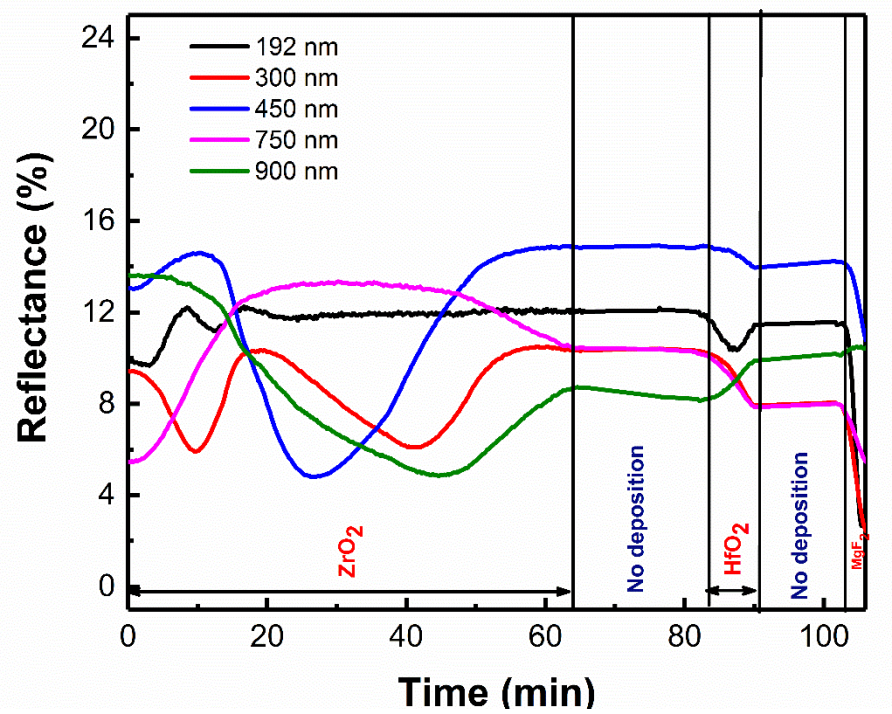

Figure 4. 13: Relative real time reflectance measurement during deposition for multi-layer AR coating on TCO substrate

These layers were deposited on TCO substrate by e-beam evaporation. The RTSE measurements were carried out *in-situ* during film growth using a rotating compensator, multichannel instrument with an energy range of 0.75–6.5 eV at an angle of incidence of 65°. The optical structure with a continuously graded refractive index profile has more than

one reflectivity minimum at several wavelengths and thus can effectively reduce the reflection for extended range of wavelengths. Figure 4.14 shows the cross-sectional SEM image of the 3-layer AR coating. The image clearly portrays the columnar structure of the layers indicating good adhesion between the three layers although the layers remain clearly distinct. Figure 4.15 compares the optimized (designed) values of thickness and refractive index of each layer in the 3-layer AR structure with the measured ones, confirming that the structure was well deposited. Figure 4.16 shows the AFM image after three layers of deposition. The cross-sectional SEM images and the AFM images allow correlating the modeled thickness and surface roughness of the structure to the measured ones, and shows that appropriate values were obtained.

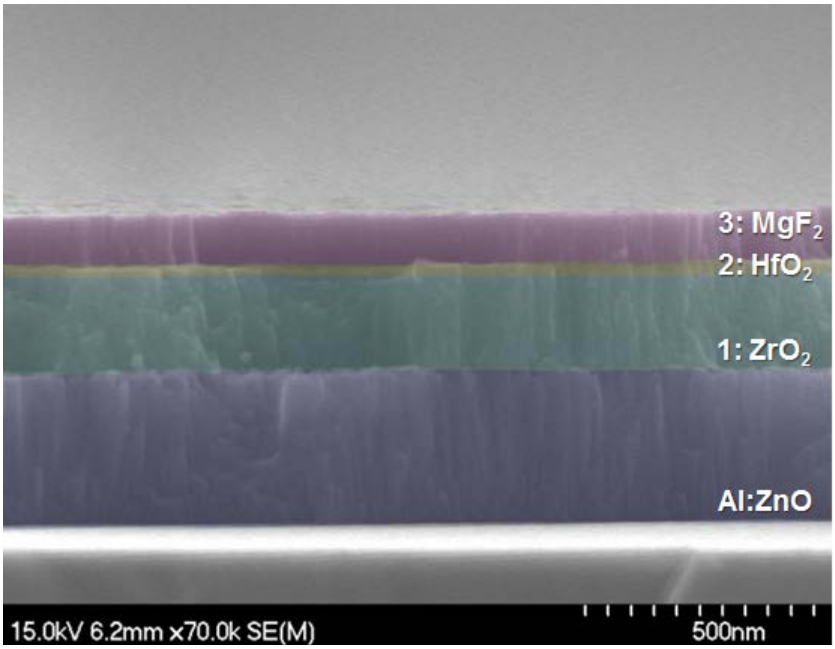

Figure 4. 14: Cross-section SEM image of the 3 layer AR coating on TCO substrate.

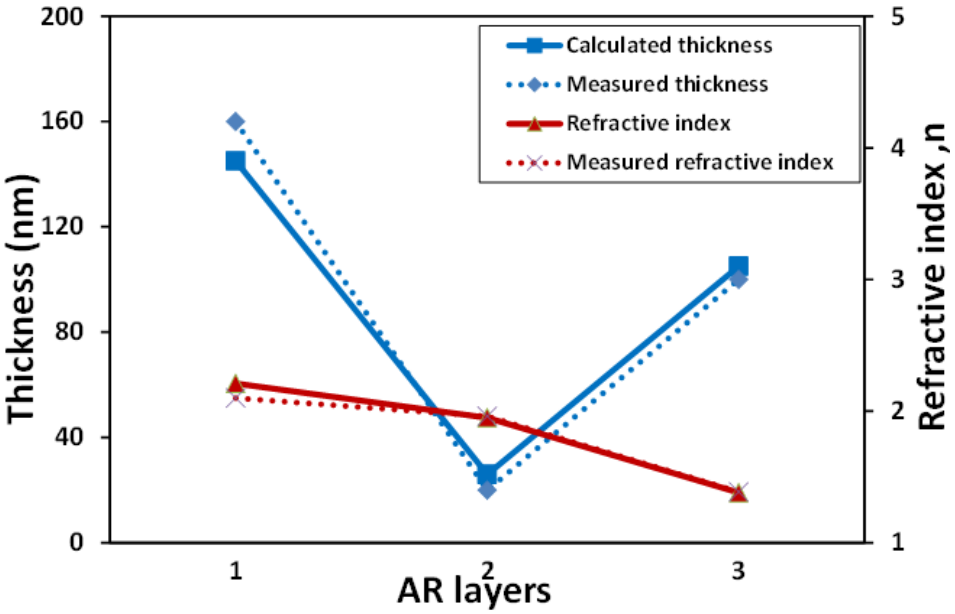

Figure 4. 15: Designed and measured values of thickness and refractive index of each layer for the optimized $MgF_2/HfO_2/ZrO_2$ coating.

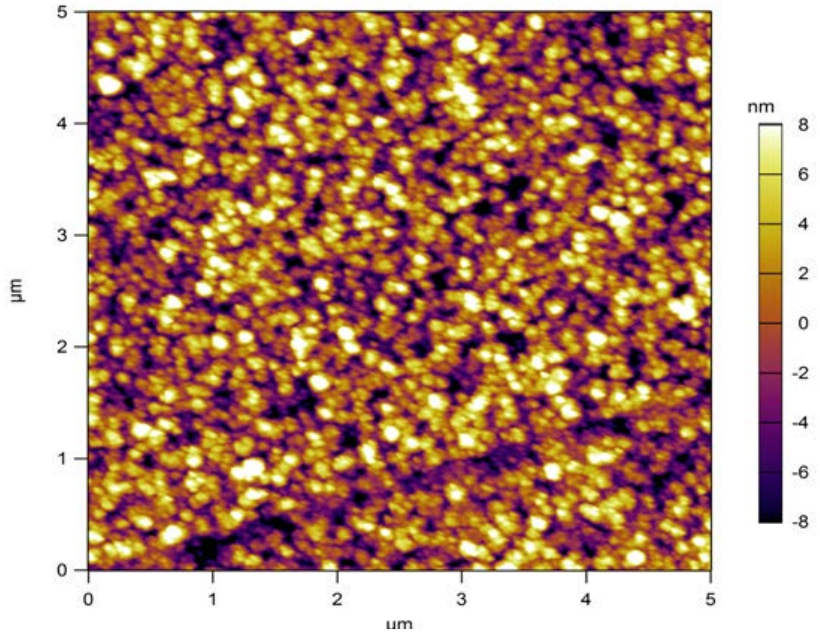

Figure 4. 16: AFM image after three layers of deposition

Optimized JV-QE Results

The effect of the AR layers on ultra-thin CIGS device with three layer graded AR structures has been summarized in Table 4.3. The J_{sc} has been considerably enhanced with the multi-layer ar coatings and can be correlated with the modeled reflectance curves (Figure 4.12). There is almost 8% increase in the J_{sc} with the optimized multi-layer structure ($MgF_2/HfO_2/ZrO_2$) when compared to using a single layer AR coating. Figure 4.17 compares the QE spectra of the ultra-thin cigs device with a single layer AR coating and a multi-layer AR coating structure and the effect of having a multilayer AR structure can be easily differentiated.

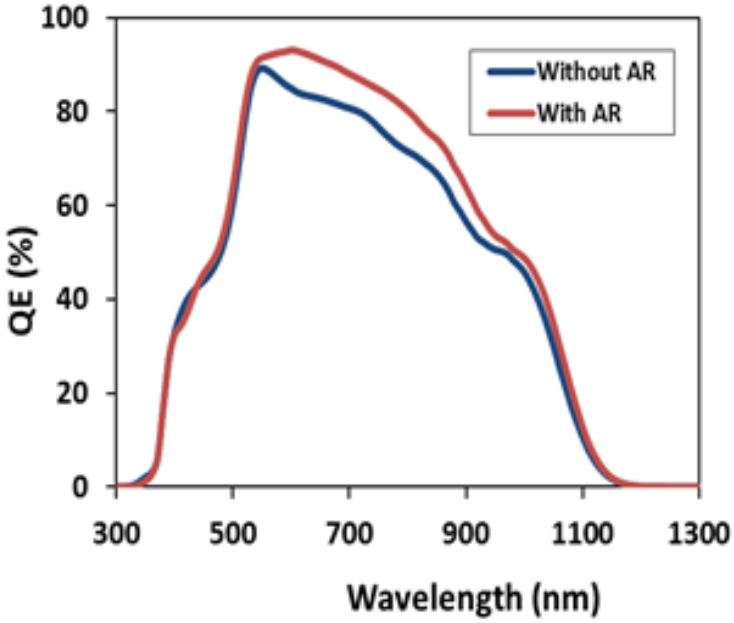

Figure 4. 177:QE spectra of the ultra-thin CIGS device with a single layer AR coating and a multi-layer AR coating structure

TABLE 4. 3 EFFECT OF GRADED AR LAYERS ON ULTRA-THIN CIGS SOLAR CELL

AR coating	**Jsc (mA/cm^2)**
Multi-layer AR ($MgF_2/HfO_2/ZrO_2$)	29.8
No AR	27.5

CHAPTER 5

MULTI-LAYER ANTI-REFLECTIVE COATING WITH HIGH/LOW INDEX PROFILE FOR ULTRA-THIN CIGS SOLAR CELLS

By employing multiple layer AR coatings, it is possible to increase the optical path length in the CIGS by multiple internal reflection and thus to reduce considerably the average reflectance from the surface of the cell. The reflection from the first surface of the cell cannot be completely cancelled through destructive interference with the weaker reflection from the top surface. With a graded index AR structure, it is a herculean task to attain index matching or optical impedance matching. The practical approach of reducing the packing density of the films to attain index matching will however distress the mechanical strength of the ARC's and thus will raise durability issues in the outdoor panels. Thus the characteristics of the single quarter wave layer can be improved by adding a high index half wave layer between the magnesium fluoride and the substrate which broadens the characteristics. The outer layer is made of a low- refractive material and the inner layer is made of high destructive index material.

5.1 Materials and Data Analysis

A wide variety of materials available for anti-reflection coatings, including MgF_2 and TiO_2, HfO_2, and ZrO_2 were deposited in a Kurt J. Lesker PVD 75 electron-beam evaporator. A base pressure lower than 10^{-6} Torr was obtained by a turbo-molecular pump prior to film depositions and the substrate holder was rotated at 15 rpm to ensure uniform deposition. Well-characterized Si wafer substrates were used, and the film/substrate was measured using ex-situ variable angle of incidence SE. Analysis of the SE data yields the

optical properties and film microstructure parameters. The deduced optical properties are shown in previous chapters.

5.2 Multi-Layer AR with High/Low Index Profile For Ultra-Thin CIGS Solar Cells

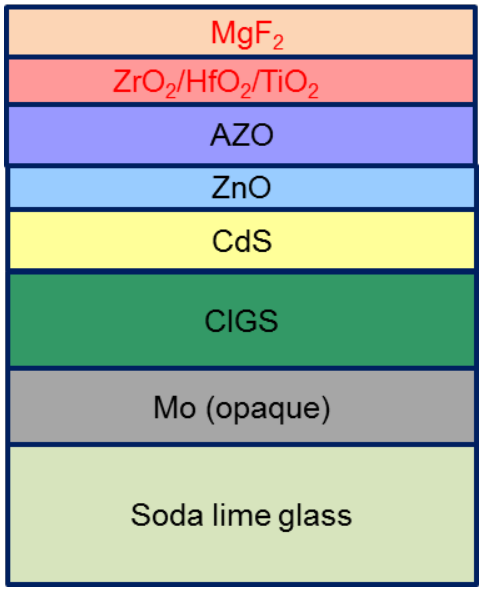

Figure 5. 1: Schematic diagram of ultra-thin CIGS solar cell with 2-layer ARC.

Anti-reflective (AR) coatings of 2 layers, 3 layers, and 5 layers have all been modeled and optimized with respect to short circuit current density. While 2- and 3-layer AR coatings significantly reduce reflectance across the wavelength range of operation of the solar cell, 5-layer AR coatings can theoretically decrease reflectance losses even more. However, this is valid only for planar-smooth interfaces. In the case of multilayer AR coatings, scattering can arise from rough interfaces and reduce the quality of the AR effect, and thus reduce the light delivered to the active layers.

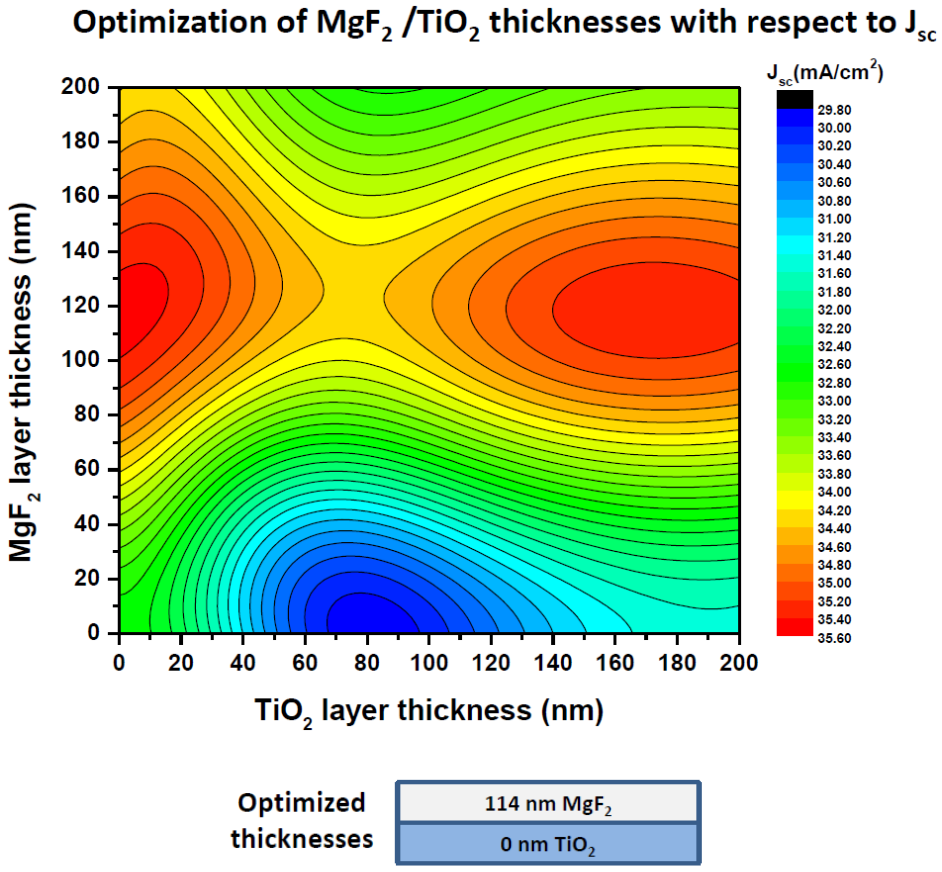

Figure 5.2:Predicted variation of Jsc with MgF_2/TiO_2 thicknesses: Jsc- 35.5 mA/cm^2

The effect of using a bi-layer AR coating on the simulated J_{SC} in a solar cell with 0.5 µm ultra-thin CIGS absorber layer was studied. For the *2-layer AR* structures investigated as shown in Figure 5.1, thickness of both layers in the AR structure was varied between 0-200nm using steps of 2nm and resulting J_{sc} was plotted as a function of thickness of MgF_2 layer and layer with high refractive index. Figure 5.2 illustrates simulated variation of J_{sc} for an AR structure as mentioned - MgF_2 (120 nm)/TiO_2 (200 nm). The highest short circuit current density was predicted for $J_{sc\ max.}$ = 35.5 mA/cm^2. Figure 5.3 shows simulated variation of J_{sc} with with an AR structure - MgF_2 (120 nm)/ZrO_2 (200 nm). The highest

short circuit current density was predicted for $J_{sc\ max.}$ = 35.5 mA/cm^2. The highest short circuit current density was predicted for a structure - MgF_2(120 nm)/HfO_2(200 nm) which gives $J_{sc\ max.}$ = 35.6 mA/cm^2 as shown in Figure 5.4 This approach to simulation helps in expediting the optimization of solar cells by estimating the required layer thicknesses even before any experiments are carried out.

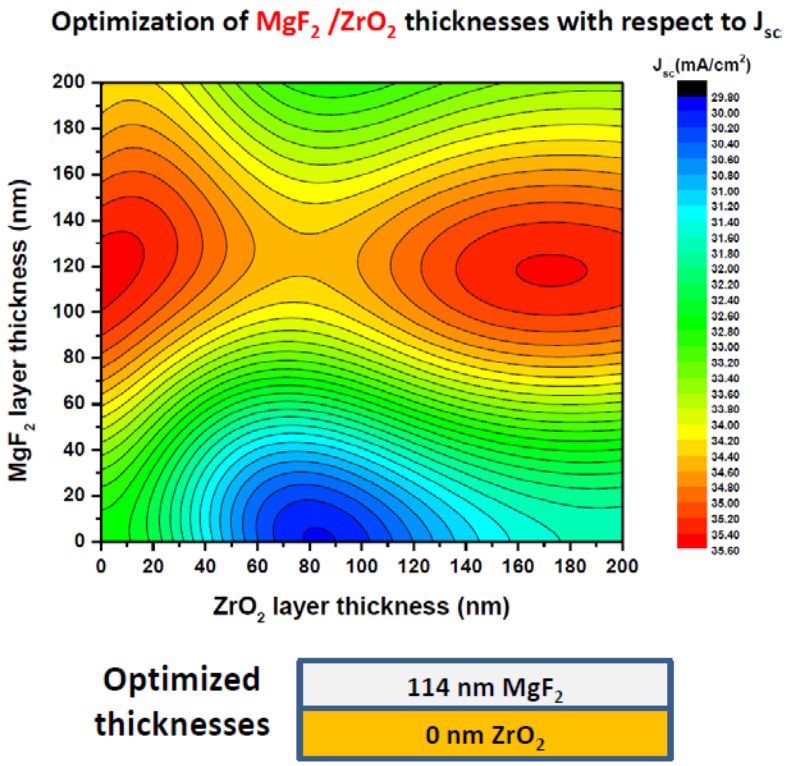

Figure 5. 3: Predicted variation of Jsc with MgF_2/ZrO_2 thicknesses; Jsc : 35.5 mA/cm^2

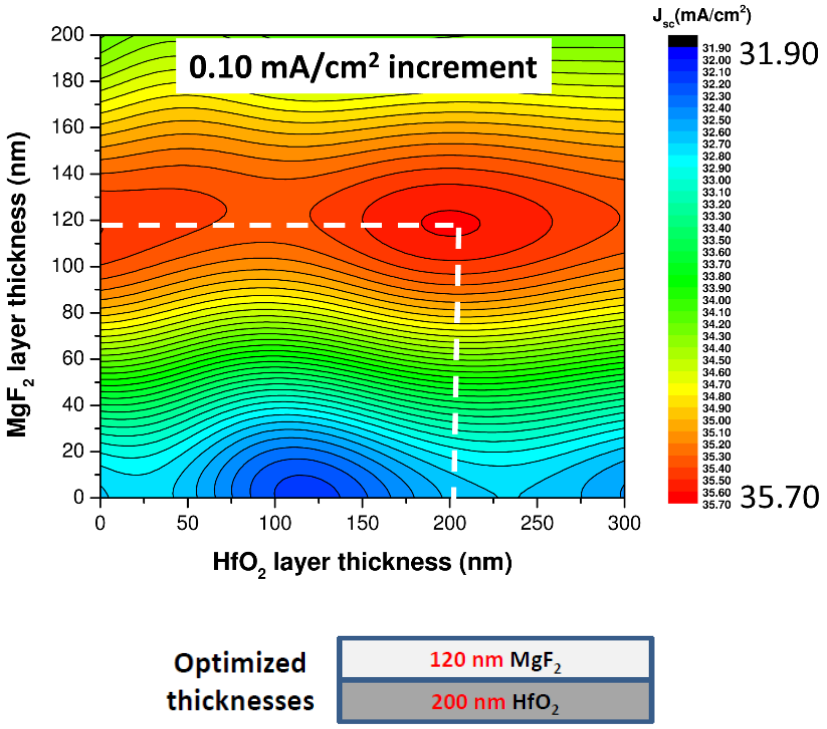

Figure 5. 4: Identification of optimum two-layer AR from EQE/JSC simulations. Predicted variation of Jsc with MgF_2/HfO_2 thicknesses; Jsc : 35.6 mA/cm^2

Figure 5.5 shows the reflectance and transmittance before and after deposition of a MgF_2/HfO_2 AR coating on top of the standard TCO layers used for CIGS solar cells. The TCOs were in turn deposited directly on soda lime glass (SLG). This study was performed to evaluate possible substrate dependence of the optical properties of the AR coatings, comparing results for a Si substrate and for ZnO:Al, which is the top-most layer of the CIGS solar cell.

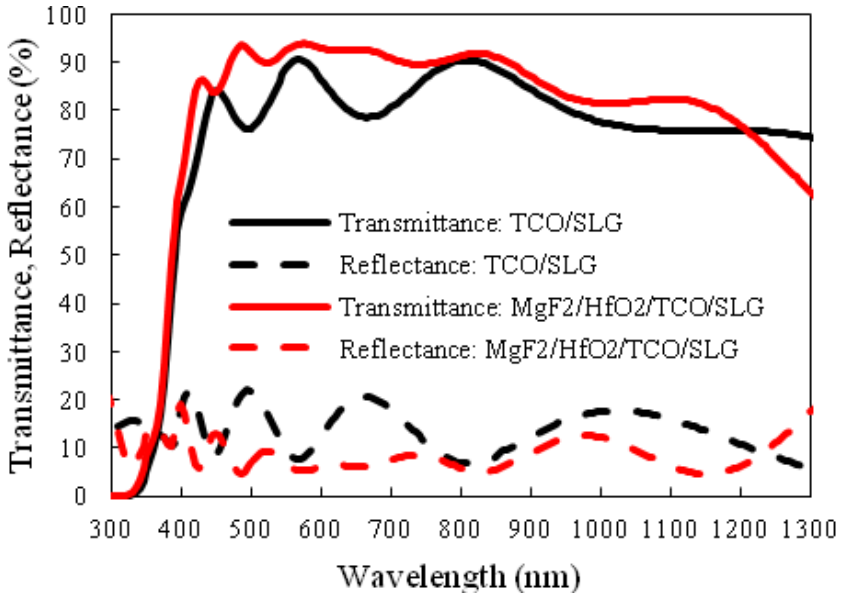

Figure 5. 5:Measured reflectance and transmittance spectra of a standard TCO structure on SLG before and after deposition of a 2-layer MgF_2/HfO_2 AR coating

Optimized JV-QE results

The deposition process of CIGS absorber layers were optimized to obtain an increase in the efficiencies for ultra-thin CIGS cells. The thickness of the CIGS layer was varied from 2μm to 0.7 μm, 0.5 μm and 0.36 μm. To our knowledge, these are among the highest efficiencies reported for cells with ultra-thin CIGS. The results are summarized in Table 5.1 and the experimental EQE's for devices with 0.5 μm thick CIGS are shown in Figure.5.6 A bi-layer AR coating (MgF_2/HfO_2) with layer thicknesses optimized by simulation was deposited on the solar cell with 0.5 μm CIGS.

TABLE 5. 1 PERFORMANCE OF SOLAR CELLS WITH STANDARD CIGS THICKNESSES AND THIN CIGS LAYERS.

CIGS d_{eff} (μm)	**AR coating**	**V_{oc} (V)**	**FF (%)**	**J_{sc} (mA/cm^2)**	**Eff. (%)**
standard 2 μm	3-stage (MgF_2 AR)	0.63	74	34.0	15.9
0.7310 ± 0.0010 μm	(no AR)	0.55	70.8	32.7	12.8
	(MgF_2 AR)			33.8	13.2
0.50 μm	(no AR)	0.52	63.5	27.6	9.0
	(MgF_2 AR)			30.9	10.1

The measured reflectance of the cell before and after the coating is shown in Figure 5.7 and Figure 5.6 compares the effect of the bi-layer AR coating on the EQE. There is an approximate improvement of around 4.4 mA/cm^2 in J_{sc} and the reflectance response was reduced significantly after adding the AR coating. The efficiency of the cell increased from 9.02 % to 10.10 % with the inclusion of the coating. The lower measured EQE relative to the calculation over the 400-1000 nm range is attributed to electron-hole collection losses. The higher measured EQE relative to the model at wavelengths > 1000 nm can be attributed to light scattering which is not included in the optical model.

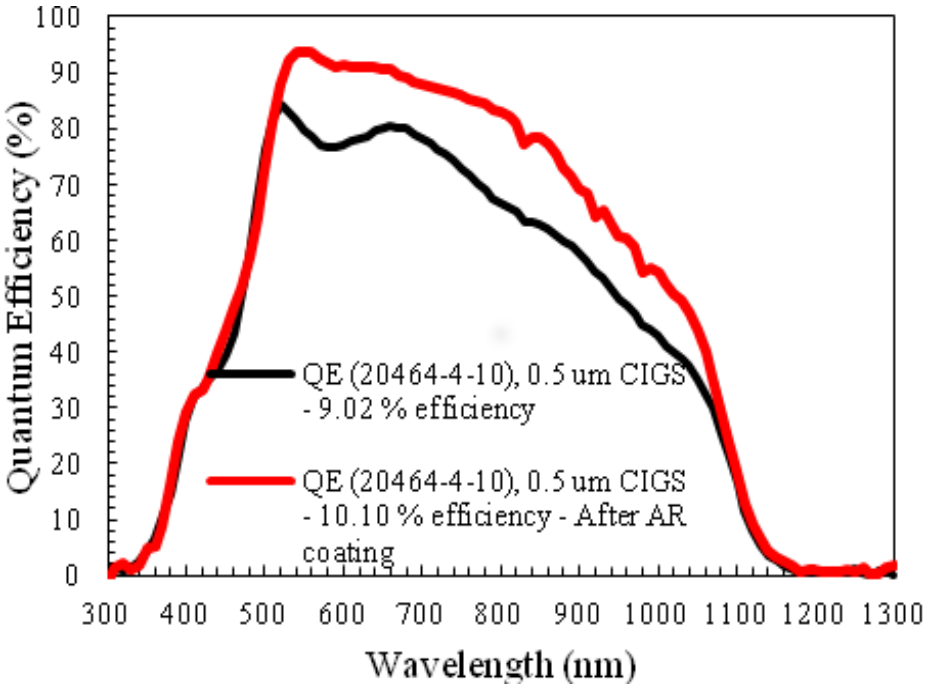

Figure 5. 6:External quantum efficiency (EQE) for a solar cell with 0.5 µm CIGS

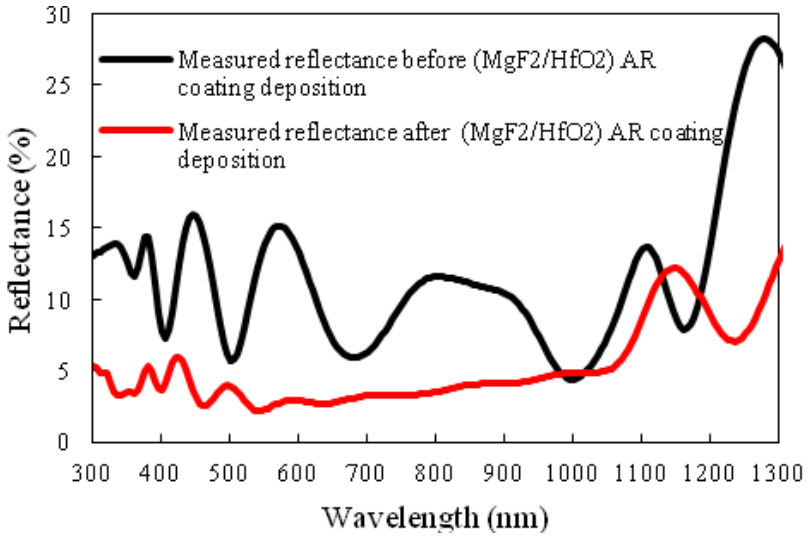

Figure 5. 7: Measured reflectance spectra of a solar cell with a 0.5 µm CIGS absorber layer before application of an AR coating and after deposition of a 2-layer MgF_2/HfO_2 AR coating

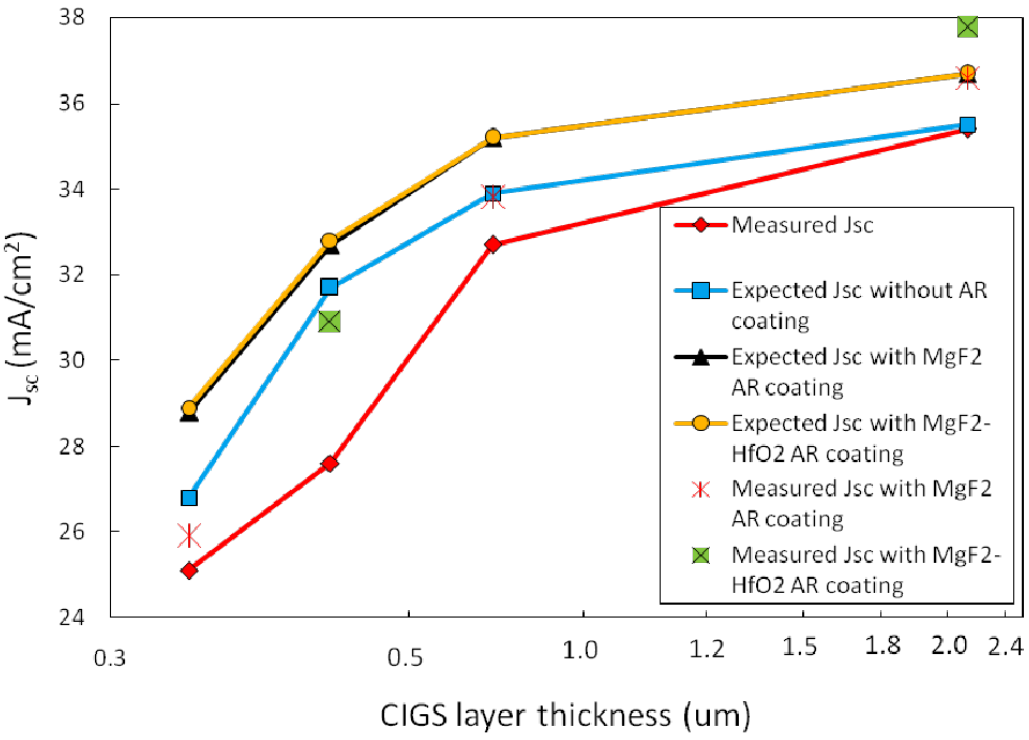

Figure 5. 8: Measured and optically simulated Jsc values for CIGS solar cells with standard and thin absorbers with and without AR coatings

5.3 Three layer AR Structure:

The AR structure was modified including a three layer AR structure to improve the light trapping. Figure 5.9 illustrates the structure of an ultra-thin CIGS device with a three layer AR structure. Figure 5.10 illustrates a simulated effect of the AR coating on the reflectance of an ultra-thin CIGS device. The simulated model shows a clear advantage of having a multi-layer AR over a single layer AR coating for the device.

Figure 5. 9:Schematic diagram of ultra-thin CIGS solar cell with 3-layer ARC.

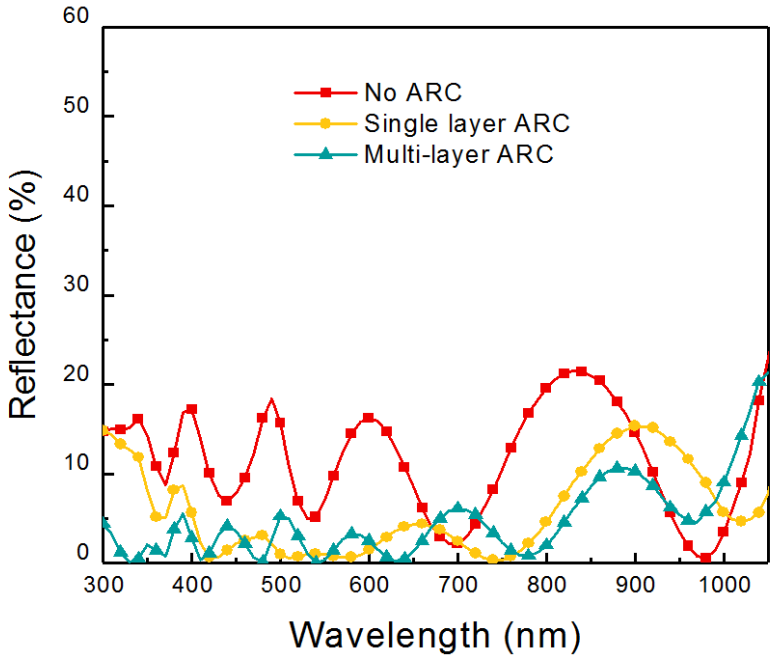

Figure 5. 10: Simulated reflectance spectra of ultra-thin CIGS device with multi-layer AR coating

5.4 Four layer AR coating with High/Low Index Profile

The optical properties of single thin film or an assembly of thin films can be completely described by a characteristic matrix for given wavelength. Herpin equivalent layers concept is applied in three layer gradient coating, where medium index is replaced by a combination of high and low index materials for two layer coating. This concept can be used to reduce a complex multi-layer structure with symmetrical sub components to a simpler structure for ease of modeling and design. Thus a high/low/high/low index (HLHL), two material AR coating can be used to approximate the optical performance of the gradient coating structure[51-55]. Reflectance modeling designs are implemented for CIGS devices with 0.5 µm absorber thickness. The variation in reflectance is simulated for a combination of different 4-layer AR coatings following a [high-refractive-index (H)]/[low-refractive-index (L)]/H/L structure. MgF_2 serves as the low refractive index layer (L) in all cases, whereas H designates a high refractive index layer, which is either ZrO_2, HfO_2, or TiO_2. Simulations of QE spectra for the different AR coatings on CIGS devices are shown in Figure 5.11, along with those for no AR coating or a single layer MgF_2 AR coating. The structure of the AR coating is designed based on the optical properties of the underlying structure, such that the overall reflectance spectra from the device is minimized. A structure based on HfO_2 and MgF_2 provides a smooth transition in refractive index from the top of the cell to air. Thus, it is important to note that the simulations are carried out to reduce the average reflectance for each structure, yielding a different thickness for each layer in each of the optimized structures. The results exhibit a reduction of reflectance from 14 % to 6 % for an AR structure of $MgF_2/HfO_2/MgF_2/HfO_2$. The reflectance curves for the different structures investigated is shown in Figure 5.12. The reduction in reflectance

spectra can be correlated with the refractive index of the material used in the structure. The multi-layer structure with HfO_2 provides the least reflectance (6%) and the structure with TiO_2 has the highest reflectance (8%). Therefore, it is very crucial to select the right material while designing the multi-layer AR structure.

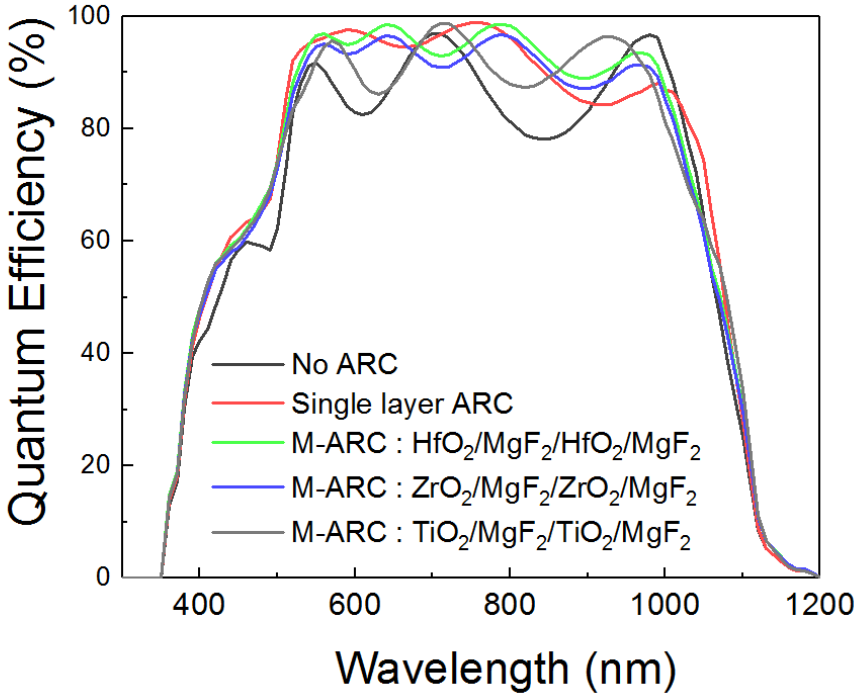

Figure 5. 11:Simulated quantum efficiency (QE) for an ultra-thin CIGS device (0.5 µm) without AR coating, with single layer AR coating (MgF_2), and with 3 different multilayer AR coating structures.

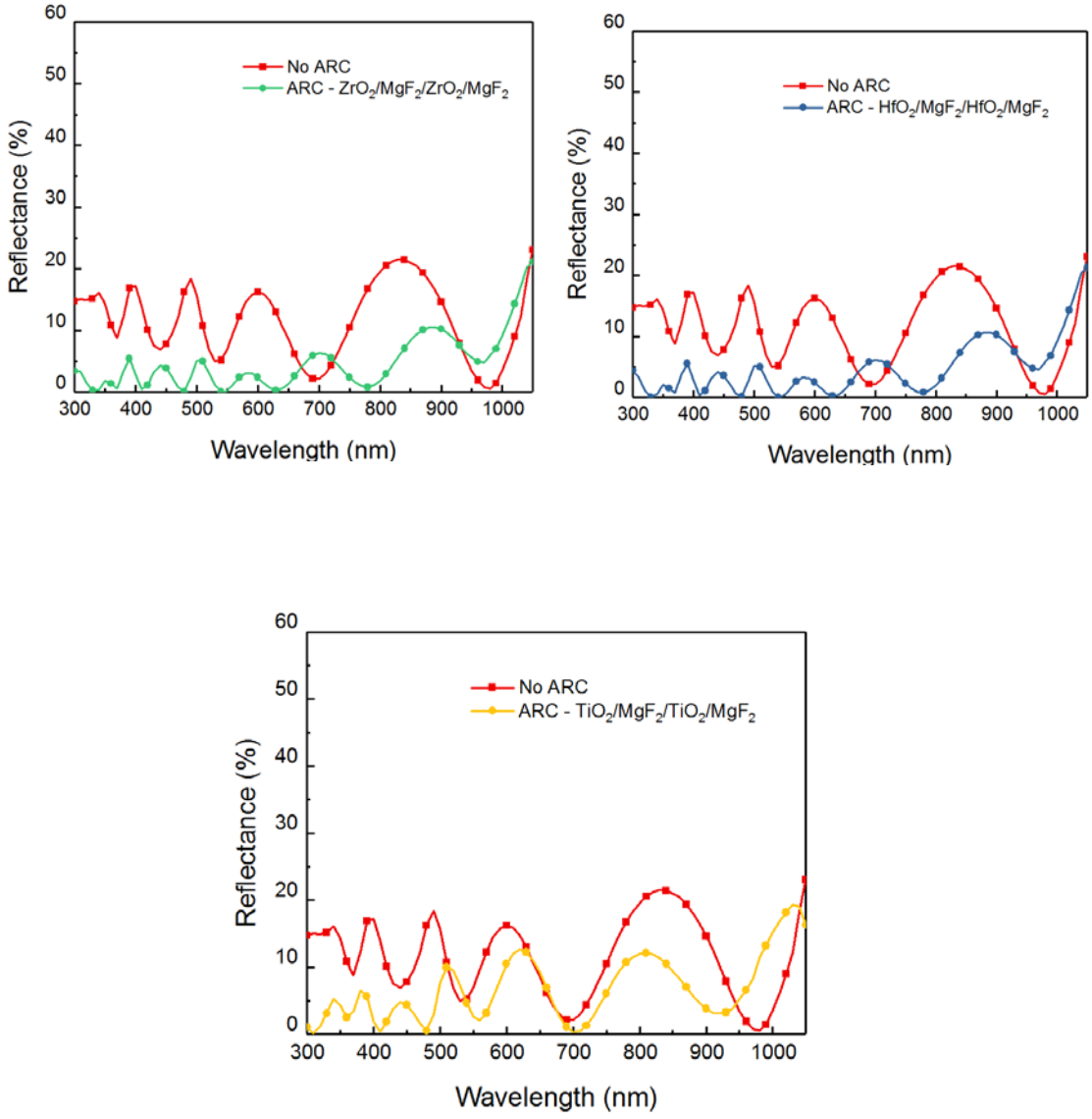

. Figure 5. 12: Simulated reflectance of an ultra-thin CIGS device with three layer AR structure.

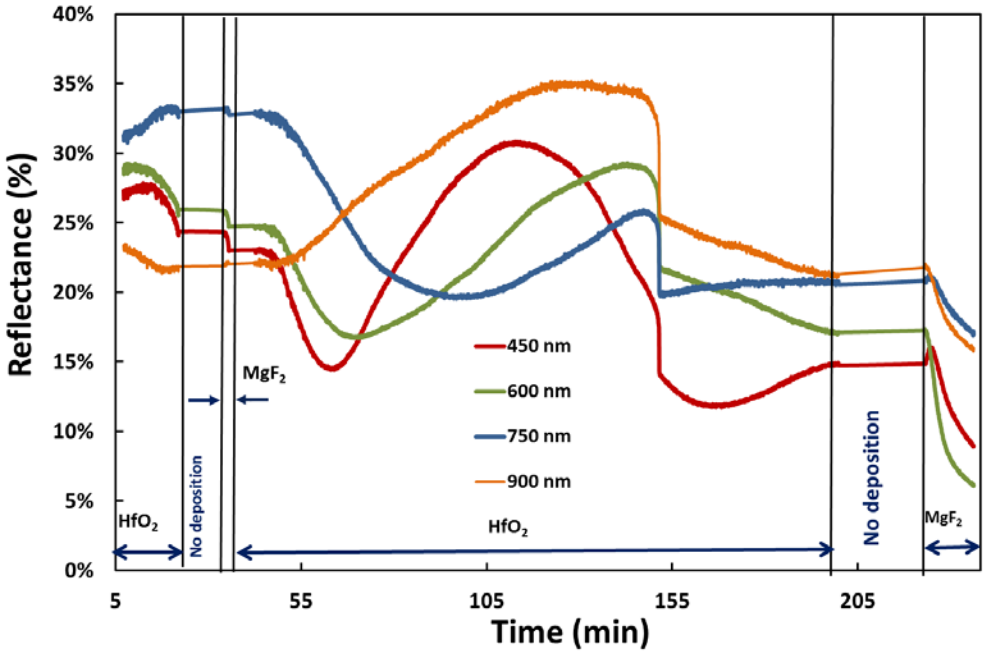

Figure 5.13: Real time reflectance during deposition of AR layer (HfO2/MgF2/ HfO2/ MgF2) on ultra-thin CIGS (600 nm) cell.

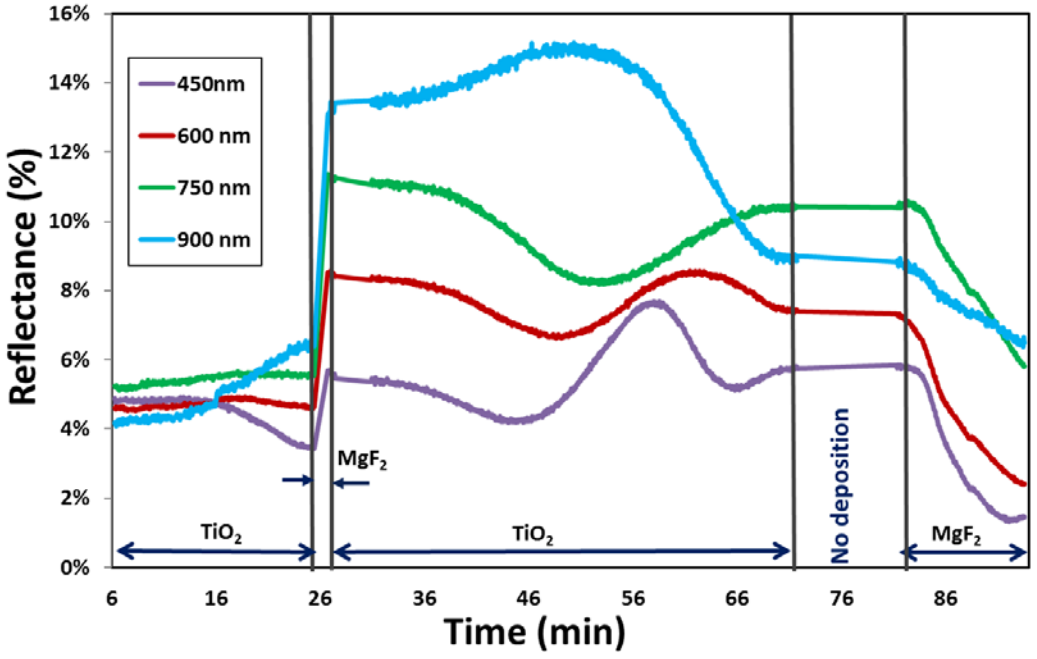

Figure 5. 14: Real time reflectance during deposition of AR layer (TiO2/MgF2 /TiO2/ MgF2) on ultra-thin CIGS (600 nm) cell.

These simulations serve to guide experiment by providing an estimated thickness for each layer. *In-situ* RTSE measurements are carried out to monitor the average reflectance of these multilayer AR structures on ultra-thin CIGS cells. *Ex-situ* reflectance measurements of the CIGS devices were also performed before and after the deposition of the multilayer AR structure, to supplement the RTSE measurements. Figure 5.13-5.14 shows the real time reflectance measurement acquired *in-situ* during deposition of the multilayer structure. It can be observed that the optical structure with the multilayer AR coating has more than one reflectance minimum at each wavelength and thus can effectively reduce the reflectance for an extended range of wavelengths. The utility of this demonstration is that *in-situ* monitoring during AR coating fabrication can be used for real time adjustment of the layer structure to ensure that the proper reflectance metrics are obtained from the combination of refractive index and thickness for each layer, as opposed to assuming reference values and deposition rates.

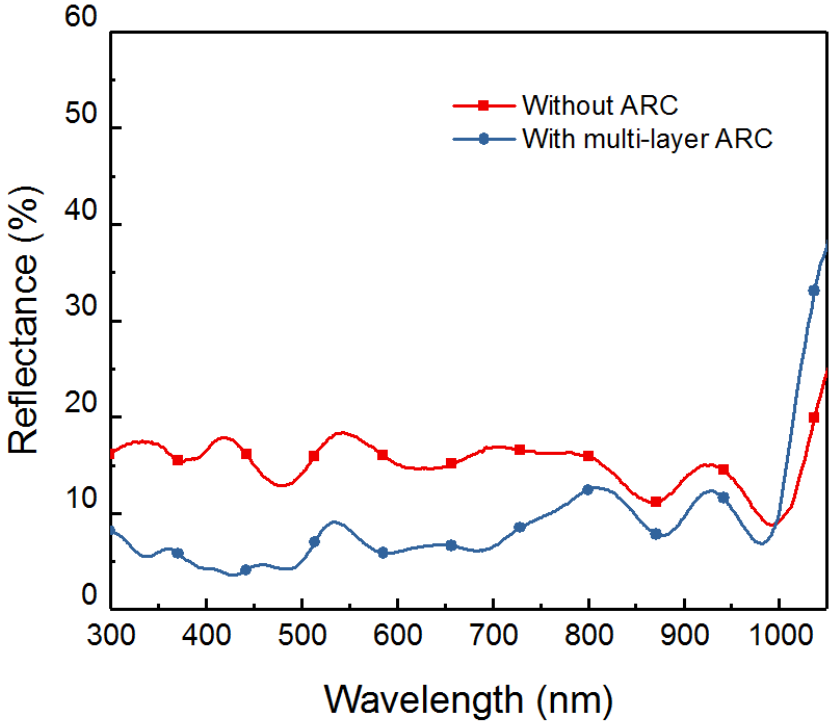

Figure 5. 15:Ex-situ reflectance before and after the deposition of the AR coating

Ex-situ reflectance measurements (Figure 5.15) of the CIGS devices were done before and after the deposition of the multi-layer structure, to correlate to the RTSE measurements. The optical structure with the multi-layer AR structure has more than one reflectivity minimum at several wavelengths and thus can effectively reduce the reflection for an extended range of wavelengths.

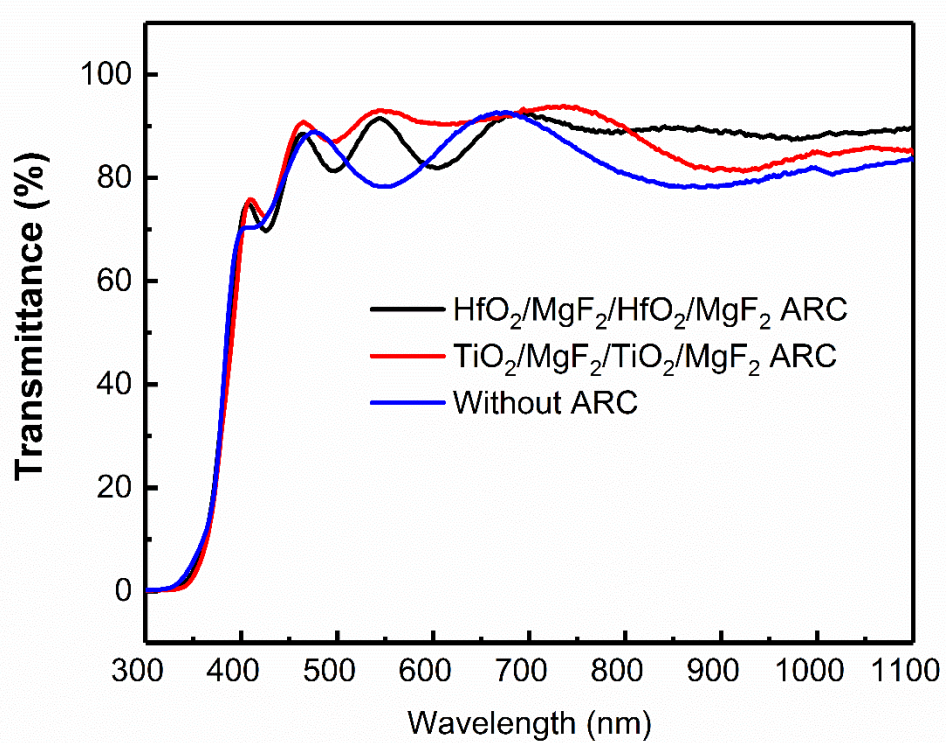

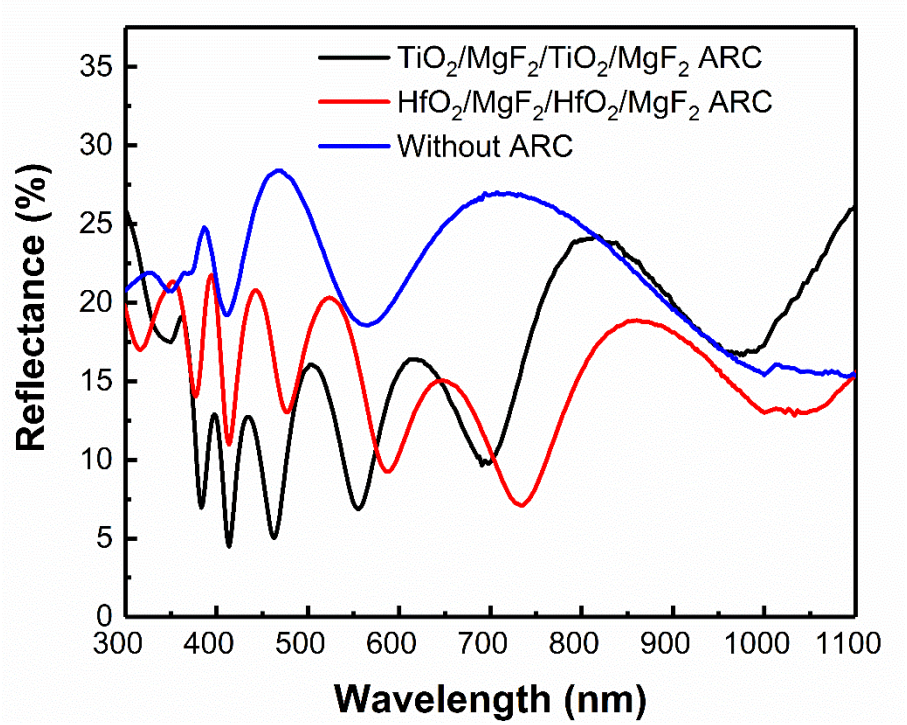

Figure 5. 16: Simulated reflectance and transmittance before and after deposition of a MgF2/HfO2 /MgF2/HfO2 AR coating on top of the standard TCO layers

Figure 5.16 shows the reflectance and transmittance before and after deposition of a $MgF_2/HfO_2/MgF_2/HfO_2$ AR coating on top of the standard TCO layers used for CIGS solar cells. The TCOs were in turn deposited directly on soda lime glass (SLG). This study was performed to evaluate possible substrate dependence of the optical properties of the AR coatings, comparing results for a Si substrate and for ZnO:Al, which is the top-most layer of the CIGS solar cell.

Optimized JV & QE Results

The effect of the AR layers on ultra-thin CIGS device with different AR structures has been summarized in Table 5.2. The J_{SC} has been considerably enhanced with the multi-layer AR coatings and can be correlated with the modeled reflectance curves (Figure 5.16). There is almost a 14% increase in the Jsc with the multi-layer structure ($HfO_2/MgF_2/HfO_2/MgF_2$) when compared to using a single layer AR coating which hardly gives an increase up to 8%. However, taking into consideration the high material cost of HfO_2, one can compromise to use the multi-layer AR structure with ZrO_2 as their performances are almost similar. Figure 5.17 compares the QE spectra of the ultra-thin CIGS device with a single layer AR coating and a multi-layer AR coating structure and the effect of having a multilayer AR structure can be easily differentiated. The deposition of the multi-layer AR coating increased the short circuit current density by almost 3.5 mA/cm^2 (14% relative increase) for the device shown in the figure.

TABLE 5. 2 EFFECT OF DIFFERENT AR LAYERS ON ULTRA-THIN CIGS DEVICE (0.55µm)

Sample ID	AR coating	η (%)	Jsc (mA/cm^2)	Voc (V)	FF (%)
SAMPLE I	MgF_2	9.1	28.2	0.54	59.8
	No AR	8.2	26.0	0.53	59.2
SAMPLE II	ZrO_2/MgF_2/ ZrO_2/MgF_2	9.4	28.4	0.55	60.3
	No AR	7.9	25.6	0.53	58.3
SAMPLE III	HfO_2/MgF_2/ HfO_2/MgF_2	9.1	28.4	0.55	58.2
	No AR	7.2	24.9	0.53	54.5

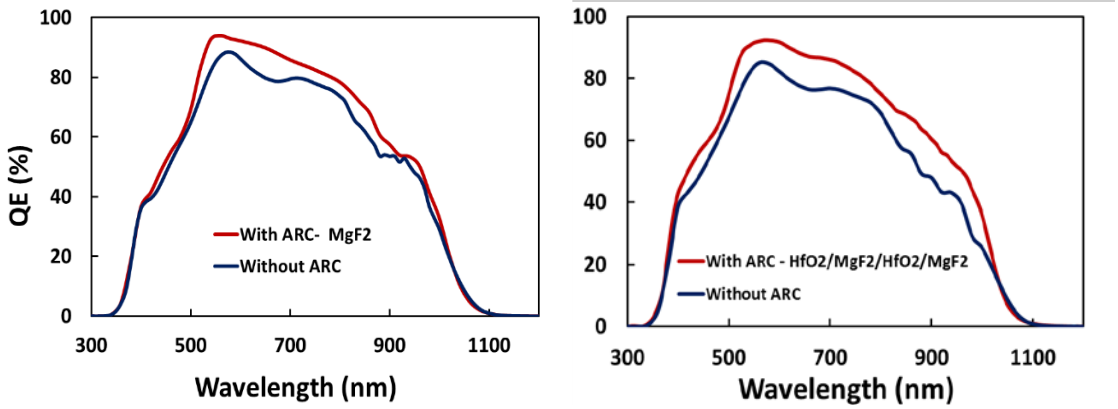

Figure 5. 17: Comparison of QE spectra for a 0.55 µm CIGS device with different AR structures.

5.5 Real time reflectance monitoring During Multi-layer Anti-reflective Layer Deposition

The average reflectance from the CIGS cell structure is closely monitored during the course of deposition of anti-reflective layers. The effect of the AR layers on CIGS devices with different CIGS thicknesses has been summarized in Table. 5.3. For a thick CIGS layer (2um), a layer of MgF_2 is sufficient to reduce the top reflection. However, with the reduced thickness of CIGS layer, the reflection from the first surface cannot be completely cancelled through destructive interference with the weaker reflection from the top surface. Thus the characteristics of the single quarter wave layer can be improved by adding a high index half wave layer between MgF_2 layer and the substrate to broaden the characteristics. With multi-layers, there are multiple minimum reflection points at different wavelengths and the average reflectance is comparatively reduced.

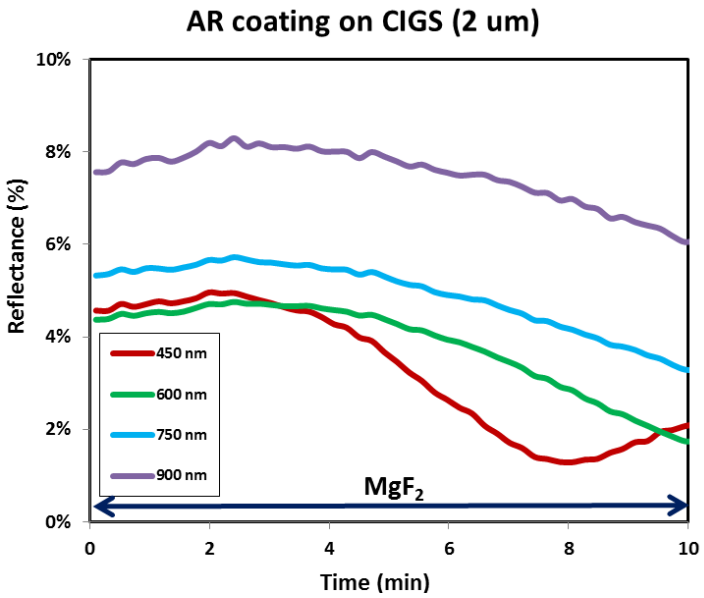

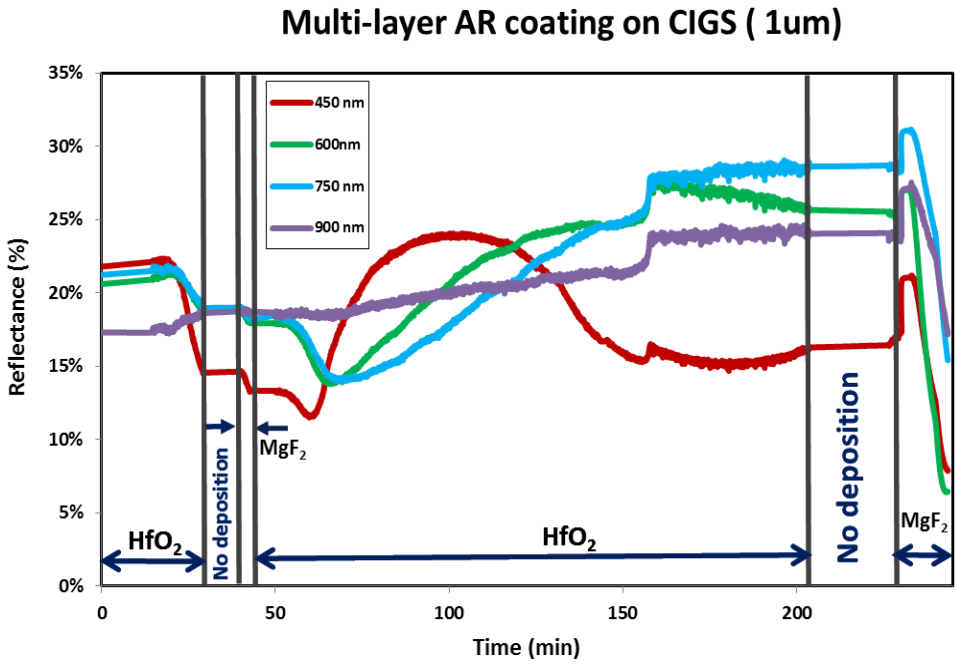

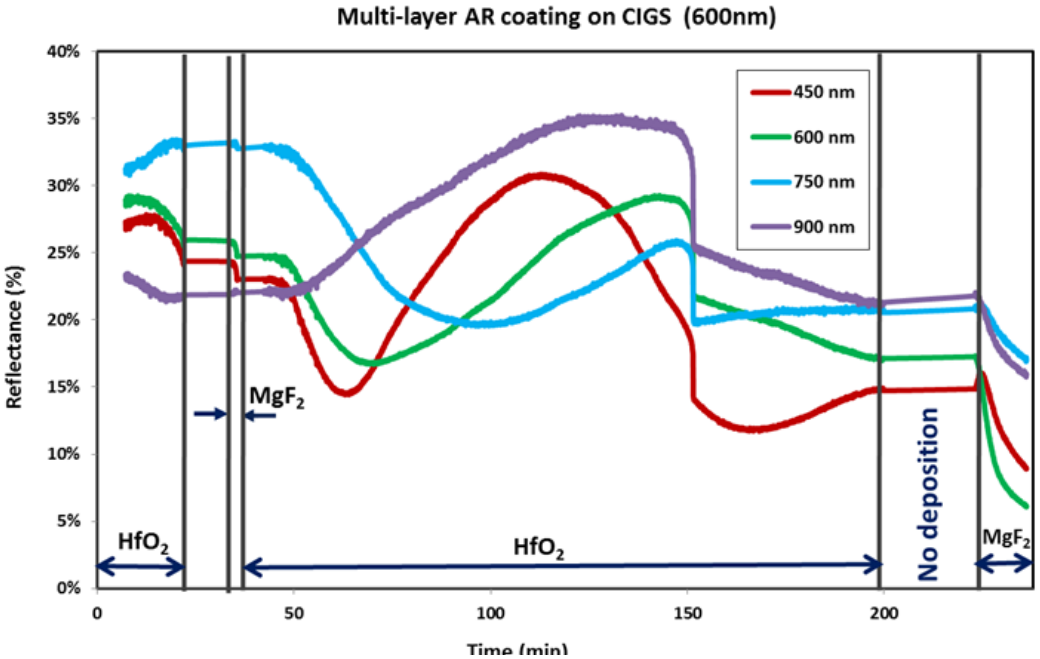

Figure 5. 18 Real time reflectance for CIGS devices with varied thickness with multi-layer AR

The J_{SC} has been considerably enhanced with the multi-layer AR coatings. The reduced Voc and FF for some cells is probably due to the increased substrate temperature and diffusion into cell structure caused due to lengthy hours of deposition time for the AR coatings. Figure 5.18 shows the real time reflectance for CIGS devices with varied thickness with multi-layer AR coatings and Table 5.3 shows the device summary for these samples.

TABLE 5. 3 DEVICE SUMMARY FOR DIFFERENT CIGS THICKNESS WITH AR LAYERS

Thickness (μm)	**AR coating**	**η (%)**	**Jsc (mA/cm^2)**	**Voc (V)**	**FF (%)**
2.0	MgF_2	17.6	37.5	0.64	73.1
	No AR	16.7	35.6	0.64	73.4
1.0	4 layer AR	11.9	32	0.58	64.7
	No AR	12.8	30.6	0.59	70.5
0.55	4-layer AR	10.8	28.1	0.59	64.7
	No AR	10.2	27.3	0.58	64.7

5.6 Alternative Nitrides Back Contacts for Ultra-Thin CIGS Solar Cells

As the thickness of the CIGS absorber is reduced to optimize the material costs, fabrication costs and/or bulk recombination losses, one pass of the light through the device is not sufficient for complete absorption. The absorption losses can be compensated by employing effective optical enhancement techniques by impinging light effective path lengths that are greater than the absorber thickness [56]. The optical losses can be

minimized by improving the reflectivity at the back of the device as increased scattering provides for diagonal light paths. Thus, a reflective back contact combined with an effective AR coating can improve the light trapping in the device. Application of alternative back contacts can also improve the device stability, offer better thermal expansion match with the other layers and reduce material and processing costs [57].

The different materials investigated as alternative back contacts include different metal nitrides such as ZrN and VN. Figure 5.19 shows the structure of the CIGS cell using alternative back contacts. ZrN and VN have high reflectivity in the red or near infra-red spectrum thus exhibiting approximately a 15% increase in the average reflectance when compared to using Mo as the back contact. This provides the possibility of multiple passes of light through the ultra-thin CIGS layer increasing the conversion efficiency. Figure 5.20 a). shows the reflection intensity for different back contacts[58]. Figure 5.20 b) compares the experimental results for reflection intensity of the CIGS device with alternative back contacts. One can see there that the quality of our nitrides is not good yet, as the reflectance is not as high as expected.

Multi-layer AR coatings can be used in conjunction with the back reflector to serve as a light trap in the red and the near infra- red region, where enhanced absorption is required. The goal is to achieve at least five passes in the internal reflection for complete absorption of light. The average reflectance of the ultra-thin CIGS devices with alternative back contacts and multi-layer AR coatings (TiO2/MgF2/TiO2/MgF2) is shown in Figure 5.21. It is observed that the average reflectance can be considerably reduced, by up to 40%, with this light trapping scheme.

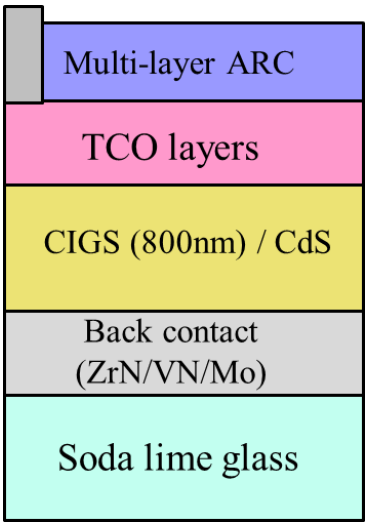

Figure 5. 19:Basic structure of CIGS device with alternative back contacts

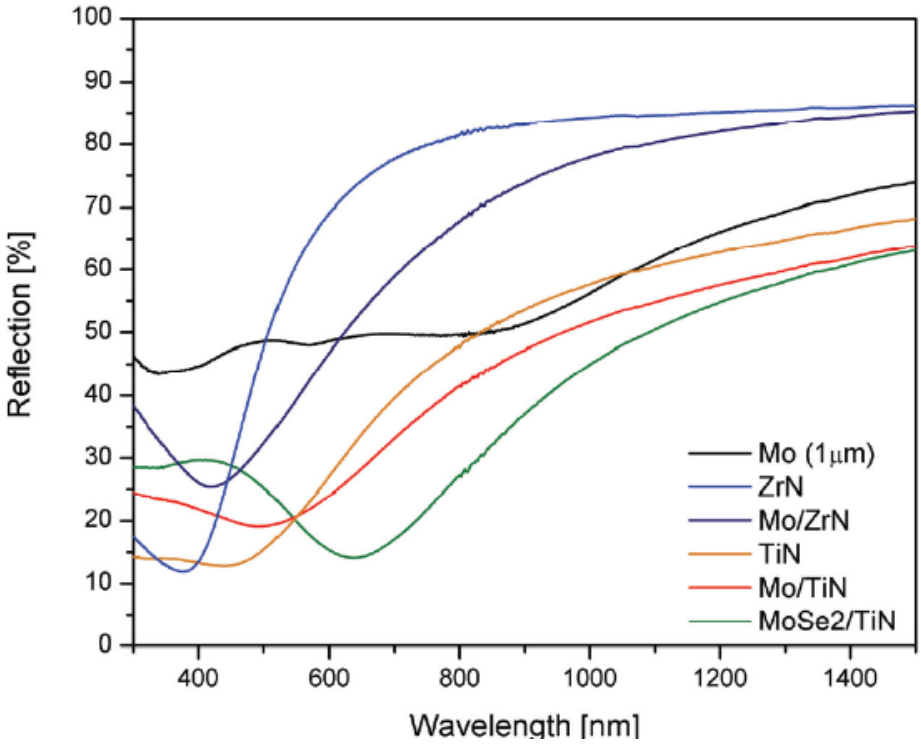

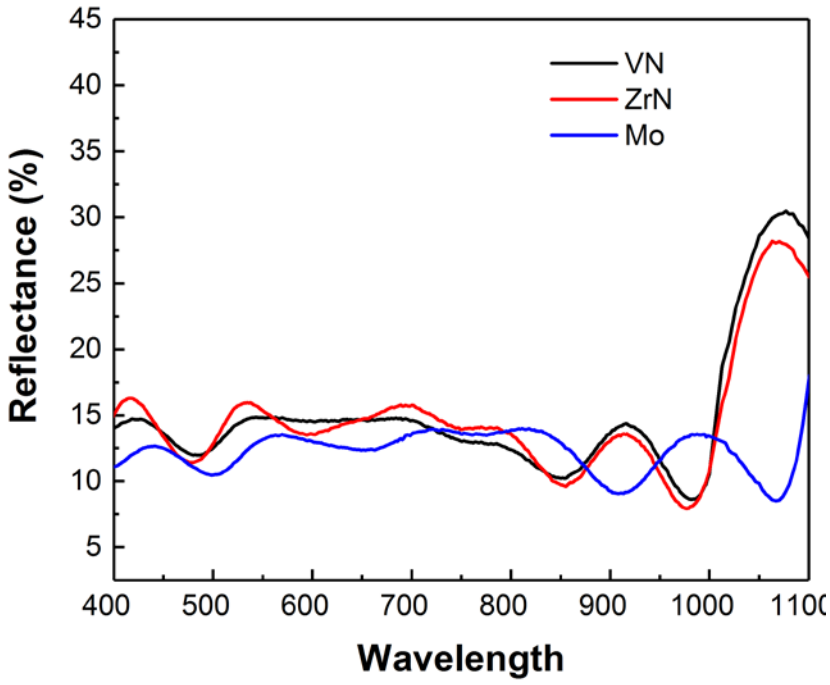

Figure 5. 20: a) Reflection (to air) for different back contacts [58], b) Reflectance curve for CIGS devices on alternative back contacts.

Due to the reduction of thickness of the CIGS layer, there is a decrease in the short circuit current thereby reducing the overall efficiency. As demonstrated, VN and ZrN have higher reflectivity towards the IR and near IR region, thus theoretically increasing the absorption in the region. This demonstrates therefore the capacity of this alternative scheme to produce better current as expected but also shows the limitations of our current process. Another problem arises from the Voc, which tends to be higher for the Mo contact due to better ohmicity.

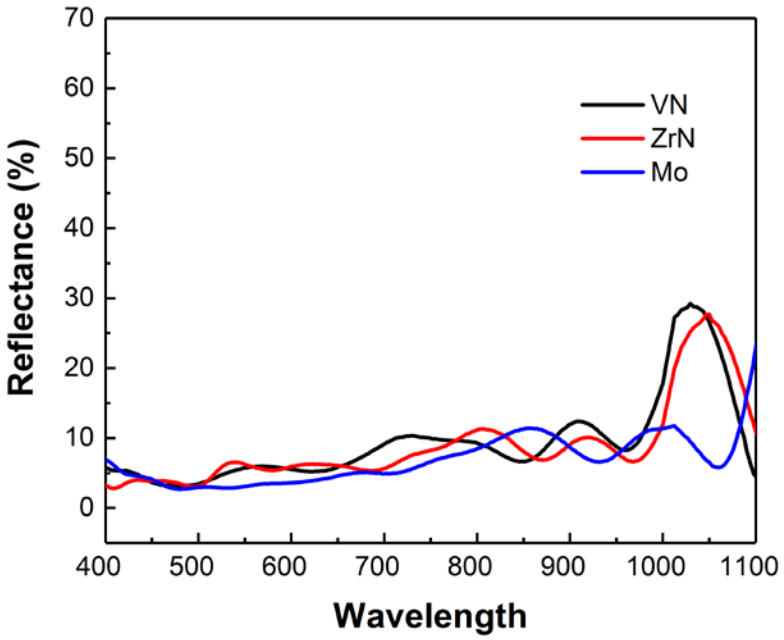

Figure 5. 21: Reflectance curve for CIGS solar cells with multi-layer AR coating on alternative back contacts.

Figure 5.22 compares the QE for CIGS device with the alternative back contact with CIGS device on Mo as back contact. One can see that, in the case of VN, the current indeed increases but that it decreases for ZrN.

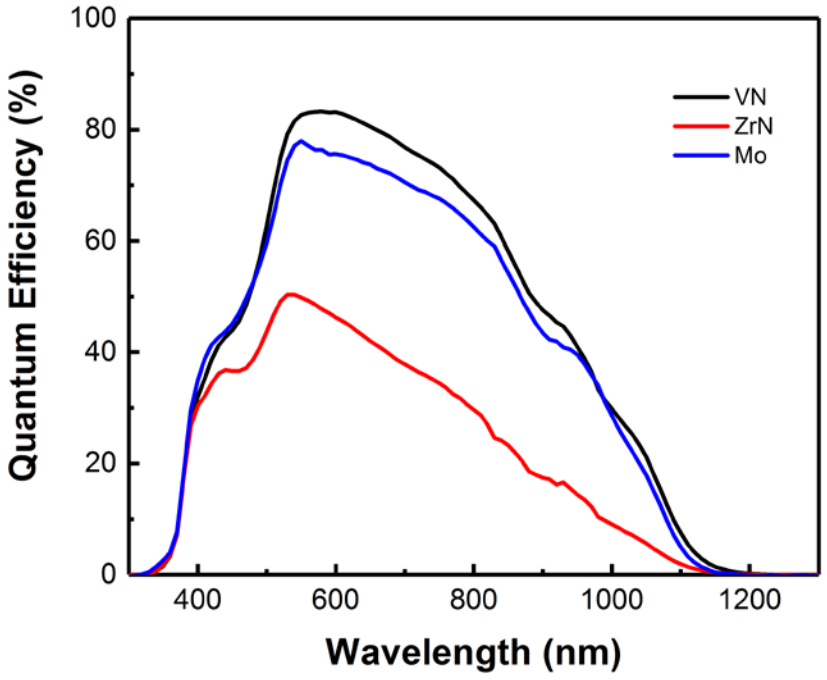

Figure 5. 22: Quantum efficiency measurements for CIGS devices with alternative back contacts.

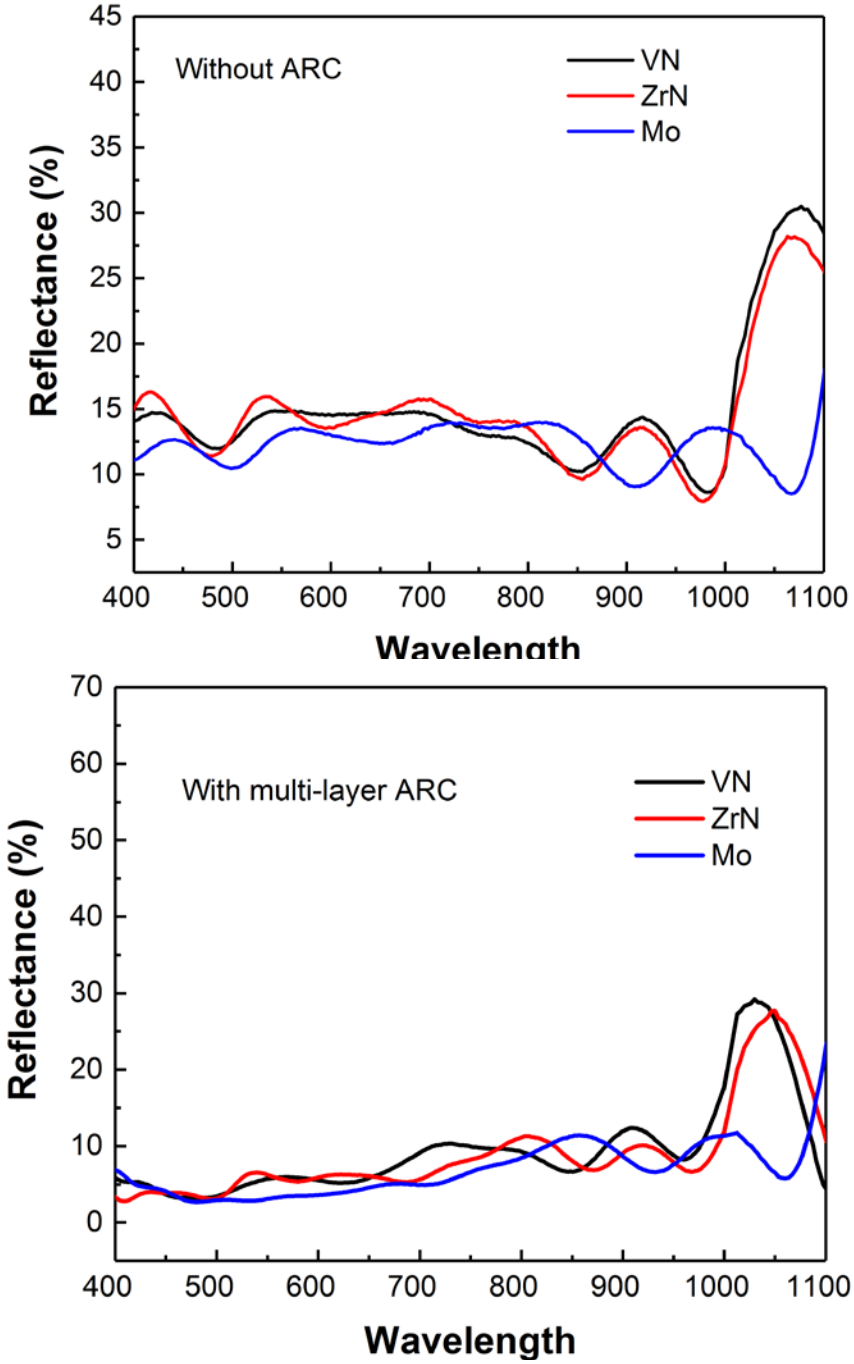

Figure 5. 23: Reflectance curve for CIGS devices with alternative back contacts with and without multi-layer ARC.

Due to the reduction of thickness of the CIGS layer, there is a decrease in the short circuit current thereby reducing the overall efficiency. VN and ZrN have higher reflectivity towards the IR and near IR region thus increasing the absorption in the region. Comparing the QE for CIGS device with the alternative back contact with CIGS device on Mo as back contact substantiates the increase in Jsc due to the increase in absorption. However, the QE for CIGS device with ZrN as back contact states that there is more room for optimization and improvement of the back contact layer. Figure 5.23 compares the reflectance curve for CIGS devices on alternative back contacts with and without the multi-layer AR coating. The average reflectance has been considerably reduced in a structure with multi-layer AR coatings.

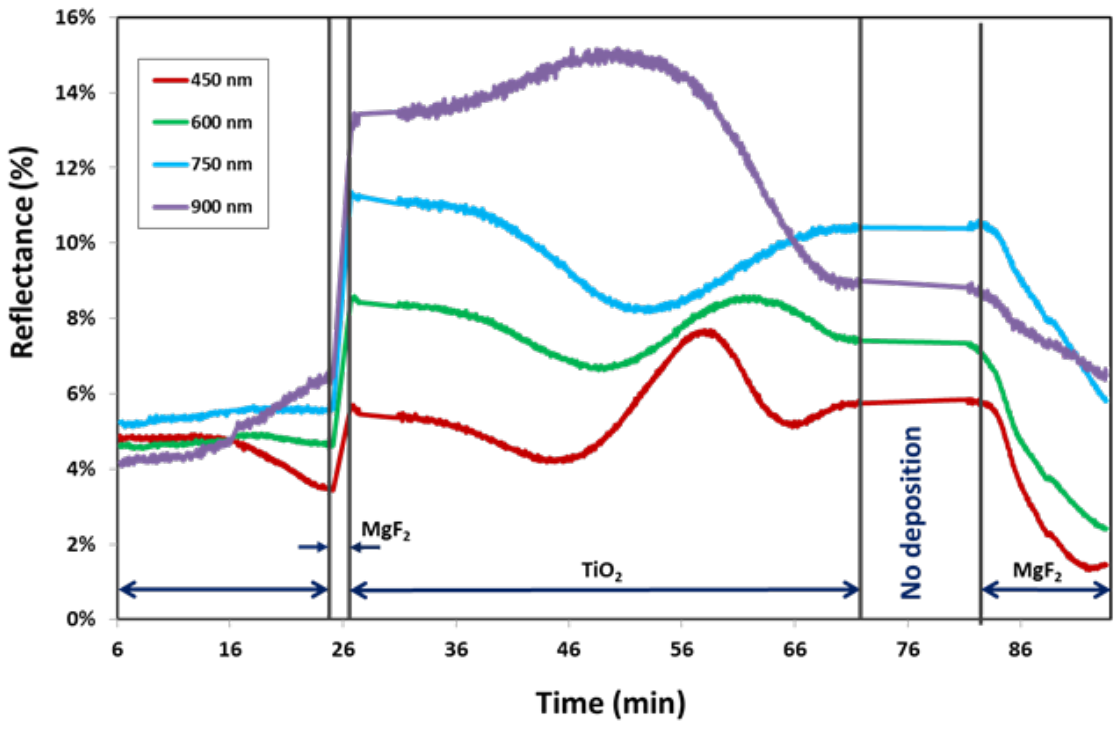

Figure 5. 24:Real time reflectance measurement during multi-layer AR coating on ultra-thin CIGS on Mo back contact

RTSE measurements were carried out to obtain relative reflectance of ultra-thin CIGS device on alternative back contacts with the multi-layer AR ($TiO_2/MgF_2/TiO_2/MgF_2$) coatings. The reflection intensity of the layers was closely monitored for different wavelength in-situ during the deposition of AR coating on CIGS device. Real time measurements aid to optimize the dimensions of the different AR layers so as to reduce the reflection for a specific spectral range thus leading a reduction in the average reflectance.

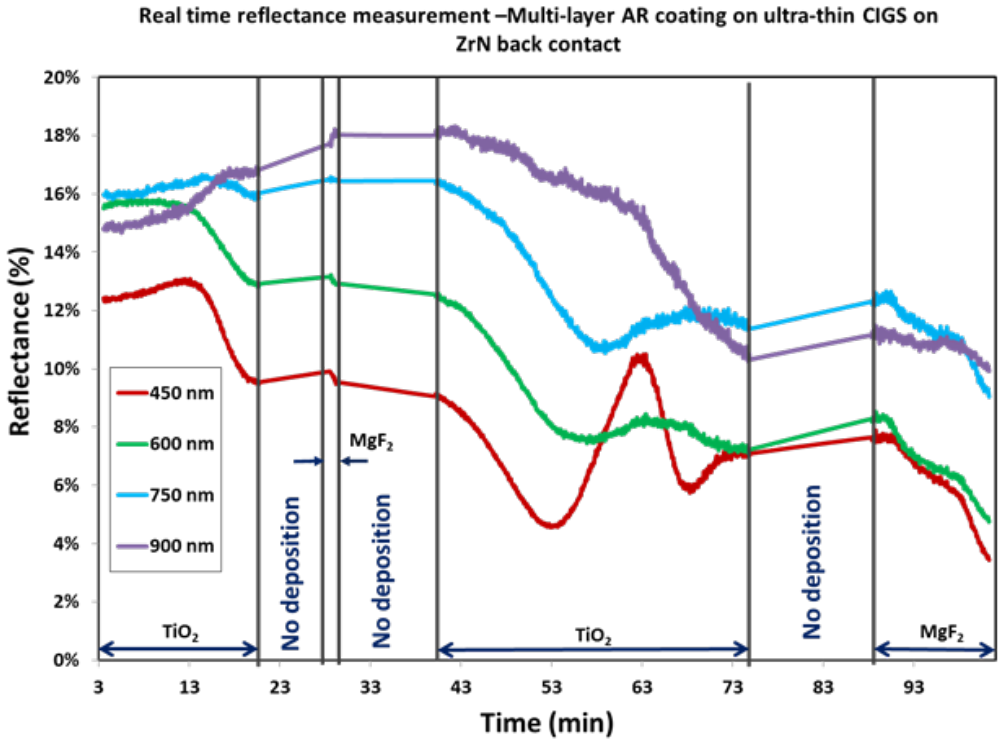

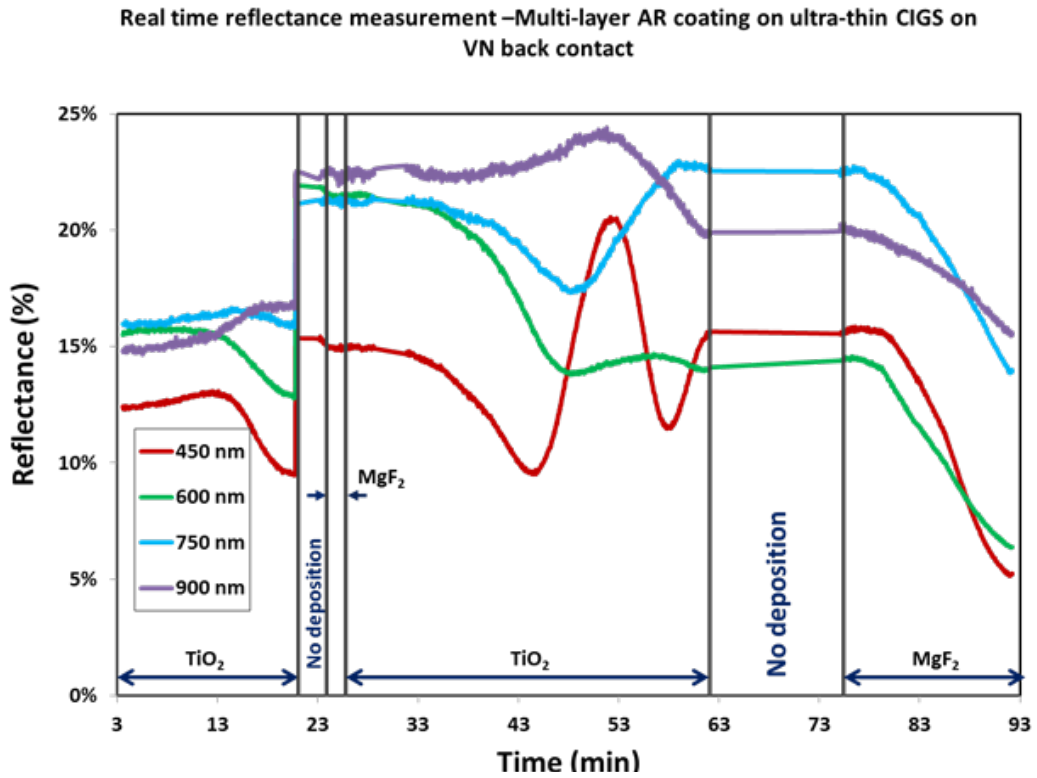

Figure 5. 25:Real time reflectance measurement during multi-layer AR coating on ultra-thin CIGS on VN and ZrN back contact

CONCLUSIONS

A solar cell is efficient when it is able to convert all the incoming photons to electron-hole pair with minimum reflectance from the layers. The optical trapping can be enhanced by having anti-reflective layers on the cell and the design on any AR coating is characterized by the irradiance, emittance, and absorptance of the media and also by the optical properties, index of refraction, and extinction coefficient of the materials. The AR coatings have to be chosen with great care as it has to be very durable, resistive to both physical and environmental damage and most importantly, it should be compatible with the substrate. Depending on the structure of the solar cell, either single layer or multilayer AR stack can be used to achieve enhanced light trapping. The critical influence of the thickness of the AR coating for CIGS applications was demonstrated via modeling and experimental results. Using a transfer matrix theory model, the influence of the thickness of CIGS, CdS and AZO was demonstrated. The importance of controlling the deposition parameters of the MgF_2 is discussed, as it influences the devices parameters. The experimental results confirmed the validity of the model and allowed for optimized devices to be fabricated. Real time spectroscopic ellipsometry was used to analyze the average reflectance of the CIGS structure to obtain optimum results. An optimized deposition of AR coating at room temperature provided an increase in the short circuit current density by around 5%, while the AR layer deposited at higher substrate temperature provided an increase of 10%.

The multi-layer anti-reflective coating structure using alternate high and low refractive index dielectric thin films are generally used for a variety of optical applications. GaAs and polycrystalline silicon devices have also explored the possibilities of the multi-layer AR structure. In this study, the potential of different materials to be used as AR coatings for ultra-thin CIGS applications has been explored and optimized. With multi-layer structure and coupled boundaries, the reflection effect can be considerably reduced across a wide wavelength range. Using a transfer matrix model and reflectance model, the structure and thickness of the AR layers were optimized. Optical modelling predicts a reduction of reflectance from 14% down to 6% with the optimized AR structure. The application of the multi-layer AR coating on the ultra-thin CIGS device increased the efficiency from 10.2% to 10.8% for the best device. The reduced reflectance leads to an improvement of the short circuit current density produced by the cell by 0.8 mA/cm^2 and this increase is definitely attractive as the thickness of the CIGS absorber layer gets further reduced. The performance of the multi-layer AR structure can be further improved by modifying the structure with a continuously graded refractive index that has more than one reflectivity minimum at several wavelengths. Also, the structure can be made more cost efficient by exploring the possibilities of a low cost and abundant material like zirconium dioxide and by optimizing the structure.

REFERENCES

[1] J. Poortmans and V. Arkhipov, *Thin film solar cells: fabrication, characterization and applications*. John Wiley & Sons, 2006.

[2] J. Goldemberg, "United Nations Development Programme, United Nations, Department of Economic and Social Affairs and World Energy Council (2000)," *World Energy Assessment: Energy and the Challenge of Sustainability*.

[3] X. Yan, L. Yang, X. Zhang, and W. Zhan, "Concept of an Accelerator-Driven Advanced Nuclear Energy System," *Energies*, vol. 10, no. 7, p. 944, 2017.

[4] C. Honsberg and S. Bowden, "Pvcdrom," *retrieved 16 th November 2011*, 2010.

[5] S. Anywhere, "SolarAnywhere data, Clean Power Research 2012," *URL< http://www. solaranywhere. com*, 2012.

[6] M. A. Green *et al.*, "Solar cell efficiency tables (version 50)," *Progress in Photovoltaics: Research and Applications*, vol. 25, no. 7, pp. 668-676, 2017.

[7] P. Jackson, R. Wuerz, D. Hariskos, E. Lotter, W. Witte, and M. Powalla, "Effects of heavy alkali elements in Cu (In, Ga) Se2 solar cells with efficiencies up to 22.6%," *physica status solidi (RRL)-Rapid Research Letters*, vol. 10, no. 8, pp. 583-586, 2016.

[8] S. M. Sze, *Semiconductor devices: physics and technology*. John Wiley & Sons, 2008.

[9] L. Aé *et al.*, "ZnO nanorod arrays as an antireflective coating for Cu (In, Ga) Se2 thin film solar cells," *Progress in Photovoltaics: Research and Applications*, vol. 18, no. 3, pp. 209-213, 2010.

[10] G. Rajan *et al.*, "Real-time optimization of anti-reflective coatings for CIGS solar cells," in *Photovoltaic Specialists Conference (PVSC), 2016 IEEE 43rd*, 2016, pp. 2250-2254: IEEE.

[11] G. Rajan *et al.*, "Optimization of anti-reflective coatings for CIGS solar cells via real time spectroscopic ellipsometry," in *Photovoltaic Specialist Conference (PVSC), 2015 IEEE 42nd*, 2015, pp. 1-4: IEEE.

[12] G. Rajan *et al.*, "Optimization of multi-layered anti-reflective coatings for ultra-thin Cu (In, Ga) Se 2 solar cells," in *Photovoltaic Specialists Conference (PVSC), 2016 IEEE 43rd*, 2016, pp. 1506-1510: IEEE.

[13] G. Rajan, A.-R. Ibdah, K. Aryal, R. W. Collins, and S. Marsillac, "Multi layered anti-reflective coatings for ultra-thin CIGS solar cells," in *Photovoltaic Specialists Conference (PVSC), 2013 IEEE 39th*, 2013, pp. 2026-2028: IEEE.

[14] A.-R. Ibdah *et al.*, "Solar cells with thin Cu (In1-xGax) Se 2 absorbers: Optical analysis and quantum efficiency simulations," in *Photovoltaic Specialist Conference (PVSC), 2014 IEEE 40th*, 2014, pp. 0373-0378: IEEE.

[15] G. Rajan, K. Aryal, S. Karki, P. Aryal, R. W. Collins, and S. Marsillac, "Characterization and Analysis of Ultrathin CIGS Films and Solar Cells Deposited by 3-Stage Process," *Journal of Spectroscopy*, vol. 2018, 2018.

[16] G. Rajan *et al.*, "Real-time optimization of anti-reflective coatings for CIGS solar cells," in *2017 IEEE 44th Photovoltaic Specialist Conference (PVSC)*, 2017, pp. 1-5.

[17] I. A. Digdaya, "Optical enhancement for heterojunction silicon solar cells," 2012.

[18] J. Woollam, "Guide to Using WVASE32 Spectroscopic Ellipsomtry Data Acquisition and Analysis Software. JA Woollam Co," ed: Inc, 2005.

[19] H. Tompkins, "A User's Guide to Ellipsometry Academic," *New York*, pp. 26-30, 1993.

[20] D. K. Schroder, *Semiconductor material and device characterization*. John Wiley & Sons, 2006.

[21] D. Gonçalves and E. A. Irene, "Fundamentals and applications of spectroscopic ellipsometry," *Química Nova*, vol. 25, no. 5, pp. 794-800, 2002.

[22] H. Fujiwara, *Spectroscopic ellipsometry: principles and applications*. John Wiley & Sons, 2007.

[23] L. A. Pettersson, L. S. Roman, and O. Inganäs, "Modeling photocurrent action spectra of photovoltaic devices based on organic thin films," *Journal of Applied Physics*, vol. 86, no. 1, pp. 487-496, 1999.

[24] M. Stockett, "Optical properties of thin transparent conducting oxide films on glass for photovoltaic applications," ed: Thesis, Oberlin College, 2006.

[25] A. Poruba *et al.*, "Optical absorption and light scattering in microcrystalline silicon thin films and solar cells," *Journal of Applied Physics*, vol. 88, no. 1, pp. 148-160, 2000.

[26] J. Springer, A. Poruba, and M. Vanecek, "Improved three-dimensional optical model for thin-film silicon solar cells," *Journal of Applied Physics*, vol. 96, no. 9, pp. 5329-5337, 2004.

[27] J. Prentice, "Coherent, partially coherent and incoherent light absorption in thin-film multilayer structures," *Journal of Physics D: Applied Physics,* vol. 33, no. 24, p. 3139, 2000.

[28] J. Prentice, "Optical generation rate of electron-hole pairs in multilayer thin-film photovoltaic cells," *Journal of Physics D: Applied Physics,* vol. 32, no. 17, p. 2146, 1999.

[29] C. Suryanarayana and M. G. Norton, *X-ray diffraction: a practical approach*. Springer Science & Business Media, 2013.

[30] T. M. Friedlmeier *et al.*, "Improved photocurrent in Cu (In, Ga) Se 2 solar cells: from 20.8% to 21.7% efficiency with CdS buffer and 21.0% Cd-free," *IEEE Journal of Photovoltaics,* vol. 5, no. 5, pp. 1487-1491, 2015.

[31] P. Kaminski, F. Lisco, and J. Walls, "Multilayer broadband antireflective coatings for more efficient thin film CdTe solar cells," *IEEE Journal of Photovoltaics,* vol. 4, no. 1, pp. 452-456, 2014.

[32] P. Nubile, "Analytical design of antireflection coatings for silicon photovoltaic devices," *Thin solid films,* vol. 342, no. 1, pp. 257-261, 1999.

[33] A. Chirila *et al.*, "Highly efficient Cu (In, Ga) Se2 solar cells grown on flexible polymer films," *Nature materials,* vol. 10, no. 11, p. 857, 2011.

[34] M. A. Contreras *et al.*, "Progress toward 20% efficiency in Cu (In, Ga) Se2 polycrystalline thin-film solar cells," *Progress in Photovoltaics: Research and applications,* vol. 7, no. 4, pp. 311-316, 1999.

[35] P. Jackson *et al.*, "Properties of Cu (In, Ga) Se2 solar cells with new record efficiencies up to 21.7%," *physica status solidi (RRL)-Rapid Research Letters*, vol. 9, no. 1, pp. 28-31, 2015.

[36] J. Walker, H. Khatri, V. Ranjan, J. Li, R. Collins, and S. Marsillac, "Electronic and structural properties of molybdenum thin films as determined by real-time spectroscopic ellipsometry," *Applied Physics Letters*, vol. 94, no. 14, p. 141908, 2009.

[37] P. Aryal, *Optical and photovoltaic properties of copper indium-gallium diselenide materials and solar cells*. The University of Toledo, 2014.

[38] G. Rajan *et al.*, "Optical enhancement of ultra-thin CIGS solar cells using multi-layered antireflection coatings," in *Photovoltaic Specialist Conference (PVSC), 2014 IEEE 40th*, 2014, pp. 1687-1690: IEEE.

[39] W. N. Shafarman and L. Stolt, "Cu (InGa) Se2 Solar Cells," *Handbook of photovoltaic science and engineering*, vol. 2, pp. 546-599, 2003.

[40] W. Shafarman, R. Birkmire, S. Marsillac, M. Marudachalam, N. Orbey, and T. Russell, "Effect of Reduced Deposition Temperature, Time, and Thickness on Cu (InGa) Se~ 2 Films and Devices," in *CONFERENCE RECORD IEEE PHOTOVOLTAIC SPECIALISTS CONFERENCE*, 1997, vol. 26, pp. 331-334: IEEE INC.

[41] K. Orgassa, U. Rau, Q. Nguyen, H. Werner Schock, and J. H. Werner, "Role of the CdS buffer layer as an active optical element in Cu (In, Ga) Se2 thin-film solar cells," *Progress in Photovoltaics: Research and Applications*, vol. 10, no. 7, pp. 457-463, 2002.

[42] M. Islam *et al.*, "Thickness study of Al: ZnO film for application as a window layer in Cu (In 1− x Ga x) Se 2 thin film solar cell," *Applied Surface Science,* vol. 257, no. 9, pp. 4026-4030, 2011.

[43] H.-H. Yang and G.-C. Park, "A Study on the properties of MgF 2 Antireflection film for Solar Cells," *Transactions on electrical and electronic materials,* vol. 11, no. 1, pp. 33-36, 2010.

[44] T. Pilvi *et al.,* "Study of a novel ALD process for depositing MgF 2 thin films," *Journal of Materials Chemistry,* vol. 17, no. 48, pp. 5077-5083, 2007.

[45] C.-L. Tien and T.-W. Lin, "Temperature-dependent optical and mechanical properties of obliquely deposited MgF2 thin films," *Indian Journal of Pure & Applied Physics (IJPAP),* vol. 52, no. 2, pp. 117-123, 2015.

[46] C. van Lare, G. Yin, A. Polman, and M. Schmid, "Light coupling and trapping in ultrathin Cu (In, Ga) Se2 solar cells using dielectric scattering patterns," *ACS nano,* vol. 9, no. 10, pp. 9603-9613, 2015.

[47] A. Macleod, "Optical Thin Films," *Handbook of Thin Film Deposition (third ed.), William Andrew Publishing, Oxford,* pp. 271-311, 2012.

[48] A. Elshabini, A. A. Elshabini-Riad, and F. D. Barlow, *Thin film technology handbook*. McGraw-Hill Professional, 1998.

[49] A. Macleod and C. Clark, "Optical coating design with the Essential Macleod," 2012.

[50] W. Qiu *et al.,* "An ultrabroad band omni-directional anti-reflective coating with quasi-gradient refractive index distribution based on Si–SiOxNy–SiO2 materials system," *Japanese Journal of Applied Physics,* vol. 53, no. 2, p. 021501, 2014.

[51] M. F. Schubert, F. W. Mont, S. Chhajed, D. J. Poxson, J. K. Kim, and E. F. Schubert, "Design of multilayer antireflection coatings made from co-sputtered and low-refractive-index materials by genetic algorithm," *Optics express*, vol. 16, no. 8, pp. 5290-5298, 2008.

[52] D. J. Aiken, "High performance anti-reflection coatings for broadband multi-junction solar cells," *Solar energy materials and solar cells*, vol. 64, no. 4, pp. 393-404, 2000.

[53] L. Hsu, J. Luo, K. Yeh, T. Chen, T. Huang, and P. Wu, "& Lee, A," *Director*, 1994.

[54] U. B. Schallenberg, "Antireflection design concepts with equivalent layers," *Applied optics*, vol. 45, no. 7, pp. 1507-1514, 2006.

[55] G. Womack, P. M. Kaminski, and J. Walls, "High temperature stability of broadband Anti-Reflection coatings on soda lime glass for solar modules," in *Photovoltaic Specialist Conference (PVSC), 2015 IEEE 42nd*, 2015, pp. 1-6: IEEE.

[56] S. M. Schleussner, "ZrN Back-Contact Reflectors and Ga Gradients in Cu (In, Ga) Se2 Solar Cells," Acta Universitatis Upsaliensis, 2011.

[57] K. Orgassa, H. W. Schock, and J. Werner, "Alternative back contact materials for thin film Cu (In, Ga) Se2 solar cells," *Thin Solid Films*, vol. 431, pp. 387-391, 2003.

[58] D. J. L. Brémaud, "Investigation and development of CIGS solar cells on flexible substrates and with alternative electrical back contacts," ETH, 2009.

APPENDICES

Title: Optical enhancement of ultra-thin CIGS solar cells using multi-layered antireflection coatings

Conference Proceedings: 2014 IEEE 40th Photovoltaic Specialist Conference (PVSC)

Author: Grace Rajan; Abdel-Rahman Ibdah; Krishna Aryal; Tasnuva Ashrafee; Vikash Ranjan; Elizabeth A Pogue; Angus Rockett; Robert W. Collins; Sylvain Marsillac

Publisher: IEEE

Date: 8-13 June 2014

Thesis / Dissertation Reuse

The IEEE does not require individuals working on a thesis to obtain a formal reuse license, however, you may print out this statement to be used as a permission grant:

Requirements to be followed when using any portion (e.g., figure, graph, table, or textual material) of an IEEE copyrighted paper in a thesis:

1) In the case of textual material (e.g., using short quotes or referring to the work within these papers) users must give full credit to the original source (author, paper, publication) followed by the IEEE copyright line © 2011 IEEE.
2) In the case of illustrations or tabular material, we require that the copyright line © [Year of original publication] IEEE appear prominently with each reprinted figure and/or table.
3) If a substantial portion of the original paper is to be used, and if you are not the senior author, also obtain the senior author's approval.

Requirements to be followed when using an entire IEEE copyrighted paper in a thesis:

1) The following IEEE copyright/ credit notice should be placed prominently in the references: © [year of original publication] IEEE. Reprinted, with permission, from [author names, paper title, IEEE publication title, and month/year of publication]
2) Only the accepted version of an IEEE copyrighted paper can be used when posting the paper or your thesis on-line.
3) In placing the thesis on the author's university website, please display the following message in a prominent place on the website: In reference to IEEE copyrighted material which is used with permission in this thesis, the IEEE does not endorse any of [university/educational entity's name goes here]'s products or services. Internal or personal use of this material is permitted. If interested in reprinting/republishing IEEE copyrighted material for advertising or promotional purposes or for creating new collective works for resale or redistribution, please go to http://www.ieee.org/publications_standards/publications/rights/rights_link.html to learn how to obtain a License from RightsLink.

If applicable, University Microfilms and/or ProQuest Library, or the Archives of Canada may supply single copies of the dissertation.

Title: Optimization of anti-reflective coatings for CIGS solar cells via real time spectroscopic ellipsometry
Conference Proceedings: 2015 IEEE 42nd Photovoltaic Specialist Conference (PVSC)
Author: Grace Rajan
Publisher: IEEE
Date: June 2015

Thesis / Dissertation Reuse

The IEEE does not require individuals working on a thesis to obtain a formal reuse license, however, you may print out this statement to be used as a permission grant:

Requirements to be followed when using any portion (e.g., figure, graph, table, or textual material) of an IEEE copyrighted paper in a thesis:

1) In the case of textual material (e.g., using short quotes or referring to the work within these papers) users must give full credit to the original source (author, paper, publication) followed by the IEEE copyright line © 2011 IEEE.
2) In the case of illustrations or tabular material, we require that the copyright line © [Year of original publication] IEEE appear prominently with each reprinted figure and/or table.
3) If a substantial portion of the original paper is to be used, and if you are not the senior author, also obtain the senior author's approval.

Requirements to be followed when using an entire IEEE copyrighted paper in a thesis:

1) The following IEEE copyright/ credit notice should be placed prominently in the references: © [year of original publication] IEEE. Reprinted, with permission, from [author names, paper title, IEEE publication title, and month/year of publication]
2) Only the accepted version of an IEEE copyrighted paper can be used when posting the paper or your thesis on-line.
3) In placing the thesis on the author's university website, please display the following message in a prominent place on the website: In reference to IEEE copyrighted material which is used with permission in this thesis, the IEEE does not endorse any of [university/educational entity's name goes here]'s products or services. Internal or personal use of this material is permitted. If interested in reprinting/republishing IEEE copyrighted material for advertising or promotional purposes or for creating new collective works for resale or redistribution, please go to http://www.ieee.org/publications_standards/publications/rights/rights_link.html to learn how to obtain a License from RightsLink.

If applicable, University Microfilms and/or ProQuest Library, or the Archives of Canada may supply single copies of the dissertation.

BACK CLOSE WINDOW

Title: Optimization of multi-layered anti-reflective coatings for ultra-thin Cu (In, Ga)Se2 solar cells
Conference Proceedings: 2016 IEEE 43rd Photovoltaic Specialists Conference (PVSC)
Author: G. Rajan
Publisher: IEEE
Date: June 2016

Thesis / Dissertation Reuse

The IEEE does not require individuals working on a thesis to obtain a formal reuse license, however, you may print out this statement to be used as a permission grant:

Requirements to be followed when using any portion (e.g., figure, graph, table, or textual material) of an IEEE copyrighted paper in a thesis:

1) In the case of textual material (e.g., using short quotes or referring to the work within these papers) users must give full credit to the original source (author, paper, publication) followed by the IEEE copyright line © 2011 IEEE.
2) In the case of illustrations or tabular material, we require that the copyright line © [Year of original publication] IEEE appear prominently with each reprinted figure and/or table.
3) If a substantial portion of the original paper is to be used, and if you are not the senior author, also obtain the senior author's approval.

Requirements to be followed when using an entire IEEE copyrighted paper in a thesis:

1) The following IEEE copyright/ credit notice should be placed prominently in the references: © [year of original publication] IEEE. Reprinted, with permission, from [author names, paper title, IEEE publication title, and month/year of publication]
2) Only the accepted version of an IEEE copyrighted paper can be used when posting the paper or your thesis on-line.
3) In placing the thesis on the author's university website, please display the following message in a prominent place on the website: In reference to IEEE copyrighted material which is used with permission in this thesis, the IEEE does not endorse any of [university/educational entity's name goes here]'s products or services. Internal or personal use of this material is permitted. If interested in reprinting/republishing IEEE copyrighted material for advertising or promotional purposes or for creating new collective works for resale or redistribution, please go to http://www.ieee.org/publications_standards/publications/rights/rights_link.html to learn how to obtain a License from RightsLink.

If applicable, University Microfilms and/or ProQuest Library, or the Archives of Canada may supply single copies of the dissertation.

Title: Real-time optimization of anti-reflective coatings for CIGS solar cells
Conference Proceedings: 2017 IEEE 44th Photovoltaic Specialist Conference (PVSC)
Author: Grace Rajan
Publisher: IEEE
Date: June 2017

Thesis / Dissertation Reuse

The IEEE does not require individuals working on a thesis to obtain a formal reuse license, however, you may print out this statement to be used as a permission grant:

Requirements to be followed when using any portion (e.g., figure, graph, table, or textual material) of an IEEE copyrighted paper in a thesis:

1) In the case of textual material (e.g., using short quotes or referring to the work within these papers) users must give full credit to the original source (author, paper, publication) followed by the IEEE copyright line © 2011 IEEE.
2) In the case of illustrations or tabular material, we require that the copyright line © [Year of original publication] IEEE appear prominently with each reprinted figure and/or table.
3) If a substantial portion of the original paper is to be used, and if you are not the senior author, also obtain the senior author's approval.

Requirements to be followed when using an entire IEEE copyrighted paper in a thesis:

1) The following IEEE copyright/ credit notice should be placed prominently in the references: © [year of original publication] IEEE. Reprinted, with permission, from [author names, paper title, IEEE publication title, and month/year of publication]
2) Only the accepted version of an IEEE copyrighted paper can be used when posting the paper or your thesis on-line.
3) In placing the thesis on the author's university website, please display the following message in a prominent place on the website: In reference to IEEE copyrighted material which is used with permission in this thesis, the IEEE does not endorse any of [university/educational entity's name goes here]'s products or services. Internal or personal use of this material is permitted. If interested in reprinting/republishing IEEE copyrighted material for advertising or promotional purposes or for creating new collective works for resale or redistribution, please go to http://www.ieee.org/publications_standards/publications/rights/rights_link.html to learn how to obtain a License from RightsLink.

If applicable, University Microfilms and/or ProQuest Library, or the Archives of Canada may supply single copies of the dissertation.

BACK CLOSE WINDOW

VITA

Grace Cherukara Rajan

231 Kaufman Hall
ECE Department
Old Dominion University
Norfolk, VA 23529

Education

2018	**Ph.D.**	Electrical Engineering	Old Dominion University, VA
2009	**B.Tech.**	Electrical & Electronics Engineering	Kerala University, India.

Selected Peer Reviewed Publications

1. **Rajan G**, Aryal K, Karki S, Collins R.W, Marsillac S., "Characterization and analysis of Ultra-thin CIGS films and solar cells deposited by 3-stage process", *Journal of Spectroscopy*, vol. 2018, Article ID 8527491, 9 pages, 2018.
2. Karki S, Paul PK, **Rajan G**, Ashrafee T, Aryal K, Pradhan P, Marsillac S., "In Situ and Ex Situ Investigations of KF Postdeposition Treatment Effects on CIGS Solar Cells", *IEEE Journal of Photovoltaics*. 2017; 7: 665-9.

Selected Conference Proceedings

1. **Rajan G**, Karki S, Collins R.W, Marsillac S., "Enhanced Anti-Reflective Coating for Thin Film Solar Cells", *Photovoltaic Specialists Conference (PVSC)*, 2017 IEEE 44th: IEEE; 2017.
2. **Rajan G**, Miryala T, Karki S, Collins R.W, Podraza N.J, Marsillac S., "Influence of Deposition Parameters on Silicon Thin Films Deposited by Magnetron Sputtering", *Photovoltaic Specialists Conference (PVSC)*, 2017 IEEE 44th: IEEE; 2017.
3. **Rajan G**, Karki S, Butt I, Aryal K, Grassman T.J., Rockett A., Marsillac S., "Understanding Instabilities and Degradation due to Moisture Ingress in Cu(In,Ga)Se_2 Solar Cells", *Photovoltaic Specialists Conference (PVSC)*, 2017 IEEE 44th: IEEE; 2017.
4. **Rajan G**, Begou T, Aryal K, Ashrafee T, Karki S, Ranjan V, et al., "Optimization of multi-layered anti-reflective coatings for ultra-thin Cu (In, Ga) Se 2 solar cells", *Photovoltaic Specialists Conference (PVSC)*, 2016 IEEE 43rd: IEEE; 2016. p. 1506-10.
5. **Rajan G,** Aryal K, Ashrafee T, Karki S, Babcock S, Ranjan V, et al. Real-time optimization of anti-reflective coatings for CIGS solar cells. Photovoltaic Specialists Conference (PVSC), 2016 IEEE 43rd: IEEE; 2016. p. 2250-4.

Honors, Awards and Scholarships

1. **Graduate Student Travel Award (2017),** by the Division of Student Engagement and Enrollment at Old Dominion University to attend IEEE 44th PVSC Conference, Washington D.C, 2017.
2. **Best poster award, Runner up at IEEE 43th PVSC Conference, Portland (2016)** "Optimization of Multi-layered Anti-reflective coatings for Ultra-Thin Cu(In,Ga)Se_2 Solar Cells".
3. **Graduate Student Assistantship Award (2015 & 2016),** at the IEEE 43rd PVSC Conference, Portland 2016 and IEEE 42nd PVSC Conference, New Orleans 2015.
4. **Outstanding Teaching Assistant Award (2015),** Department of Electrical & Computer Engineering, Old Dominion University.
5. **Outstanding Graduate Student Service Award (2014),** Department of Electrical & Computer Engineering, Old Dominion University.